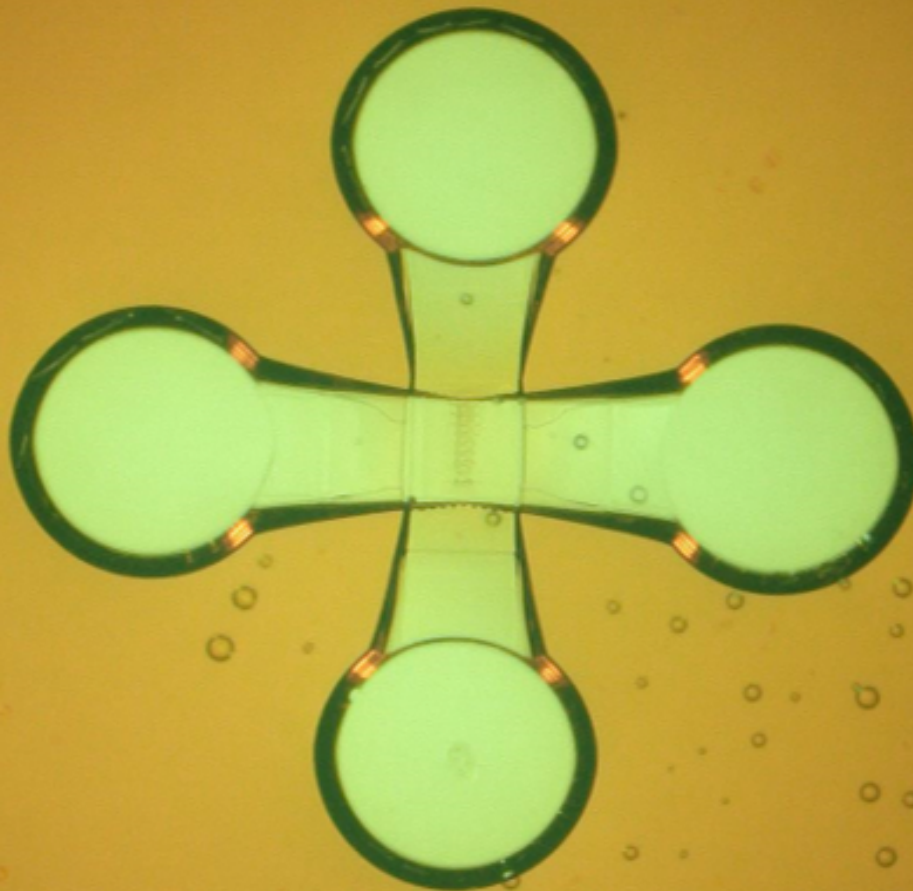


Department of Precision and Microsystems Engineering

Fabrication of a microfluidic device by using two-photon lithography on a positive photoresist

G. van der Velden

Report no : 2019.016
Coach : Prof. Dr. U. Staufer, Dr. D. Fan
Professor : Prof. Dr. U. Staufer
Specialisation : Micro and Nano Engineering
Type of report : MSc Thesis
Date : 25 June 2019



Fabrication of a microfluidic device by using two-photon lithography on a positive photoresist

MASTER OF SCIENCE THESIS

For the degree of Master of Science in Precision and Microsystems Engineering at Delft University of Technology

G. van der Velden

June 25, 2019

Student number: 4220595

Thesis committee: Prof. Dr. U. Staufer, TU Delft
Dr. D. Fan, TU Delft
Dr. Ir. J.F.L. Goosen, TU Delft

An electronic version of this thesis is available at <http://repository.tudelft.nl/>.



Preface

Dear reader, welcome to the first page of my thesis. I would like to thank you for opening this document and for taking the time to read my entire thesis called "Fabrication of a microfluidic device by using two-photon lithography on a positive photoresist". I spent one year doing experiments and making models to research this topic and to make a valuable contribution to the academic world.

There are some people I would like to thank for their contribution to the project. Luigi Sasso for helping me find this research topic and getting me started on the project, Daniel Fan and Urs Stauer for the supervision during the project, and the lab technicians of our department for helping me in the lab. Furthermore I would like to thank my friends, my family and Lola for giving me motivation and support throughout my research.

Delft, University of Technology
June 11, 2019

G. van der Velden

Abstract

Organ-on-chip (OoC) devices are increasingly used for biomedical research and to speed up the process of bringing a medicinal drug from the lab to the market. The technology also addresses ethical issues linked to animal testing as it offers a reduction in animal experiments through its possibility to mimic the environment in the human body. Hence, it produces more relevant results than plain cell-culture experiments, while still sharing the possibility of high-throughput testing by simultaneously operating many devices in parallel. The main components of an OoC device are microfluidic channels and porous membranes. Current chips are often assembled from several parts. In the development phase a small change in design will cause a delay in the research because a new prototype has to be built again step-by-step. This research addresses this problem by targeting the fabrication of a microfluidic device in a single lithography and development step. A device consisting of two crossed channels at different heights separated by a membrane was chosen.

The manufacturing method used was two-photon lithography (TPL) on positive photoresist AZ 4562. TPL exploits the fact that two-photon absorption non-linearly depends on the light intensity. The required intensity is only achieved in a small volume around the focal point, called the voxel. By positioning and moving this voxel inside the resist, 3D manufacturing is possible. Therefore the technique can be used for the single step fabrication of a closed channel. By vertically moving the voxel through the resist, pores can be manufactured. In literature an ellipsoidal voxel shape is assumed, leading to the assumption that the maximum voxel, and therefore pore diameter is found at the focal plane, i.e. at $z = 0$. However, this research shows that the voxel may also have an hourglass-shape for a high enough laser intensity. In this case the maximum voxel diameter is found at a distance z from the focal plane. For the production of pores, therefore the maximum voxel diameter instead of the diameter at the focal plane has to be taken into account.

The smallest pores produced measured 250 nm - 290 nm. AZ 4562 was used as a stamp and a mold for the manufacturing of 3D topographical features on a PDMS surface. Finally the microfluidic device was successfully produced in a layer of 50 μm thick resist. The channel width was 100 μm and the height was 10 μm . The channels were separated by 10 μm in height. The sizes of the input and output holes were adapted to the diameter of the smallest available blunt needle, which is 210 μm .

Table of Contents

1	Introduction	1
1-1	Motivation	1
1-2	Manufacturing methods	3
1-3	Prior Art of TPL on a positive photoresist	6
1-4	Planning	7
1-5	Report outline	7
2	Paper written for Elsevier journal: Micro and Nano Engineering	9
3	Methods and materials	15
3-1	Photon Energy	15
3-2	Introduction to Photolithography	15
3-3	Positive photoresists	18
3-4	AZ 4562	19
3-5	The setup	23
4	Characterization	25
4-1	The main equation	25
4-2	Experimental results	28
4-3	Conclusions and discussion	33
5	3D manufacturing	37
5-1	Straight pillars	37
5-2	3D structures	39
5-3	AZ 4562 as a mold	39
5-4	Conclusions and discussion	41

6	Fabrication of the microfluidic device	43
6-1	Channel and chip manufacturing	43
6-2	Conclusions and discussion	45
7	Conclusions and recommendations	47
8	Reflection	49
A	Additional mathematical information	51
A-1	Equation derivation and explanation	51
A-2	Characterization steps and decisions	54
B	Experimental results	57
B-1	Data and model fits for different scanning speeds	57
B-2	Data from scanning voxel	60
B-3	3D structures	62
B-4	Channel and chip manufacturing	64
C	Writing protocols	65
C-1	General protocol	65
C-2	Interface finding	66
C-3	Piezo mode writing	67
C-4	Galvo mode writing	68
C-5	Stamp/Mold for PDMS	68
C-6	Channel manufacturing	68
D	Project steps, designs and decisions	71
D-1	Finding the interface	71
D-2	Project steps for Galvo Scan Mode	72
D-3	Project steps for Piezo Scan mode	76
D-4	3D structures	80
D-5	Channel and chip manufacturing	81
E	Extra work	85
E-1	Automatic pore diameter measurement	85
E-2	GUI for model fitting	88
E-3	Preparing for electrochemical deposition	89
E-4	Needle preparation	89

List of Figures

1-1	A standard microfluidic chip.	2
1-2	Gantt chart of the initial project planning.	8
3-1	The energy of light is related to the wavelength. <i>Image from Hudedmani, et al.</i>	16
3-2	The difference between a negative and a positive photoresist, illustrated with help of a mask.	16
3-3	(a) Electron jump by single-photon absorption. (b) Electron jump via virtual state by two-photon absorption.	17
3-4	Exposed volume of UV and NIR light, <i>By Nanoscribe.</i>	18
3-5	Contrast curves, <i>By Campbell: The Science and Engineering of Microelectronic Fabrication.</i>	19
3-6	The most relevant way to describe TPL with a positive photoresist is with a graph showing the voxel size for different laser powers. <i>Image by Cao et al.</i>	19
3-7	(a) Novolac is the backbone of the AZ resist. (b) DNQ is the photosensitive molecule in the resist.	20
3-8	The three steps of the chemical reaction that occurs when DNQ is exposed to a laser with sufficient energy to initiate TPA.	21
3-9	The Photonic Professional GT, <i>By Nanoscribe.</i>	23
3-10	The profile of a Gaussian beam with the intensity distribution at different distances from the focal plane.	24
4-1	Pores with a diameter between 250 - 290 nm.	28
4-2	(a) The least squares error fit for the given dataset. (b) The 3D model of the voxel at a laser power of 3.5 mW.	29
4-3	The voxel is lowered into the resist with steps of 50 nm.	29
4-4	(a) Combined least squares error fit for the voxel height (red) and diameter (blue). The total height of the voxel (i.e. 2z) is shown. (b) 3D visualization of the voxel at laser power 3.5 mW and scanning speed 40 $\mu\text{m}/\text{s}$	30
4-5	(a) The obtained values for K_{CtM} decrease linearly with an increasing scanning speed. (b) The possible combinations of Ct and M_{th} for the obtained value of K_{CtM}	31

4-6	(a) Voxel diameter and height test by lowering the voxel with steps of 50 nm, from right to left, starting in the lower right corner and then upwards. The scanning speed was 40 $\mu\text{m}/\text{s}$ and the laser power was 3.5 mW. (b) The measured voxel diameter at different heights in red and the cross-section of the calculated voxel shape in blue.	31
4-7	The predicted voxel shape for different laser powers (mW).	32
4-8	Voxel with arrows indicating diffusion of functionalized DNQ at three different locations. The effect will be larger at the waist of the voxel.	34
5-1	The NIL process to create straight pillars.	38
5-2	The NIL process for 3D structures.	39
5-3	The process for producing 3D structures by using a mold.	40
6-1	(a) Fully developed channel with a width of 100 μm , a height of 10 μm and a length of respectively 180, 380 and 580 μm . (b) SEM image under 45° angle showing that the channels are closed. (c) Optical image of a small channel that was produced. The height and width are 10 μm and the length is 420 μm	44
6-2	(a) An optical image of the fully developed chip. (b) The white light interferometer shows that the channels are under the surface.	45
6-3	(a) Micrograph of the in- or outlet hole to the lower channel taken in the SEM under a 45° angle. (b) Micrograph of the in- or outlet hole to the higher channel. . . .	45
6-4	(a) Dry channels before they were filled with water. (b) Channels filled with water. . . .	46
A-1	Mathematical influence of the material threshold value M_{th}	55
A-2	Mathematical influence of the two-photon absorption constant C and exposure time t combined as Ct	56
A-3	Mathematical influence of the beam waist radius w_0	56
B-1	The fitted curves that were obtained for the voxel height and diameter experiments. . . .	59
B-2	(a) A micrograph of the voxel height and diameter test for a laser power of 3.5 mW and scanning speed 100 $\mu\text{m}/\text{s}$. (b) The measured diameter and height for laser power 3.5 mW and scanning speed 100 $\mu\text{m}/\text{s}$	59
B-3	The pore diameter measured from the initial experiment. The voxel was scanned through the material.	61
B-4	(a) An overview of the produced 3D features. (b) A micrograph of the cones. (c) A micrograph of the pyramids. (d) A micrograph of the trapeziums with one straight side.	62
B-5	(a) An overview of the produced inverse 3D features. (b) A micrograph of the inverse cones. (c) A micrograph of the inverse pyramids. (d) A micrograph of the inverse trapeziums with one straight side.	63
B-6	A cracked surface shows that both channels are there at different heights.	64
C-1	Interface signals in the Photonic Professional GT.	67
C-2	For multiple layer coating, at hydration, follow the arrow back to spincoating, until the final layer is thick enough.	69
D-1	Interfaces in the writing configuration.	72

D-2	Four different Describe designs for large pores.	73
D-3	(a) Array of open channels. (b) The predicted process time in blue and the actual process time in red.	74
D-4	(a) Parameter sweeps 10x10 μm square pores. (b) Overview of laser power vs. scanning speed for Galvo scan mode.	75
D-5	The different Describe designs made for Piezo Scan mode writing.	77
D-6	(a) Overview of trenches. (b) Closer view of two trenches. (c) Results from trench experiments.	78
D-7	(a) Dose test with scanning laser to create pores with a length of 10 μm . (b) Test to find voxel height and corresponding voxel diameter, by lowering the voxel with steps of 50 nm	79
D-8	Two images of channel intersections. The channels were not completely developed, but the pores are clearly visible.	79
D-9	Describe designs for 3D manufacturing.	80
D-10	(a) Optical image of the stamp. (b) SEM micrograph of the stamp. (c) PDMS pillars. (d) White light interferometer image from the pillars.	81
D-11	The three features that make the chip and the full chip design.	82
D-12	The stage that was designed to enable the use of the magnetic stirrer.	83
D-13	Four failed development methods.	84
E-1	High and low contrast images before and after processing.	86
E-2	The automatic pore measurement is all within 5% of human measurement, except for the situation where the human measurement was very inaccurate.	87
E-3	GUI made for combined least-squares error fit.	88
E-4	Three writing configurations.	89
E-5	SEM micrographs of needle with laser cut layer.	89
E-6	Picture on the calendar of the PME department.	90

List of Tables

1-1	Organ-on-chip properties in literature.	3
1-2	Micro manufacturing techniques. The method should be suitable for small scale production. The method should enable rapid prototyping. 3D manufacturing is desired. Other disadvantages such as the need of a mold or a predetermined shape are not desired.	5
4-1	The variables used to calculate the voxel diameter and height. The unknown variables were given an estimated value.	27

Chapter 1

Introduction

1-1 Motivation

For a medicinal drug, the road from lab to market is long. Out of thousands of substances, only 10 to 20 will eventually make it to the shelves [1]. This entire process takes on average 10-12 years [1, 2], which is mainly due to the length of the testing phase. A substance will be tested *in vitro* and *in vivo*. *In vitro* tests are taken in the lab, with cells cultured on a petri dish. The advantage of this is the possibility to do multiple tests in parallel. The main problem with this type of testing is that the natural environment of the cells is not accurately mimicked [3]. The reaction of the human body to the drug may differ from the results in the lab. *In vivo* tests are performed with lab animals. This causes ethical problems; more than 115 million animals are used in lab experiments every year [4]. Besides that, animal testing is expensive [5], and time consuming, because the animals have to be bred. After animal testing, additional tests have to be conducted with human tissue for the final approval of the drug [6].

Organ-on-chip

Because conventional testing is expensive, time consuming and ethically problematic, new ways of drug testing are desired. One solution to this problem is called organ-on-chip (OoC) technology. This technology enables the fabrication of devices that can accurately mimic the natural environment of the human body and therefore create a realistic result for the drug testing [7, 8]. An organ and its functionalities can be simulated on chip, without the need of animals. Modern manufacturing techniques allow these chips to become really small, with feature sizes in the micrometer range, saving materials and costs. OoC technology also offers the possibility to do many tests simultaneously, which would significantly reduce the required testing time compared to conventional testing.

Before the actual drug testing can take place, the OoC device must be designed and developed. The basic features that are present in such a device are microfluidic channels and

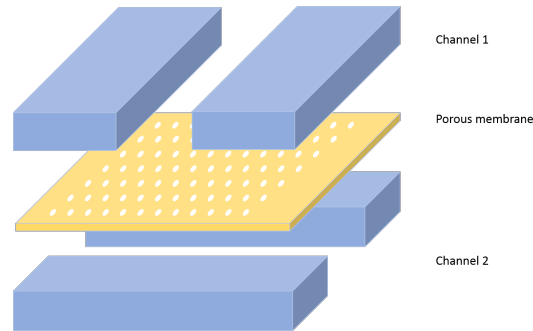


Figure 1-1: A standard microfluidic chip.

porous membranes that connect these channels [8–12]. In more complicated chips, sensors and actuators can be placed, but for this research only channels and membranes are taken into consideration. An example of a simple microfluidic system is visualized in Figure 1-1. This device consists of two channels and a connecting membrane in between. As can be seen in the example, OoC devices are assembled from multiple parts. These parts have to be designed, manufactured and tested. A small change in such a design would mean that every part has to be redesigned and the entire device has to be built again step-by-step. This way it could take a long time before a new prototype is produced. To enable rapid prototyping it could therefore be useful to find a manufacturing method that can produce these features in a single step. Eventually for the drug testing, large scale production is required, but that is not necessary in the development phase. That is why for the development of an OoC device, small scale production methods are preferred.

Channel and membrane properties

Nowadays a variety of OoC devices exist. In Table 1-1 various existing organs-on-chips and the properties of their channels and membranes are shown. Typically, the microfluidic channels are produced in-house, whereas the membranes are commercially obtained. There is a range of different membranes that are commercially available. Frequently used membranes are Transwell[®] cell culture inserts or porous sheets [13]. These inserts have pore sizes between 0.4 and 10 μm , the pore density for these membranes varies between 1×10^5 and 1×10^8 pores/ cm^2 and the membrane thickness is in the range of 10 - 50 μm . The problem with commercially obtained membranes is that they restrict the researcher to the predetermined shape, pore size, film thickness and pore density. If a change in membrane is desired, new products must be ordered and delivered, which costs time. Therefore it is desirable to find a manufacturing method that is able to produce a membrane with pores with a diameter comparable to commercial available membranes. To create an entire microfluidic system in one production step, the method must also allow single step channel manufacturing.

Research goal

The goal of this research is to find and characterize a manufacturing method that can be used for the single step fabrication of a microfluidic device consisting of two crossed channels at a different height level, connected by a membrane.

Table 1-1: Organ-on-chip properties in literature.

Application	Channel H x W	Membrane pore size	Membrane thickness	Reference
Lung-on-chip	-	10 μm	10 μm	[14]
Airway-on-chip	0.2 - 1 x 1 mm	0.4 μm	10 μm	[15, 16]
Alveolus-on-chip	0.2 - 1 x 1 mm	9 μm	25 - 50 μm	[15]
Gut-on-chip	- x 1 mm	-	20 μm	[17]
Liver-on-chip	0.1 x 1 mm	0.4 μm	10 μm	[18]
Skin-on-chip	0.15 x 0.15 mm	-	-	[19]

1-2 Manufacturing methods

There are many manufacturing techniques that can be used for the fabrication of microfluidic channels and porous membranes. However, for the manufacturing of a closed channel in a single step, the technique must offer the possibility of 3D manufacturing. For the manufacturing of a membrane that is comparable with commercially available membranes, it is desired that the technique has sub-micron resolution. In the following section frequently used techniques that can achieve sub-micron resolution will be discussed briefly and an overview with references is given in Table 1-2. It will be checked whether the manufacturing technique is suitable for small scale production, rapid prototyping and 3D manufacturing. The fourth requirement includes other disadvantages such as the need of a mold or a predetermined membrane shape.

Hot embossing

Hot embossing is a way of stamping a pattern into a polymer surface. A stamp will be pressed all the way through the polymer layer. The method is cheap for large scale production, but not attractive for small scale production. The need of a stamp is a disadvantage that makes the technique unsuitable for rapid prototyping. With a 3D stamp, a pattern can be transferred, but only such that the polymer can still be released from the stamp, thereby excluding the production of closed channels. This restriction makes it unsuitable for the application discussed in this research.

Injection molding

For injection molding, a material is melted and poured into a mold under high pressure. After cooling down the negative of the mold remains. Due to the mold, the method is cheap and fast for large scale production and not suitable for rapid prototyping. It is possible to create 3D structures. The manufacturing of the mold adds an extra production step to the process and makes the method unsuitable for the discussed application.

Nano Imprint Lithography

Nano Imprint Lithography (NIL) is another method to stamp a pattern into a polymer surface. The stamp will only go through a relatively thin part of the polymer layer. The method can be used for large scale production. Because a stamp is needed, this method is not suitable for rapid prototyping. 3D structures can be transferred, but it can not be used to create closed channels.

Electron Beam Lithography

A photoresist is a material of which the solubility can change when exposed to a source of energy. The difference between a negative and a positive-tone resist will be explained in Chapter 3. Electron Beam Lithography (EBL) exposes the photoresist to a focused electron beam, removing material with high resolution. The method is suitable for small scale production. For the scope of this project, using a negative resist does not allow rapid prototyping, whereas a positive resist does. The method can not be used for 3D manufacturing.

Focused Ion Beam Lithography

Focused Ion Beam Lithography (FIBL) makes use of an ion beam that is focused onto the surface of a photoresist. The method is suitable for small scale production and allows rapid prototyping when combined with a positive photoresist. FIB can not be used for 3D manufacturing.

Scanning Probe Lithography

Scanning Probe Lithography (SPL) is another lithography technique that is used for sub-micron fabrication. There are different ways of SPL, for example mechanical SPL, where material is scratched away, thermal SPL, where the temperature of the probe is used, or thermo-chemical SPL where chemical reactions change the surface as a result of a heated probe. SPL is suitable for small scale production and allows rapid prototyping, but it can not be used for single step 3D manufacturing.

Electrospinning

Electrospinning makes use of a polymer solution or a polymer melt. From this polymer, fibers are extracted with submicron sizes. The fibers are stacked on top of each other and form a porous membrane. This is a fast production method, but it can not be used to create specific 3D patterns. The method allows rapid prototyping and small scale production. A major disadvantage is that the 3D structure can not be controlled.

Two Photon Lithography

Two Photon Lithography (TPL) makes use of a laser that initially does not have enough energy to change the properties of a photoresist. However, in the focal point of the laser, two photons are absorbed nearly at the same time, giving enough energy to induce the change in the resist. TPL is suitable for small scale production and in combination with a positive photoresist it allows rapid prototyping and 3D manufacturing.

Many techniques can be used for sub-micron manufacturing. The methods that need a stamp or a mold are not advantageous for small scale production and do not allow rapid prototyping, since it costs time to produce a new mold or stamp. Most of the methods that do not require an extra mold or stamp, do not offer the possibility of 3D manufacturing. The only method that fits all requirements is TPL with a positive photoresist. That is why this technique will be further investigated and extensively discussed in Chapter 3.

Method	Production scale	Rapid prototyping	3D manufacturing	Other	Reference
Hot Embossing	-	-	-	-	[20, 21]
Injection Molding / Particulate Leaching	-	-	+	-	[22–24]
Nano Imprint Lithography	-	-	-	-	[25–28]
Electron Beam Lithography Negative	+	-	-	+	[29]
Electron Beam Lithography Positive	+	+	-	+	[29–32]
Focused Ion Beam Lithography	+	+	-	+	[33]
Scanning Probe Lithography	+	+	-	+	[34, 35]
Electrospinning	+	+	+	-	[36, 37]
Two Photon Lithography Negative	+	-	+	+	[38, 39]
Two Photon Lithography Positive	+	+	+	+	[40–42]

Table 1-2: Micro manufacturing techniques.

The method should be suitable for small scale production.

The method should enable rapid prototyping.

3D manufacturing is desired.

Other disadvantages such as the need of a mold or a predetermined shape are not desired.

1-3 Prior Art of TPL on a positive photoresist

The use of a positive photoresist in a TPL process is not widely researched. In literature there are two groups who used this method. In this section their work is briefly discussed.

Two-photon nanolithography of positive photoresist thin film with ultrafast laser direct writing by Cao et al. (2013)

The concept of performing TPL on a positive photoresist was first tried in 2013 by Cao et al. [41]. The authors investigated the process and tried to maximize the resolution. The experiments were two dimensional. The main goal of this work was to show the potential of this process and to provide a protocol for TPL on a positive photoresist in future studies. To get a resolution as high as possible, the authors produced nanotrenches. A laser with a wavelength of 780 nm was used and a spatial resolution of 85 nm was achieved. This resolution was achieved at a laser power of 0.330 mW. Furthermore the authors provide an equation to describe the trench width. The experimental results corresponded to the calculated values. The equation is derived in Appendix A, and is used in this research.

The photoresist used was AZ P4620. This is a commercially available photoresist meant for layer thicknesses between 6 - 20 μm [43]. This thickness is considered thick for a positive photoresist. The authors diluted the AZ P4620 with 1,2-Propanediol monomethyl ether acetate (PGMEA) with a mass ratio of 1:3, to obtain a thin layer of 145 nm thickness.

Two-photon lithography for 3D magnetic nanostructure fabrication By Williams et al. (2018)

In 2018 Williams et al. [42] used the process to make three dimensional molds for electrochemical deposition. In literature this was the only research found that makes use of the 3D manufacturing possibilities of this process. The authors created structures with sizes of up to several microns and a smallest features size of 430 nm. A laser power between 3 - 10.5 mW and a scanning speed between 5 - 25 $\mu\text{m}/\text{s}$ were varied.

After the electrochemical deposition, the resist was dissolved in acetone and the residual resist on the samples was removed by using an oxygen plasma treatment, leaving the metal structures on the substrate.

The photoresist used was AZ 9260. This is also a commercially available resist and the recommended layer thickness is between 5 - 20 μm [43].

Conclusion

There are only two groups in literature that made use of TPL on a positive photoresist. The application of single step manufacturing of microfluidic channels and a porous membrane was not explored. A research in this direction could therefore be a valuable contribution.

1-4 Planning

The initial planning of the project was divided into three phases, each with different sub-phases, deliverables and a final milestone. A Gantt chart was made, which is shown in Figure 1-2. The first phase was focused on the characterization of the process. The goal was to be able to produce sub-micron pores and to understand what was happening during the exposure and development of the resist. In the second phase the concept of 3D manufacturing was explored and in the third phase the obtained knowledge was used for fabrication of a microfluidic device in a single step. In the initial planning the release of the layer was incorporated. This was eventually not researched, because it introduces an extra step to the fabrication process and the research is about single step manufacturing.

1-5 Report outline

Following this report introduction is a paper, written for the Elsevier journal *Micro and Nano Engineering* to share the most important information acquired during this research. The paper is independent from the rest of the report. Some equations and figures are therefore repeated. Chapter 3 gives a more extensive description of TPL and the positive photoresist used in the research. The governing equations of the process are discussed and information about the setup is given. Chapter 4 discusses the results obtained in the characterization phase of the research. Chapter 5 shares the most important results that were obtained in the 3D manufacturing phase. In Chapter 6, the manufacturing of the microfluidic device is discussed. Finally the conclusions drawn from this research and the recommendations for future work are given in Chapter 7.

After the main matter of this report, there are five appendices with additional information. The first Appendix A covers the derivation of the main equation and the calculations that lead to the decisions that were made during the characterization phase. In Appendix B additional results of the most important experiments conducted in each phase are displayed. Appendix C shares the writing protocols for a TPL process on a positive photoresist. Appendix D shows the steps taken in this research. Finally in Appendix E extra work that has been done during this research can be found.

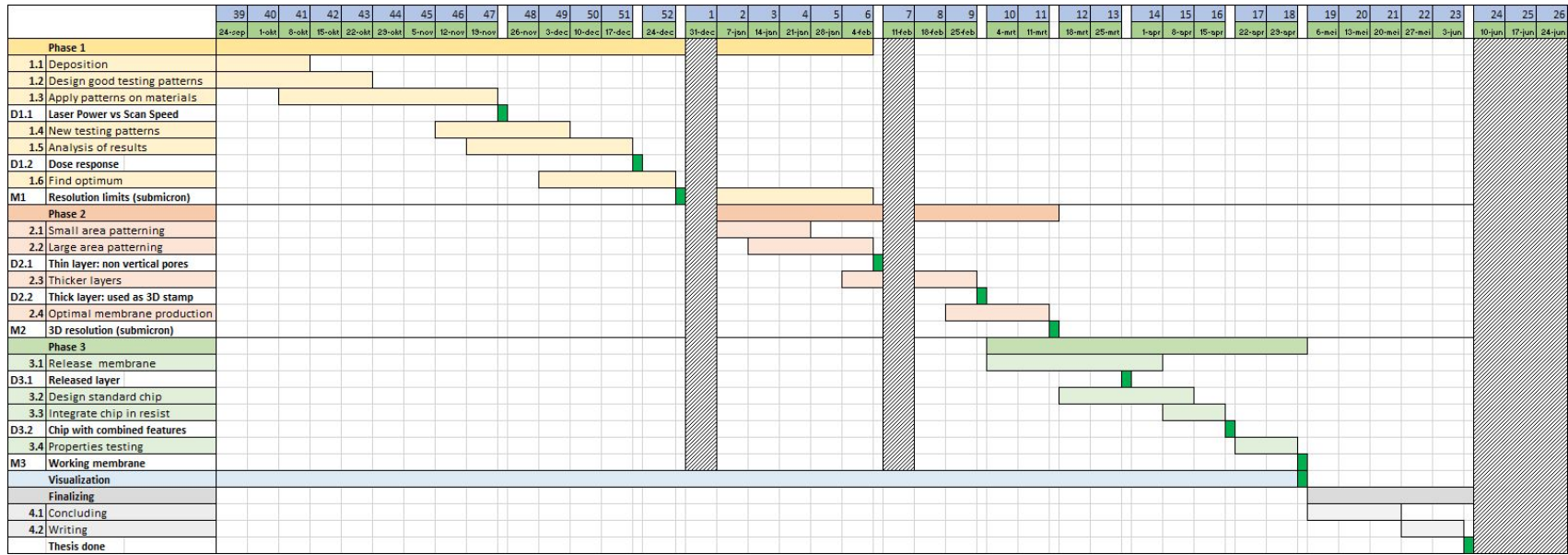


Figure 1-2: Gantt chart of the initial project planning.

Chapter 2

Paper written for Elsevier journal: Micro and Nano Engineering

The use of two-photon lithography on a positive photoresist is a topic that is not yet widely researched. The characterization phase of this research offers new insights into this method. A paper was written for the journal *Micro and Nano Engineering* from Elsevier. This paper is presented on the following pages. An abstract about this paper was submitted for the international conference on Micro & Nano Engineering, MNE2019. The paper is an independent part of the thesis. Therefore some equations and figures may be repeated in the other chapters of the report.

Fabrication of a microfluidic device by using two-photon lithography on a positive photoresist

G. van der Velden, D. Fan, U. Staufer*

Mechanical Engineering
Department of Precision and Microsystems Engineering
Delft University of Technology

Keywords: two-photon lithography, positive photoresist, voxel shape, microfluidic channel, Organ-on-Chip

ABSTRACT

Organ-on-chip (OoC) technology is increasingly used for biomedical research and to speed up the process of bringing a drug from lab to the market. The main components of an OoC device are microfluidic channels and porous membranes. Current chips are often assembled from several parts. In the development phase a small change in design will cause a delay in the research because a new prototype has to be built again step-by-step. The research discussed in this paper addresses this point by targeting a monolithic 3D device that can be fabricated in a single lithography and development step, enabling rapid prototyping. Two-photon lithography (TPL) was used in combination with a positive photoresist AZ 4562. Pore manufacturing was studied and characterized. In literature an ellipsoidal voxel shape is assumed, resulting in the largest diameter of the voxel to be at the height of the focal plane, i.e. at $z=0$. This study however, found that for certain laser powers the voxel follows the profile of the Gaussian laser beam, creating an hourglass-shape. This causes the maximum voxel and therefore pore diameter to be at a distance from the focal plane. The smallest pores produced measured 250 nm. The TPL process was used to successfully fabricate a microfluidic device featuring two crossed channels each one on a separate height-level, connected by a membrane in the center.

1 Introduction

The time for a newly developed biomedical drug to reach the market is long [1]. Currently this process takes ten to twelve years, which is mainly due to the length of the testing phase [2]. Substances are tested *in vitro*, by plain cell-culture experiments and *in vivo*, on animals. The main advantage of current *in vitro* tests is high-throughput testing by simultaneously operating many devices in parallel. OoC technology shares this advantage, but it produces more relevant results, as it offers the possibility to mimic the environment in the human body [3], similar to *in vivo* testing. However, animal testing causes ethical issues, it is time consuming and expensive [4]. OoC technology addresses these issues, because it offers a significant reduction in the number of animal tests done each year. After animal testing, additional tests have to be conducted using human tissue for the final approval of the drug [5]. These tests could also be reduced by testing with OoC devices.

The main components of an OoC device are microfluidic

channels and porous membranes [6]. Typically, channels are fabricated in-house while membranes are usually purchased commercially [7]. Current chips are often assembled from several parts. In the development phase a small change in design will therefore cause a long delay in the research because a new prototype has to be built and some components have to be purchased and delivered. Therefore it can be said that the current development of OoC devices does not offer the possibility of rapid prototyping. In this research a method of channel and membrane manufacturing is proposed that can fabricate the main components of an OoC device in a single lithography and development step.

Two-photon lithography (TPL) is a direct laser writing method, that is currently used in many micro fabrication applications [8–12]. TPL exploits the fact that a two-photon process depends non-linearly on the light intensity [8]. The required intensity is only achieved in a small volume around the focal point of the laser, called the voxel [9]. The shape of this voxel is assumed to be ellipsoidal, leading to the assumption that the maximum diameter of the voxel is found

*Correspondence to this author

at the height of the focal plane, i.e. at $z = 0$ [9, 10]. The laser can be focused within the photosensitive resin, and by moving the voxel around, three dimensional structures can be created. In earlier research, TPL is nearly always used in combination with a negative photoresist, called two-photon polymerization (2PP) [13]. However, for this research that would significantly increase the processing time. For the application of single step channel and membrane manufacturing, TPL was used on a positive photoresist. This allows fast production of a complete microfluidic device featuring two crossed channels separated by a membrane, in one lithography and development step.

2 Theory

TPL makes use of the two-photon absorption (TPA) of a photosensitive molecule. The photoresist used in this research consists of Novolac as backbone polymer and diazonaphthoquinone (DNQ) as photosensitive molecule [14]. The main function of DNQ is an inhibitor to the dissolution of the surrounding Novolac. During exposure the DNQ is functionalized with carboxylic acid groups (COOH). The COOH-groups make the DNQ more soluble and easily removed when immersed in a caustic-water developer solution. Once the DNQ is removed, the surrounding resin will also be dissolved in the solution.

The process of TPL on a positive photoresist can be described by Eq. (1). Here M is the unexposed DNQ, M^* is the excited DNQ and P is the relative amount of DNQ that reacted was functionalized with a COOH-group.



It is well known that the amount of excited DNQ reaches equilibrium quickly [15]. Therefore the second rate equation can be written as $\frac{dM^*}{dt} = 0$ and can be used to solve the rate equations and obtain Eq. (2).

$$M = M_0 \exp\left(\frac{-k_1 k_3}{k_2 + k_3} t_I\right). \quad (2)$$

M_0 is the initial amount of DNQ present in the resist, k_1 is the rate at which M is excited, k_2 is the rate at which the excited DNQ molecules fall back to the initial state and k_3 is the rate constant describing the transition from the excited DNQ to the product, functionalized with a COOH-group. Finally t_I is the interaction time between the laser and the photoresist.

The rate equations and the interaction time are described by Cao et al. [11], who also used these relations to obtain a final expression describing the voxel diameter at distance z from the focal plane. This equation is given in Eq. (3) and was

only used to determine the voxel width. In this research the equation is used to define the exact voxel shape.

$$d(z) = w(z) \sqrt{\ln\left(\frac{4C\eta^2 P_{laser}^2 t}{f\tau(\pi h\nu w^2(z))^2 \ln\frac{M_0}{M_{th}}}\right)}. \quad (3)$$

In Eq. 3, η is the transmittance of the objective lens, P_{laser} is the laser power, t is the exposure time during the process, f and τ are the repetition rate and the pulse width of the laser respectively, h is Planck's constant, ν is the light frequency and M_{th} is the material threshold value for the dissolvable amount of DNQ. The beam radius $w(z)$ at distance z from the focal plane is described by Eq. (4), where w_0 is the beam waist radius and f_L the Rayleigh length [12]. Finally C is a material constant related to TPA, described by Eq. (5). Here Φ is the quantum efficiency, δ the TPA cross-section, A_E is Einstein's coefficient of spontaneous emission and C_0 is a material constant.

$$w(z) = w_0 \sqrt{1 + \left(\frac{z}{f_L}\right)^2}, \quad (4)$$

$$C = \frac{\Phi\delta C_0}{A_E + C_0}. \quad (5)$$

The voxel height can be expressed as $2z$, where z is the largest distance from the focal plane where $d > 0$.

To simplify the modeling and fit the equation on the obtained data, the constant C , the exposure time t and the material threshold value M_{th} were combined into variable K_{CTM} , given in Eq. 6. The other fitting variable is the beam waist radius w_0 .

$$K_{CTM} = \frac{Ct}{\ln\left(\frac{M_0}{M_{th}}\right)}. \quad (6)$$

Fabrication

A 10 μm thick layer of positive-tone photoresist AZ 4562 (Microchemicals GmbH, Ulm, Germany) was spincoated on a 170 μm thick glass slide (Menzel-Gläser, Bad Wildungen, Germany). After spincoating, a softbake at 110°C for 5 minutes was performed (SPS Polos Hotplate). Finally before exposure the sample was hydrated in air for 15 minutes. The specimen was exposed using TPL (Photonic Professional GT, Nanoscribe, Germany) via an objective lens (magnification 63x, numerical aperture 1.4). A laser with a mean laser power of 50 mW, a wavelength of 780 nm, 80 MHz repetition rate and a pulse width of 100 fs was used. During exposure, laser powers between 0.5 and 5 mW were used with a scanning speed that was varied between 10 - 100 $\mu m/s$. After exposure the sample was developed in an AZ 400K Developer (Microchemicals GmbH) diluted with deionized water in a 1:4 ratio.

The pores were fabricated by scanning the voxel through the resist in vertical direction. For the testing of the voxel height and shape, the voxel was lowered into the resist with steps of 50 nm, starting 0.5 - 1 μm above the surface of the resist. This value depended on the tilt of the sample. After edge bead removal (EBR) and tilt correction there was still a tilt between 0 - 0.25°. The lowering of the focal point into the resist is illustrated in Figure 1.

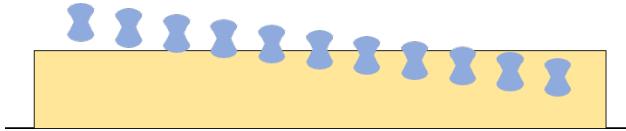


Fig. 1: The voxel was lowered into the resist with steps of 50 nm.

For the manufacturing of the channels, multiple layers of 10 μm were spincoated on top of each other, up to a resist thickness of 50 μm. The exposure was performed with a 10 mW laser power and a scanning speed of 20 mm/s. This increased the processing speed and decreased resolution. Voxel characterization is not possible at such a high scanning speed due to limitations in acceleration of the machine. The channels were developed for 80 minutes, during which the developer solution was stirred with a magnetic stirrer (IKA Labortechnik RH basic).

Measurements

For the measurement of the pores, the sample was sputter coated (SC7620, Quorum Technologies) with gold or gold/palladium layers with a thickness of around 5 nm. The coated sample was imaged in a scanning electron microscope (SEM, Jeol JSM-6010LA) and the measurements were done with the SEM software and a custom-made MATLAB script.

The channels were imaged with an optical microscope (Keyence Digital Microscope VHX-6000), a white light interferometer (Bruker) and the SEM.

3 Results and discussion

The data obtained from the voxel diameter and height experiments was combined in a model where the main equation was fitted for K_{CIM} and w_0 . The average result of three individual measurements for a scanning speed of 40 μm/s is shown in Figure 2a. The fitting values found were $K_{CIM} = 2.75 \times 10^{-60}$ and $w_0 = 125.14 \text{ nm}$. For a laser power of 1 mW and higher, the experimental data and the theory correspond well, so this model could be used in future research for rough predictions of the voxel dimensions. Similar curves were found for this experiment at scanning speeds between 10 - 100 μm/s. The fitted values for the beam waist radius were between 119.45 - 127.13 nm, with an average of 123.79 nm. The fitted values for K_{CIM} decreased linearly with the decreasing scanning speed.

The found value for w_0 is slightly smaller than expected from literature [10]. A cause of this difference could be the refractive index of the photoresist. The refractive index of AZ 4562 was estimated based on the research done by Cao et al. who used similar photoresist AZ P4620 [11]. If the actual refractive index is lower than estimated, this would result in a smaller beam waist radius. Other causes of the different beam waist radius could be lens aberrations or systematic errors in the optical path of the laser. Small fluctuations in the laser power could explain the variation in the obtained values for w_0 .

The exposed voxel that was lowered step-by-step into the resist for a scanning speed of 40 μm/s and a laser power of 3.5 mW is shown in Figure 2b. It can be observed that the diameter of the pores in row 3, column 4 and 5, is smaller than the diameter of the surrounding pores. This is where the laser is focused at exactly the height of the surface of the resist. When the laser is focused higher or lower than the surface, the diameter of the pores increases at first, then decreases and abruptly stops. This picture shows that if the laser intensity is high enough further away from the focal plane, TPA is initiated in a larger area than at the waist of the beam. Consequently a larger amount of material is removed in the developer. For the modeling of the pore diameter, this would mean that the maximum voxel diameter instead of the diameter at $z = 0$ should be taken into account.

The voxel diameter depends on the laser power and the exposure time, but also on the distance z from the focal plane. Using this dependency, a profile of the voxel can be modeled. The fitting parameters obtained were used for a laser power of 3.5 mW. The result of the model is shown in Figure 2c. and it can be observed that the shape is not an ellipsoid. The predicted voxel shape follows the profile of the Gaussian laser beam and has an hourglass-like shape. The dots display the measured voxel diameter and height obtained from 2b. The measured voxel dimensions also show the hourglass shape. The actual diameter at the beam waist is larger than modeled. This could be caused by diffusion of the functionalized DNQ into the unexposed material. There will be more diffusion near the waist of the beam than at the distance z where the maximum diameter is found, because the DNQ will diffuse in all directions. Another cause of the size difference could again be aberrations in the optical system. The actual voxel height is slightly higher than calculated. The datapoints for a diameter of 0 are drawn 50 nm above and below the voxel. In reality the real voxel top and bottom can be anywhere within this extra step of 50 nm.

The shape of the voxel strongly depends on the laser power. The positive resist has a very low threshold value and the laser is operated at low power. The predicted cross-section of the voxel for laser powers between 0.1 - 5 mW is shown in Figure 2d. The first laser power for which the maximum voxel diameter occurs at $z = 0$ again, shows a voxel with a cigar shape. As the laser power gets even lower, the expected shape will look like an ellipsoid again.

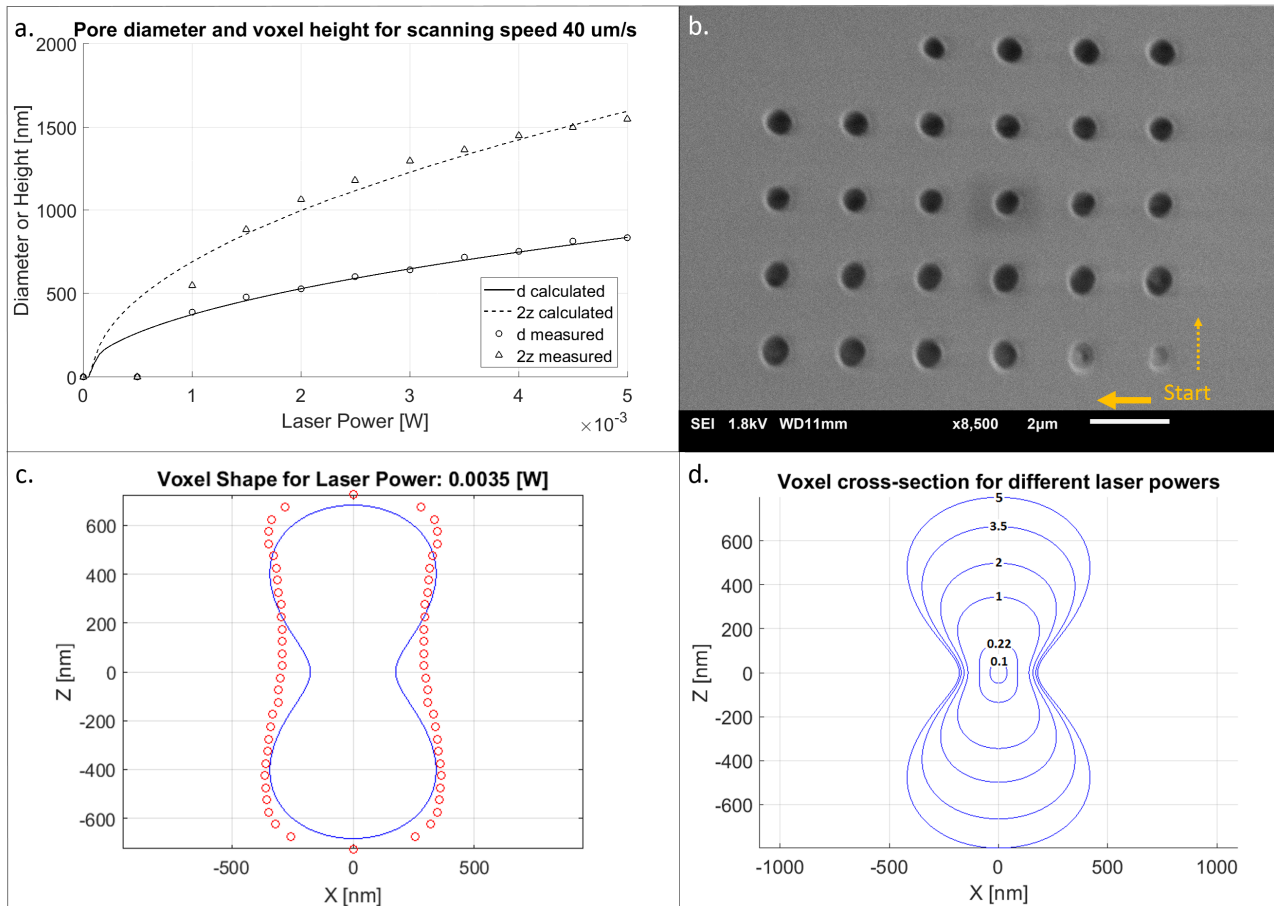


Fig. 2: a.) Model fit on the measurements. The circles indicate the voxel diameter and the triangles indicate the voxel height, which is twice the distance z from the focal plane. b.) Micrograph of the voxel diameter and height test by lowering the voxel with steps of 50 nm , from right to left, starting in the lower right corner and then rastering upwards. The scanning speed was $40\ \mu\text{m/s}$ and the laser power was $3.5\ \text{mW}$. c.) The 2D model of the voxel shows an hourglass-like shape. The measured data is added with red circles. The diameter is smaller at the waist, i.e. where $z = 0$. The maximum diameter lies at $z = 550\text{ nm}$ in the measurements and at $z = 450$ in the model. d.) The cross-section of the voxel changes with laser power. As the laser power increases, the voxel takes a more hourglass-like shape. The laser power is indicated in mW for each profile.

Pores and channels

The smallest pores that were produced were around $250\ \text{nm}$ in diameter. They were produced with a scanning speed of $30\ \mu\text{m/s}$ and a laser power of $0.5\ \text{mW}$. This laser power did not initiate TPA for a scanning speed of $40\ \mu\text{m/s}$, which is due to a shorter exposure time. A lower scanning speed corresponds to a longer exposure time. With a lower scanning speed, a laser power of $0.5\ \text{mW}$ could therefore still create a laser dose that is high enough to initiate TPA.

In theory it should be possible to produce pores with a diameter smaller than $250\ \text{nm}$. The voxel dimensions can be limited by laser properties. The beam waist radius could restrict the minimum voxel size. The experiments show that for AZ 4562, TPA is initiated at very low laser powers. At such low laser powers shot noise can come into play, which could also be a limiting factor. A solution could be the use of a positive-tone resist with a lower refractive index and a higher threshold intensity for TPA. A third reason for the size difference could be the diffusion of the functionalized DNQ

into the unexposed resist. Keeping the specimen cool could reduce the diffusion. Finally dark erosion can be a cause of the size limitations. The developer solution also affects the unexposed resist [16].

Channels from different sizes were produced, with an inlet and an outlet hole. The diameter of the holes was based on the diameter of the smallest blunt needle available ($210\ \mu\text{m}$). Figure 3a shows an optical image of the channels. A micrograph of the same channels is shown in Figure 3b, proving that the channels are inside the resist. Finally the microfluidic device consisting of two perpendicular channels separated by a membrane was produced. An optical image of this device is shown in Figure 3c. The length of the channels is $350\ \mu\text{m}$ and they are separated by $10\ \mu\text{m}$ in height. At the intersection of the channels the pores of the membrane are visible. The micrographs in Figure 3d and 3e show a zoomed in picture of in- or outlet holes with a height of $50\ \mu\text{m}$. The entrance of the channels is visible. Due to dark erosion, the channels are slightly wider at the entrance to the holes.

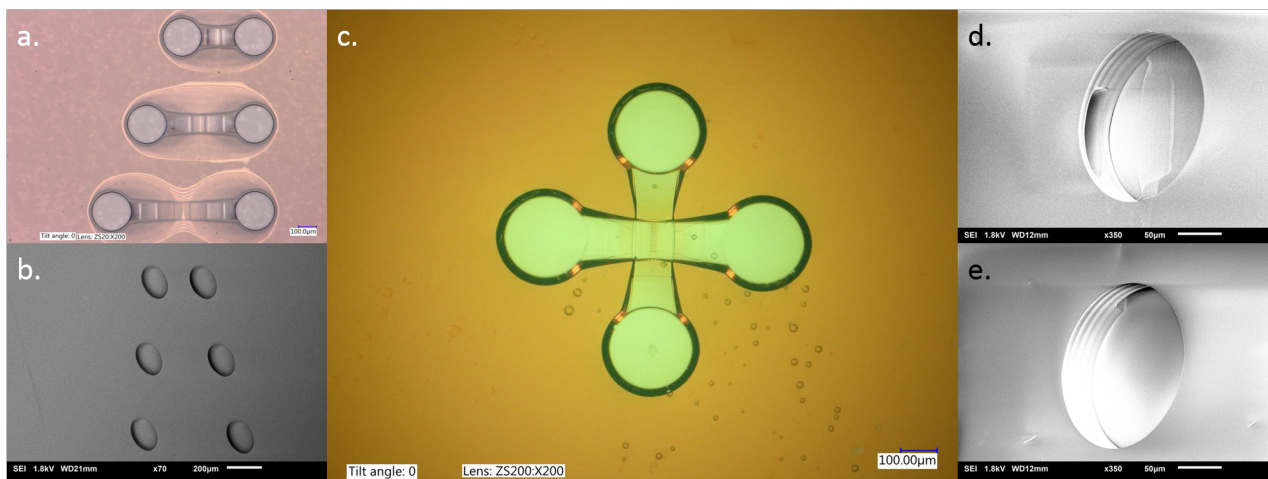


Fig. 3: a.) Optical image of three fully developed channels with a width of $100\ \mu\text{m}$ and a length of respectively 180 , 380 and $580\ \mu\text{m}$. The scale bar measures $100\ \mu\text{m}$. b.) SEM micrograph of the three channels under a 45° angle. The scale bar measures $200\ \mu\text{m}$. c.) Optical image of a fully developed microfluidic device with two perpendicular channels at different depth in the resist. The width of the channels is $100\ \mu\text{m}$ and the height is $10\ \mu\text{m}$. The inlet and outlet holes have a diameter of $210\ \mu\text{m}$. d.) SEM micrograph under a 45° angle of an in- or outlet hole for the higher channel. The scale bare measures $50\ \mu\text{m}$. e.) SEM micrograph of an in- or outlet hole for the lower channel.

4 Conclusions

A new method was used for the single step fabrication of a microfluidic device consisting of two channels and a membrane. Two-photon lithography was used on a positive-tone photoresist AZ 4562. Pore characterization showed that when the light intensity is high enough to also initiate two-photon absorption further away from the focal plane, the voxel shape follows the Gaussian beam profile and takes an hourglass shape. The maximum voxel diameter, and therefore pore diameter is not found at the focal point of the laser, but at a distance z from the focal plane. Experiments showed that the voxel indeed takes the hourglass shape. Therefore, for the fabrication of high resolution pores, the maximum voxel diameter has to be taken into account during the writing procedure. The smallest pores created were $250\ \text{nm}$. The channels in the fabricated microfluidic device have a width of $100\ \mu\text{m}$, a height of $10\ \mu\text{m}$ and a length of $350\ \mu\text{m}$. The channels are separated by a height level of $10\ \mu\text{m}$.

References

- [1] I. Torjesen, "Drug development: the journey of a medicine from lab to shelf," 2015.
- [2] J. Endres, "The drug development process: From the lab to your medicine cabinet,," 2017.
- [3] G. Hamilton, "Body parts on a chip," 2013.
- [4] K. Groff, E. Bachli, M. Lansdowne, and T. Capaldo, "Review of Evidence of Environmental Impacts of Animal Research and Testing," *Environments*, vol. 1, pp. 14–30, jun 2014.
- [5] Theodora Capaldo, "Animal Data Is Not Reliable for Human Health Research," 2014.
- [6] N. S. Bhise, J. Ribas, V. Manoharan, Y. S. Zhang, A. Polini, S. Massa, M. R. Dokmeci, and A. Khademhosseini, "Organ-on-a-chip platforms for studying drug delivery systems," *Journal of Controlled Release*, vol. 190, pp. 82–93, sep 2014.
- [7] T. Pasman, D. Grijpma, D. Stamatialis, and A. Poot, "Flat and microstructured polymeric membranes in organs-on-chips," *Journal of the Royal Society Interface*, vol. 15, p. 20180351, jul 2018.
- [8] L. Li and J. T. Fourkas, "Multiphoton polymerization," *Materials Today*, vol. 10, no. 6, pp. 30–37, 2007.
- [9] S. Maruo, O. Nakamura, and S. Kawata, "Three-dimensional microfabrication with two-photon-absorbed photopolymerization," *Optics Letters*, vol. 22, p. 132, jan 1997.
- [10] X. Zhou, Y. Hou, and J. Lin, "A review on the processing accuracy of two-photon polymerization," *AIP Advances*, vol. 5, p. 030701, mar 2015.
- [11] H. Z. Cao, M. L. Zheng, X. Z. Dong, F. Jin, Z. S. Zhao, and X. M. Duan, "Two-photon nanolithography of positive photoresist thin film with ultrafast laser direct writing," *Applied Physics Letters*, vol. 102, p. 201108, may 2013.
- [12] G. Williams, M. Hunt, B. Boehm, A. May, M. Taverne, D. Ho, S. Giblin, D. Read, J. Rarity, R. Allenspach, and S. Ladak, "Two-photon lithography for 3D magnetic nanostructure fabrication," *Nano Research*, vol. 11, no. 2, pp. 845–854, 2018.
- [13] L. Li, M. Hong, M. Schmidt, M. Zhong, A. Malshé, B. Huis In'Tveld, and V. Kovalenko, "Laser nanomanufacturing - State of the art and challenges," 2011.
- [14] S. A. Campbell, *The science and engineering of micro-electronic fabrication*, vol. 34. 2 ed., 2013.
- [15] J. Albers, "Intensity Dependence of Photochemical Reaction Rates for Photoresists," *Journal of The Electrochemical Society*, vol. 127, p. 1400, jun 2006.
- [16] WwwMicroChemicalscom, "Basic Chemistry of Developers," tech. rep.

Methods and materials

In this chapter the concept of TPL in general will be explained more extensively and the different types of photoresists that can be used will be compared and discussed. The equations that describe this process are given, followed by information about the setup that was used.

3-1 Photon Energy

The TPL process makes use of the energy of a laser. The photons in the laser have energy which is transferred when the light hits the exposed material. The energy of a single photon is directly proportional to the wavelength of the light. This amount of energy can be described by Planck's Law, given in Eq. (3-1), where h is Planck's constant, c the speed of light and λ is the wavelength of the light.

$$E_{ph} = \frac{hc}{\lambda} \quad (3-1)$$

As can be derived from this equation, the energy of a photon will increase as the wavelength of the light decreases. This is visualized in Figure 3-1. Visible light has a wavelength between 380 and 780 nm [44]. When the wavelength gets shorter than 380 nm , the light is called Ultra-violet (UV). A wavelength shorter than 10 nm gives X-rays and finally, if the wavelength gets smaller than 0.01 nm , we get gamma rays. Light with a wavelength between 780 nm and 1 mm is called Infrared (IR) [45]. At the beginning of the IR spectrum, light is considered to be Near Infrared (NIR), this is typically at a wavelength of 780 nm .

3-2 Introduction to Photolithography

Photolithography is a method where light is used to illuminate a light-sensitive material, changing the properties of this material. Materials used for this process are called photoresists. The different types of photoresists will be explained more extensively later in this chapter. For conventional photolithography, UV light is used because of its high energy photons [46].

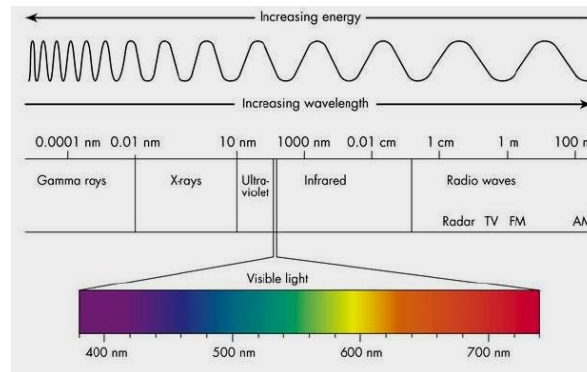


Figure 3-1: The energy of light is related to the wavelength. *Image from Hudedmani, et al.*

Introduction to photoresists

The different types of photoresists can initially be divided into two groups: the positive and the negative-tone resists [47]. These two groups can be distinguished by looking at the material that remains on the substrate after being exposed to the light. A positive photoresist consists of a hard backbone polymer and a light-sensitive molecule. The resist becomes more soluble when exposed. This can also be called the depolymerization of the material. A negative photoresist contains monomers or oligomers that are not crosslinked. By exposing a negative resist to enough energy, crosslinks are formed between the monomers or oligomers, making the material locally less soluble. This process can be called polymerization of the material.

After the exposure, the material will be developed, meaning that the soluble parts of the resist will be removed. This is done by immersion or spraying with a developer solution. For both types of resists, the parts of the material that are more soluble will be removed, leaving the less soluble parts on the substrate. To illustrate the difference, an example with a mask is given in Fig. 3-2. The mask is not light-sensitive. For a positive photoresist, the exact pattern of the mask will remain on the substrate. For a negative resist, the exact negative of the mask will remain on the surface.

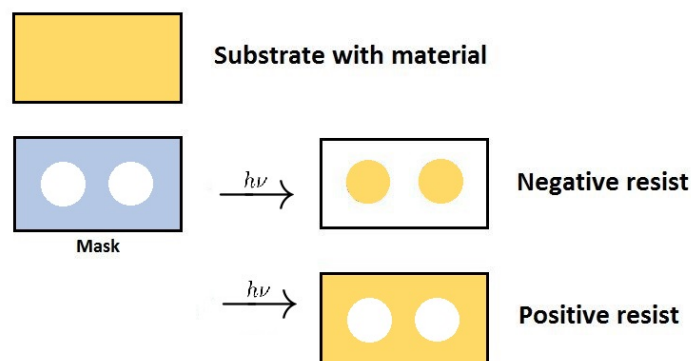


Figure 3-2: The difference between a negative and a positive photoresist, illustrated with help of a mask.

Photon Absorption

Photolithography is possible thanks to a physical process called photon absorption. In a photoresist light-sensitive molecules are present. The electrons in these molecules are initially in their lowest energy state, called the ground state. By the absorption of energy, in this case transferred by a photon, an electron can get excited and move to a higher energy state [48]. Depending on the type of molecule, this results in different reactions. For single-photon absorption (SPA), one photon transfers enough energy to get the electron to a higher state. The absorption of the photons by the electrons linearly depends on the intensity of the light. The result is that for a high enough power, anywhere in the exposed volume, the molecules are excited. The transfer to a higher energy state is shown in Figure 3-3a.

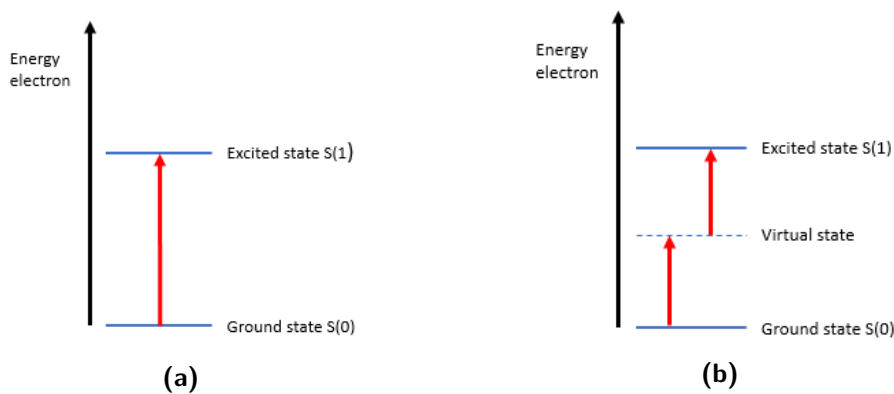


Figure 3-3: (a) Electron jump by single-photon absorption. (b) Electron jump via virtual state by two-photon absorption.

Two-photon absorption

In a TPL process, NIR-light with a large wavelength is used, and one photon can not transfer enough energy to an electron to bring it to the excited state. The photon energy is still absorbed, resulting in the electron jumping to an intermediate energy level, called a virtual state [49]. From quantum mechanics it is known that an electron cannot stay in between two states, so it will jump back to the ground state almost instantly, releasing the absorbed energy in the form of heat or vibrations [48]. If a second photon could be absorbed before the electron returns to the ground state, enough energy can be transferred to bring the electron to the excited state and induce a reaction in the photosensitive molecule. So in this very short period of time, the electron has to absorb two photons, hence two-photon absorption (TPA). The minimum time that this virtual state exists can be determined by using Heisenberg's Energy-Time uncertainty principle [50], shown in Eq. (3-2a) and (3-2b). Here $\hbar = \frac{h}{2\pi}$ is the reduced Planck constant. The electron jumping via the virtual state to the excited state is shown in Figure 3-3b.

$$\Delta\tau\Delta E \geq \frac{\hbar}{2} \quad (3-2a)$$

$$\tau = \frac{h}{4\pi E_{ph}} \quad (3-2b)$$

E_{ph} can be calculated from Eq. (3-1). With a wavelength of 780 nm this results in a photon energy of $2.55 \times 10^{-19}\text{ J}$. Substituting this in Eq. (3-2b) gives a time uncertainty of $2.07 \times 10^{-16}\text{ s}$, which is the approximated time that the virtual state exists.

This is the timespan in which a second photon of the same energy needs to be absorbed in order to reach the real excited state, which is normally reached by the absorption of one UV-photon. The absorption of two photons in this short period of time does not happen everywhere in the area that is exposed. The TPA rate depends quadratically on the intensity of the light. The governing equations showing this dependency are treated later in this chapter. In most of the exposed volume there are never two photons present in the short amount of time necessary. To expose the photoresist to a high density of photons, a femtosecond laser is used, sending an ultrashort pulse of light [38–42, 51]. When this pulse gets near its focal point, the local density of photons gets even higher. Finally, in the small volume element around the focal point, called a voxel [52], the photon density is so high that the electrons can absorb two photons fast enough to get to the excited state. The result is a much smaller volume element in which reactions take place. By moving this focal point through the resist, it is also possible to create three dimensional structures. The difference in exposed volume between conventional photolithography and TPL is visualized in Figure 3-4, created by Nanoscribe GmbH [53].

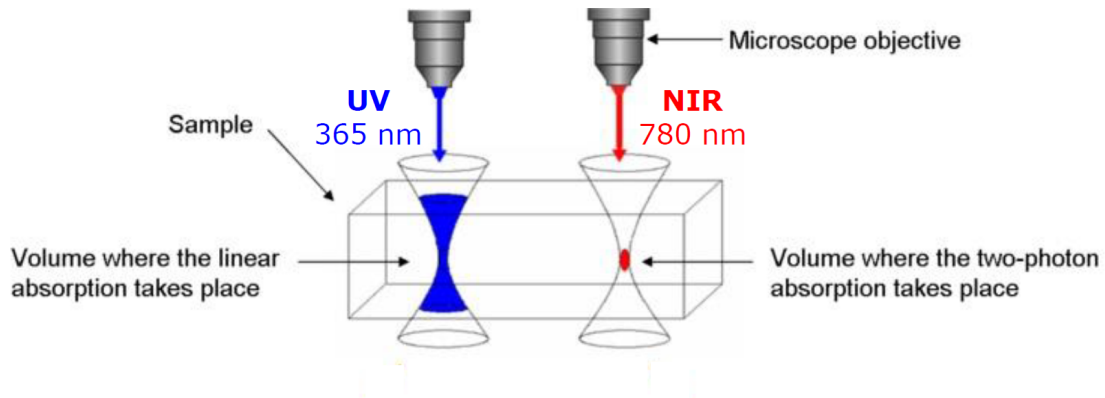
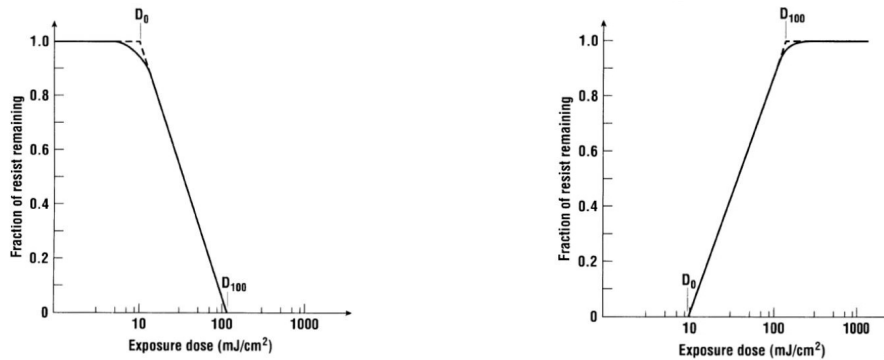


Figure 3-4: Exposed volume of UV and NIR light, By Nanoscribe.

3-3 Positive photoresists

The manufacturing method chosen in this research is TPL in combination with a positive-tone photoresist. Positive-tone photoresists are generally used as masks in conventional photolithography. When a positive resist is used as a mask, the material is meant to be fully removed at the exposed areas. For this application, the main way to express the response of a photoresist to a certain amount of energy, is by using a contrast curve [54]. This curve displays the energy dose versus the percentage of the material that is removed. In Fig. 3-5a and 3-5b the typical contrast curves are shown for a positive and negative-tone resist respectively.



(a) Contrast curve for a positive photoresist (b) Contrast curve for a negative photoresist

Figure 3-5: Contrast curves, *By Campbell: The Science and Engineering of Microelectronic Fabrication.*

TPL with a positive photoresist

When looking at 3D manufacturing, only the material near the focal point of the laser must be removed, instead of the entire layer of resist. Therefore, the contrast curve is not the most relevant way to describe the dose response in a TPL process. The best way to visualize the dose response for this process is by showing the relation between the voxel size and the laser power. This will look like the picture taken from Cao et al. [41], shown in Figure 3-6.

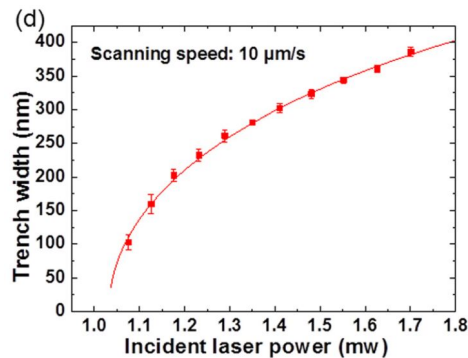


Figure 3-6: The most relevant way to describe TPL with a positive photoresist is with a graph showing the voxel size for different laser powers. *Image by Cao et al.*

3-4 AZ 4562

The material that was chosen for this research is a positive photoresist called AZ 4562, bought from Microchemicals GmbH. This material was chosen because it can be used for multilayer coating, giving the possibility to create thicker layers, which is desirable for the channel manufacturing. The material is also sensitive to light with a wavelength in the range of 320 - 420 nm, which is good for NIR light [55]. The developer solution used in this research is AZ 400K from Microchemical GmbH, diluted with deionized water in a 1:4 ratio.

Chemical reaction

In a negative-tone photoresist, when exposed, crosslinks are formed between monomers in the solution. This however, does not mean that in a positive resist crosslinks are broken. For the resist used in this research a different reaction takes place, which will be described in this section. AZ 4562 is Novolac based. This is a polymer with the shape shown in Fig. 3-7a [55]. Novolac is not photosensitive and only acts as the polymer backbone of the resist.

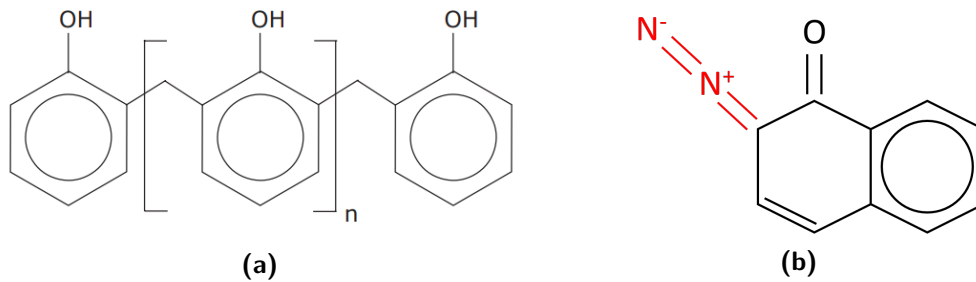


Figure 3-7: (a) Novolac is the backbone of the AZ resist. (b) DNQ is the photosensitive molecule in the resist.

Besides Novolac, there are diazonaphthoquinone (DNQ) molecules present in the material. This is the light-sensitive molecule in the photoresist. The initial molecular composition of DNQ is shown in 3-7b. The photosensitive part of the molecule is the Nitrogen group shown in red. Initially, DNQ is not dissolvable in a caustic-water mix. The unexposed DNQ also inhibits the Novolac from dissolving. The working of this inhibition is not well understood. When the resist is exposed, the N_2 -group will release, leaving a radical Carbon atom in the molecule, shown in Fig. 3-8a. After the initial reaction, a molecular reconstruction called a Wolff rearrangement takes place, shown in Fig. 3-8b. Finally in reaction with water, the DNQ is functionalized with a carboxylic acid (COOH), this is shown in green in Fig. 3-8c. This COOH-group makes the DNQ more dissolvable in a caustic-water solution. Therefore, when the resist is immersed in this solution, the exposed DNQ will dissolve and stop the inhibition from dissolving of the nearby Novolac molecules. The Novolac will then also dissolve and the unexposed material will remain on the substrate. For the manufacturing of closed channels it is important to notice that the developer solution needs access to the exposed volume in order to dissolve the resist.

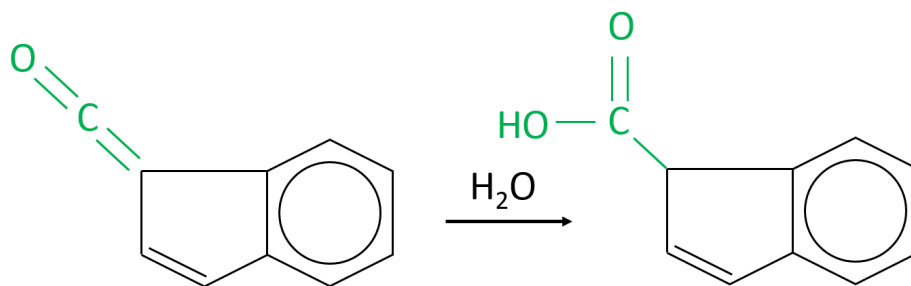
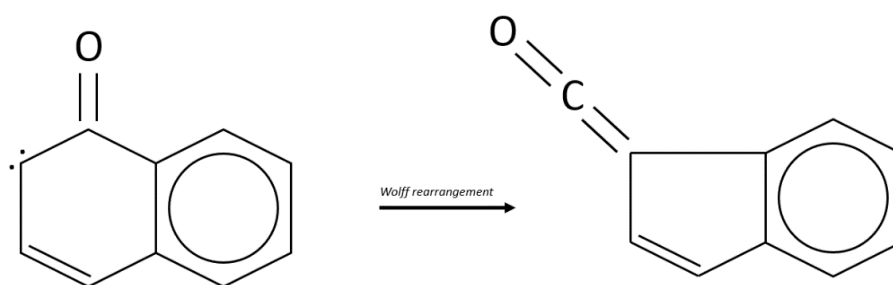
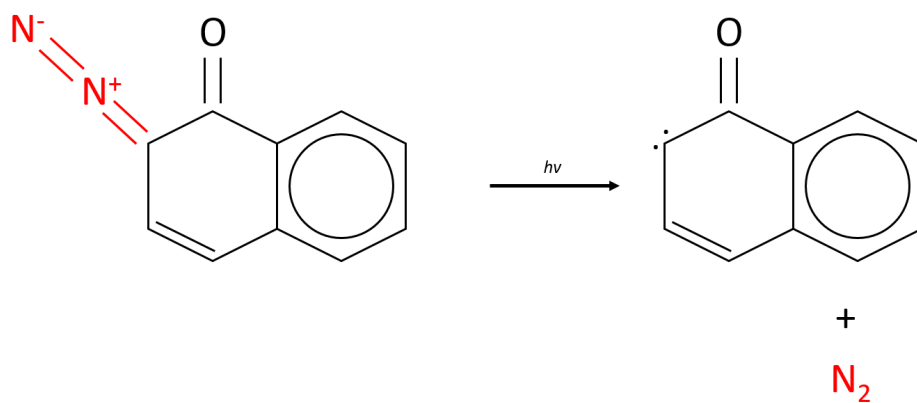


Figure 3-8: The three steps of the chemical reaction that occurs when DNQ is exposed to a laser with sufficient energy to initiate TPA.

Governing equations

This section describes the governing equations of a TPL process on a positive-tone photoresist. Some of the equations are mentioned in the paper presented in Chapter 2, but are repeated for the reader's convenience.

The main relation describing TPL on a resist like AZ 4562 is shown in Eq. (3-3). Here M is the unexposed DNQ, which is initiated at rate k_1 to obtain excited DNQ, referred to as M^* . If the excited DNQ does not react fast enough, it can turn back to the initial state. This happens at rate k_2 . It can also react and form a COOH-group resulting in the product P . This which happens at rate k_3 .



From Eq. (3-3) the following three rate equations can be obtained:

$$\frac{dM}{dt} = k_2 M^* - k_1 M \quad (3-4a)$$

$$\frac{dM^*}{dt} = k_1 M - (k_2 + k_3) M^* \quad (3-4b)$$

$$\frac{dP}{dt} = k_3 M^* \quad (3-4c)$$

It is known that the excited DNQ reaches equilibrium very quickly [56]. Therefore the amount of M^* does not change anymore and the second rate equation can be written as $\frac{dM^*}{dt} = 0$. This can be used to solve the rate equations and obtain Eq. (3-5).

$$M = M_0 \exp\left(\frac{-k_1 k_3}{k_2 + k_3} t_I\right). \quad (3-5)$$

M_0 is the initial amount of DNQ present in the resist. The rate constants k_1 , k_2 and k_3 can be described by Eq.(3-6a), (3-6b) and (3-6c) respectively. The interaction time t_I between the laser and the photoresist can be described by (3-6d) [41].

$$k_1 = \Phi \delta \left(\frac{I}{h\nu f\tau}\right)^2, \quad (3-6a)$$

$$k_2 = A_E, \quad (3-6b)$$

$$k_3 = C_0, \quad (3-6c)$$

$$t_I = t f \tau. \quad (3-6d)$$

In the rate equations Φ is the quantum efficiency, δ is the two photon absorption cross-section, h is Planck's constant and ν is the light frequency. f, τ and t are the is repetition rate, the pulse width and the exposure time of the laser respectively. A_E is Einstein's coefficient of spontaneous emission and C_0 is a material constant. Finally I is the laser intensity, which is discussed in the next section. This information can be used to derive the equation that is used for the characterization of the process of TPL on a positive photoresist, discussed in Chapter 4. An overview of the parameters is given in Table 4-1.

3-5 The setup

The setup used for this research is a TPL device by Nanoscribe GmbH called the Photonic Professional GT, shown in Figure 3-9. The machine has a femtosecond laser with a wavelength of 780 nm. In this research a 63x objective with a numerical aperture (N_A) of 1.4 was used. The mean laser power for this objective is 50mW. The focal point can be positioned with a piezo actuator for high resolution, or with galvano mirrors for high process speed.

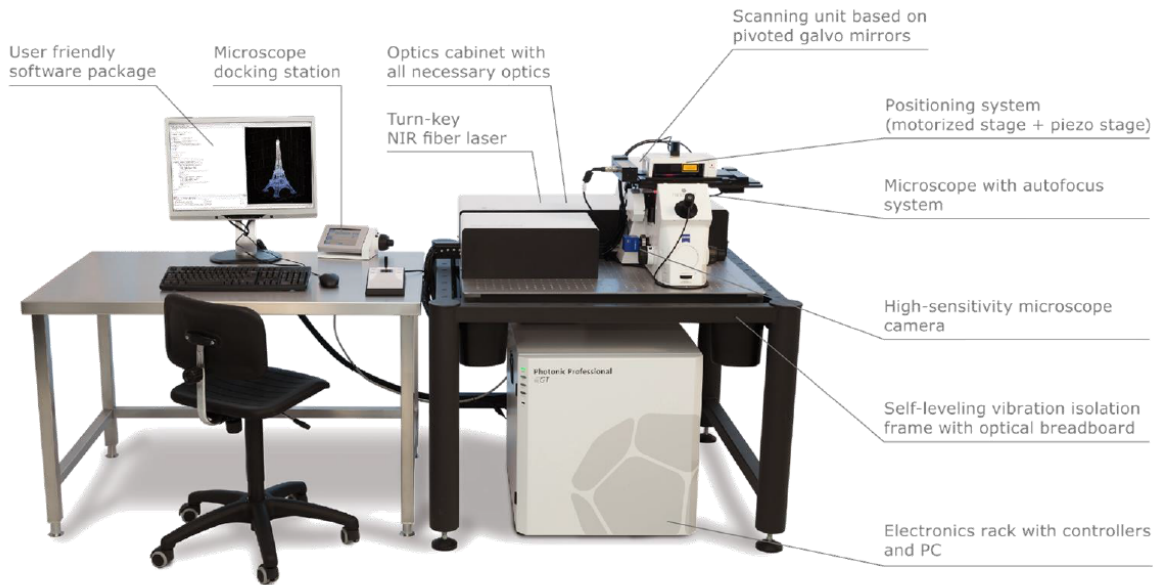


Figure 3-9: The Photonic Professional GT, *By Nanoscribe.*

Gaussian laser beam

The setup works with a Gaussian laser beam, meaning that the magnetic and electric field profiles can be described by a Gaussian function. This also means that the intensity of the laser has a Gaussian distribution over the cross-sectional area of the beam. The beam can be described by the radius at the focal plane w_0 , which will be referred to as beam waist radius, and the beam radius $w(z)$ at a distance z from the focal plane. The beam radius is described by Eq. (3-7), where f_L is the Rayleigh length, described by Eq. (3-8). This is the distance from the focal plane where the cross-sectional area of the beam is twice as large as at the beam waist. In the two dimensional example given in Figure 3-10, this can be described as the distance from the focal plane where $w(z) = \sqrt{2}w_0$.

$$w(z) = w_0 \sqrt{1 + \left(\frac{z}{f_L}\right)^2}, \quad (3-7)$$

$$f_L = \frac{(n\pi w_0^2)}{\lambda}. \quad (3-8)$$

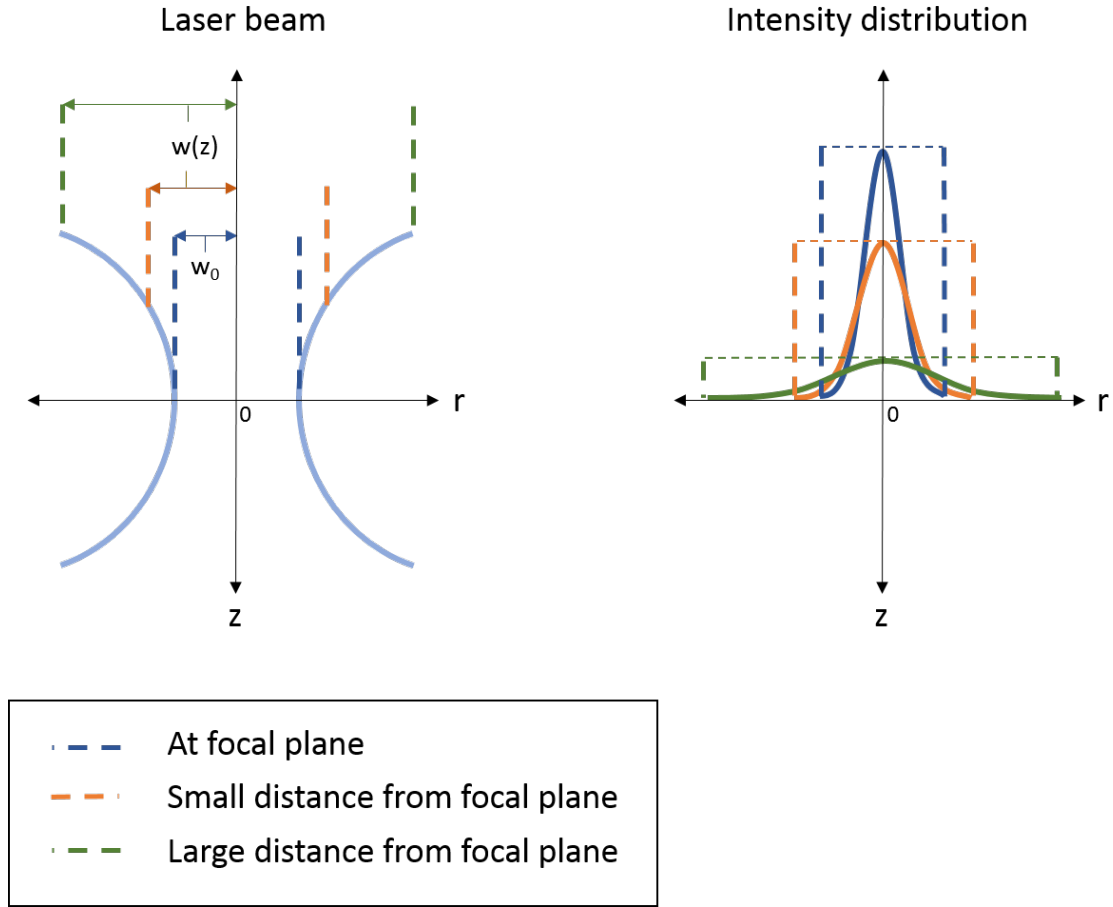


Figure 3-10: The profile of a Gaussian beam with the intensity distribution at different distances from the focal plane.

The intensity of the laser beam has a Gaussian distribution over the r -axis, and can be written as Eq. (3-9). The highest intensity, or the peak intensity, can be found at $r = 0$ and can be described as in Eq. (3-10) [51].

$$I(r, z) = I_0 \left(\frac{w_0}{w(z)} \right)^2 \exp\left(\frac{-2r^2}{w(z)^2} \right), \quad (3-9)$$

$$I_0 = \frac{2\eta P_{laser}}{\pi w_0^2}. \quad (3-10)$$

In this equation η is the transmittance of the objective lens and P_{laser} is the laser power. Substituting these equations in the governing equations of the TPL process on a positive photoresist gives the main equation that was used in this research, given in Chapter 4.

Chapter 4

Characterization

In this chapter the main results for the characterization phase of the research are given and the most important decisions that were made are explained. The results are discussed and recommendations for further experiments are given. This phase of the research was meant to understand and characterize the process of TPL on a positive photoresist, especially for the manufacturing of pores. For the experiments, a layer of 10 μm thick AZ 4562 was spincoated on a 170 μm thick glass slide (Menzel-Gläser, Bad Wildungen, Germany). The full protocol is given in Appendix C.

4-1 The main equation

The chemical reaction and governing equations of a positive photoresist that is exposed to a NIR laser were explained in Chapter 3. From relation 3-3, the main equation that was used to model the voxel diameter and height was derived by substituting the optical and material properties. The derivation of the equation is given in Appendix A. The resulting equation is shown in Eq. (4-1). In this equation the TPA constant C is described by Eq. (4-2). The value and meaning of each variable that was used is given in Table 4-1.

$$d(z) = w(z) \sqrt{\ln\left(\frac{4C\eta^2 P_{laser}^2 t}{f\tau(\pi h\nu w^2(z))^2 \ln\frac{M_0}{M_{th}}}\right)} \quad (4-1)$$

$$C = \frac{\Phi\delta C_0}{A_E + C_0} \quad (4-2)$$

Unknown variables

In Eq. (4-1) there are four unknown variables to take into consideration. Firstly, the TPA constant C , which consists of material properties that are not known for the photoresist AZ 4562. The second unknown variable is the exposure time t . Since the research is done for pore manufacturing we are working with a scanning laser, which makes it more difficult to accurately determine the exposure time for a specific point in the resist. The third unknown variable is the material threshold value for dissolvable amount of DNQ, M_{th} . In literature there was no research found that describes this property of AZ 4562 and Microchemicals also does not know or provide this information. The final unknown variable is the exact value for the beam waist radius w_0 .

From these variables, C , t and M_{th} are of similar mathematical influence. Therefore, to simplify the problem, these variables were taken together into a single new variable K_{CtM} given in Eq. (4-3).

$$K_{CtM} = \frac{Ct}{\ln\left(\frac{M_0}{M_{th}}\right)} \quad (4-3)$$

The beam waist radius w_0 is of different mathematical influence, because it can be found both in- and outside the square root in the equation. Therefore this variable is kept separate from the other unknown variables. The calculations that support this decision are given in Appendix A. In literature, different ways of describing w_0 were found. The actual value can be different for any setup due to lens aberrations or the use of a material with a different refractive index. A general expression of w_0 can be given by Eq. (4-4a). However, for a TPL system with a large numerical aperture (i.e. larger than 1), there are more accurate ways to describe the beam waist radius [51]. Cao et al. used Eq. (4-4b) to describe the beam waist radius and in a two-photon polymerization (2PP) research by Zhou et al. Eq. (4-4c) was used [51]. This third equation for w_0 was also used in earlier research on 2PP done at the department of Precision and Microsystems Engineering (PME). In the equations λ is the wavelength of the laser, N_A is the numerical aperture of the objective lens and n is the refractive index of the photoresist. For the calculations in this research, the refractive index of similar photoresist AZ 4620P was used [41, 55]. Because Eq. 4-4c gave good results for the previous research at PME, the beam waist radius is expected to be close to this value. This is elaborated more in the discussion section of this chapter.

$$w_0 = \frac{\lambda}{\pi N_A} = 177.34nm, \quad (4-4a)$$

$$w_0 = 0.41 \frac{\lambda}{N_A} = 228.43nm, \quad (4-4b)$$

$$w_0 = \frac{\lambda}{\pi N_A} \sqrt{n^2 - N_A^2} = 149.77nm. \quad (4-4c)$$

Table 4-1: The variables used to calculate the voxel diameter and height. The unknown variables were given an estimated value.

Known variables			
Sign	Value	Unit	Explanation
η	0.13	[-]	Transmittance [41]
P_{laser}	0 - 50 x 10 ⁻³	[W]	Laser Power, varied
f	80 x 10 ⁶	[s ⁻¹]	Repetition frequency
τ	100 x 10 ⁻¹⁵	[s]	Pulse width
h	6.626 x 10 ⁻³⁴	[J · s]	Planck's constant
λ	780 x 10 ⁻⁹	[m]	Laser wavelength
c	300 x 10 ⁶	[m · s ⁻¹]	Speed of light
ν	3.8462 x 10 ¹⁴	[s ⁻¹]	Light frequency
M_0	1	[-]	Initial amount of DNQ
N_A	1.4	[-]	Numerical aperture of the lens
z	0	[m]	Distance from focus point
f_L	66 - 412 x 10 ⁻⁹	[m]	Rayleigh length
n_{az}	1.635	[-]	Refractive index resist
Unknown variables			
Sign	Value	Unit	Explanation
t	10 x 10 ⁻³	[s]	Exposure time
M_{th}	> 0 and < 1	[-]	Threshold value of dissolvable DNQ
Φ	> 0 and < 1	[-]	Quantum efficiency
δ	1 x 10 ⁻⁵⁸	[m ⁴ · s]	Two-photon absorption cross section [57]
C_0	> 0 and < 1	[s ⁻¹]	A material constant
A_E	1 x 10 ⁻⁴	[s ⁻¹]	Coefficient of spontaneous emission [58]
w_0	100 - 250 x 10 ⁻⁹	[m]	Beam waist radius

4-2 Experimental results

The first experiments that were done were meant to find the resolution limit of the process and to create pores with a diameter as small as possible. To create the pores, the focal point of the laser was scanned through the resist in vertical direction. To find the pore diameter corresponding to certain laser powers and scanning speeds, parameter sweeps were done. For the result displayed in this chapter, the laser power was varied between 0.5 and 5 mW and scanning speeds between 10 - 100 $\mu m/s$ were used. The average of three individual measurements was taken. The specific case reviewed in this chapter is a process with a scanning speed of 40 $\mu m/s$. The results for the other scanning speeds are given in Appendix B. For the comparison between the modeled and measured voxel height and diameter, a laser power of 3.5 mW was used.

The smallest pores created were between 250 - 290 nm , shown in Figure 4-1. The average size of these nine pores was 273.33 nm with a standard deviation of 14.14 nm . The used settings were a laser power of 0.5 mW and a scanning speed of 30 $\mu m/s$. For these settings however, pores were not observed in every sample. Pores with these dimensions were not reproducible. The possible explanation for this observation is discussed at the end of the chapter.

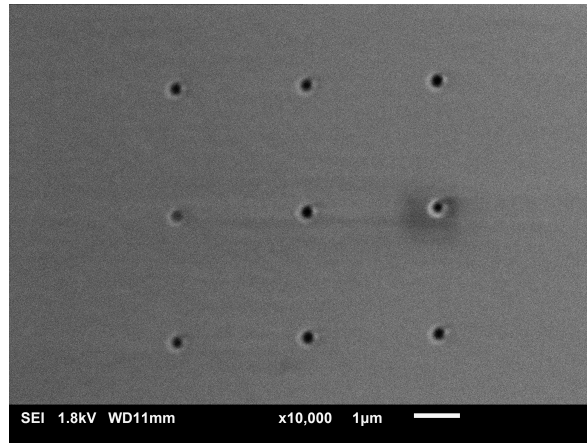


Figure 4-1: Pores with a diameter between 250 - 290 nm .

Voxel shape assumption

In literature [52,59–61], mainly on 2PP, the voxel shape is usually assumed to have the shape of an ellipsoid. This voxel shape is also used in the software Describe (Nanoscribe GmbH), that gives a preview of the written code. Following this assumption, the diameter of the voxel should be the largest at the focal plane of the laser, which can also be described as $z = 0$. This means that for the calculations of the pore diameter, at first $z = 0$ was used in the main equation. A graphical user interface (GUI) was made with MATLAB, performing a least squares error fit of the main equation on the measured diameters for fitting variables K_{CTM} and w_0 . The acquired data and the model fit is shown in Figure 4-2a.

From the fit, the following values are obtained: $K_{CTM} = 1.70 \times 10^{-59} m^4 s^2$ and $w_0 = 623.78 nm$. The value for K_{CTM} could be realistic, but the obtained beam waist radius is

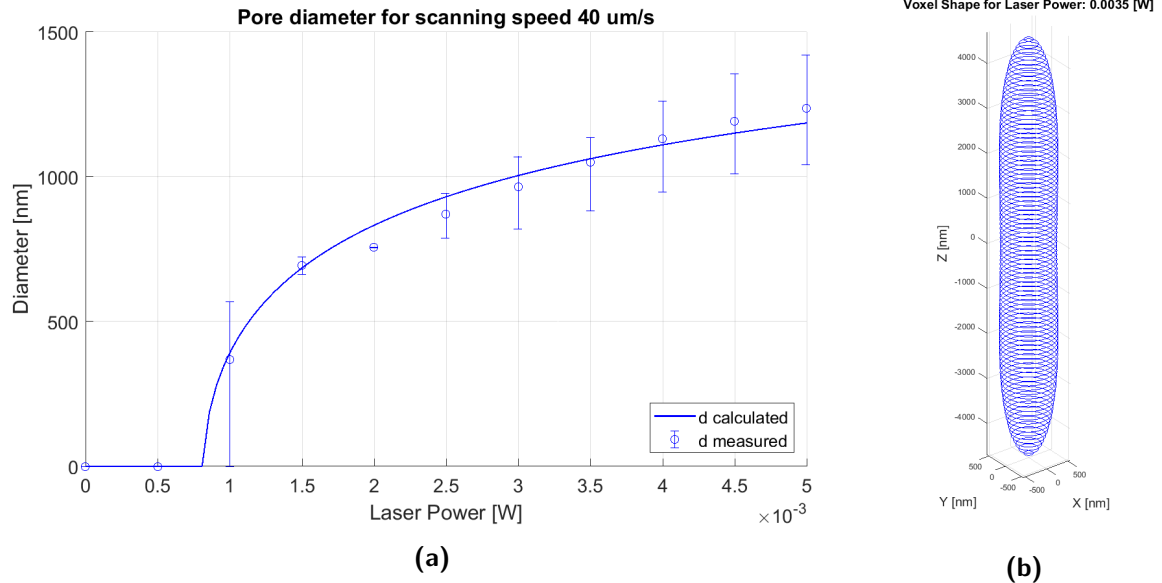


Figure 4-2: (a) The least squares error fit for the given dataset. (b) The 3D model of the voxel at a laser power of 3.5 mW.

very large compared to the ones that were used in earlier research (Eq. (4-4b) and (4-4c)). Since the diameter of the voxel depends on the distance z from the focus point, Eq. (4-1) can be used to find the largest value for z where d is still larger than 0. If we calculate the diameter for different distances from the focus point, a 3D model of the voxel can be generated. The result for the current values of K_{CtM} and w_0 is given in Figure 4-2b. The total voxel height corresponding to the voxel diameter is $9.4 \mu\text{m}$. The large voxel height obtained from the model was the reason to do further experiments to test if the voxel is indeed this high. Besides the height, it can be observed that the diameter is slightly larger at $z = 1.9 \mu\text{m}$, than at $z = 0$. This could mean that the maximum voxel diameter, which is needed to predict the pore diameter, is not at the focal plane but at different height z . This is also a reason for the following experiments.

Measuring the voxel height

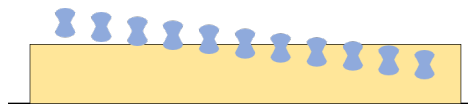


Figure 4-3: The voxel is lowered into the resist with steps of 50 nm.

The experiment that was done to measure the voxel height is visualized in Figure 4-3. The voxel was lowered into the resist with steps of 50 nm, starting with the entire voxel above the surface of the resist. From this experiment the voxel height and the voxel diameter at different distances from the focal plane were measured. The data that is extensively analyzed in this section is again found for a laser power of 0.5 - 5 mW and a scanning speed of $40 \mu\text{m}/\text{s}$. The laser power used for the analysis of the voxel shape is 3.5 mW. To find new values

for K_{CtM} and w_0 a new GUI was made, performing a combined least squares error fit of the main equation on the measured voxel diameter and height. The result is shown in Figure 4-4a. The blue dots represent the average measured voxel diameter and the red dots the corresponding voxel height of three independent measurements. The error bars indicate the minimum and maximum measured value, including measurement errors, which are explained in the discussion section. The blue and red lines are the fitted curves for the voxel diameter and height respectively. For a scanning speed of $40 \mu\text{m}/\text{s}$, this resulted in fitting values: $K_{CtM} = 2.75 \times 10^{-60}$ and $w_0 = 125.14 \text{nm}$. The value for K_{CtM} is still realistic and the value for the beam waist radius is much closer to the value that was used in the earlier research in literature and the research done at PME. The values for K_{CtM} for the different scanning speeds are shown in Figure 4-5a. The graph shows a linear relation between the scanning speed and the value for K_{Ctm} . For all of the scanning speeds the obtained beam waist radius was in a range of $119.45 - 127.13 \text{nm}$, with an average of 123.79nm . The data with fits is given in Appendix B. Figure 4-5b displays the possible combinations of $C * t$ and M_{th} for the found value of K_{CtM} .

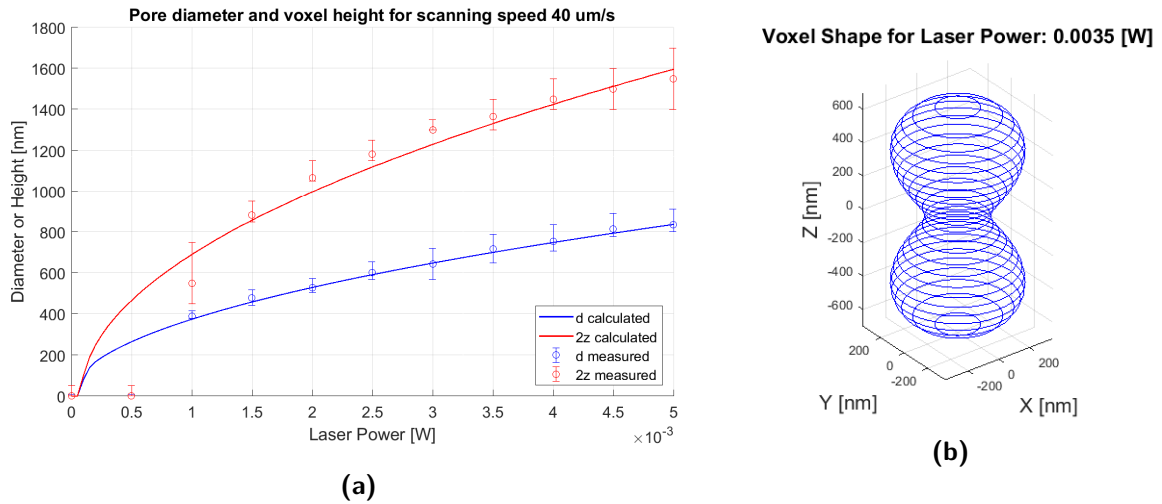


Figure 4-4: (a) Combined least squares error fit for the voxel height (red) and diameter (blue). The total height of the voxel (i.e. $2z$) is shown. (b) 3D visualization of the voxel at laser power 3.5 mW and scanning speed $40 \mu\text{m}/\text{s}$.

For the actual voxel shape the result for a laser power of 3.5 mW was chosen to more extensively discuss. The micrograph made of one of the three experiments for this laser power is shown in Figure 4-6a. The obtained new values from the fitted equation were used to determine the new shape of the voxel. The result is visualized in 3D in Figure 4-4b. An hourglass-like shape is visible, which is narrow near the focal plane and grows larger as the distance z increases. Finally the diameter of the voxel quickly decreases to 0. In Figure 4-6b, the measured data points are plotted over the modeled cross-section of the voxel. The measured voxel is slightly higher than the calculated result and the waist is not as narrow. The maximum voxel diameter is found for a slightly larger distance from the focal plane than calculated. Possible reasons for these differences can be found in the discussion.

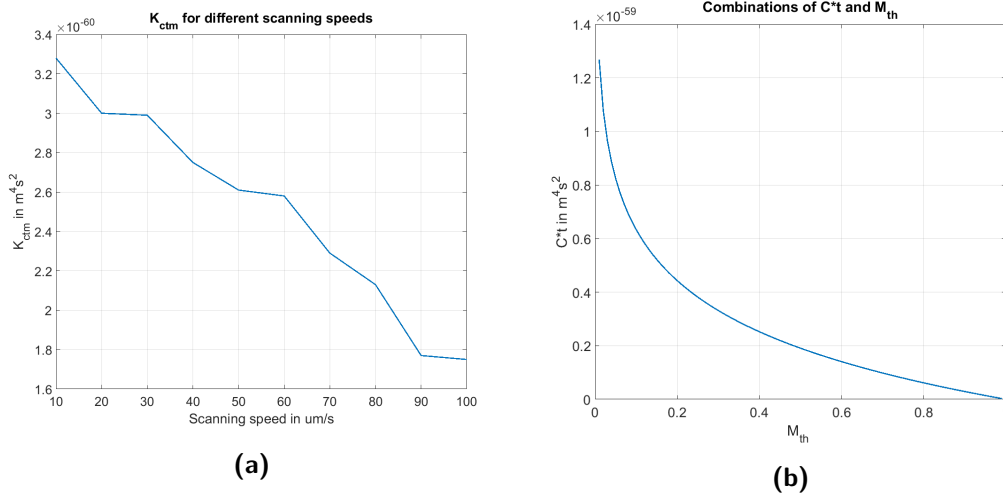


Figure 4-5: (a) The obtained values for K_{CtM} decrease linearly with an increasing scanning speed. (b) The possible combinations of Ct and M_{th} for the obtained value of K_{CtM} .

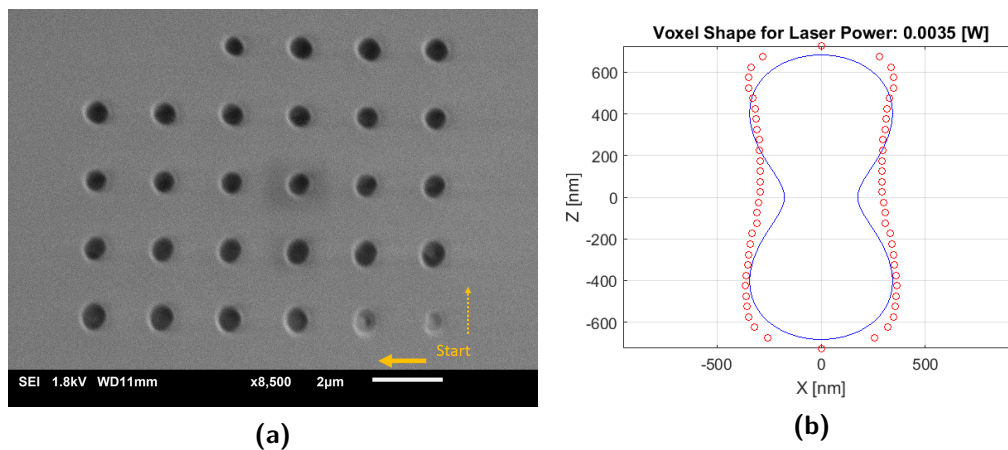


Figure 4-6: (a) Voxel diameter and height test by lowering the voxel with steps of 50 nm, from right to left, starting in the lower right corner and then upwards. The scanning speed was 40 μm/s and the laser power was 3.5 mW. (b) The measured voxel diameter at different heights in red and the cross-section of the calculated voxel shape in blue.

In Figure 4-7, the predicted voxel shape is shown for different laser powers. As the laser power gets lower, the voxel will start to look more like the ellipsoid again. With the obtained fitting values for a scanning speed of $40 \mu\text{m}/\text{s}$, the first laser power at which the maximum voxel diameter occurs at $z = 0$ again can be calculated. This happens for a laser power of 0.2235 mW , where the voxel has a cigar-like shape. If the laser power further decreases, the voxel will have a fully ellipsoidal shape again.

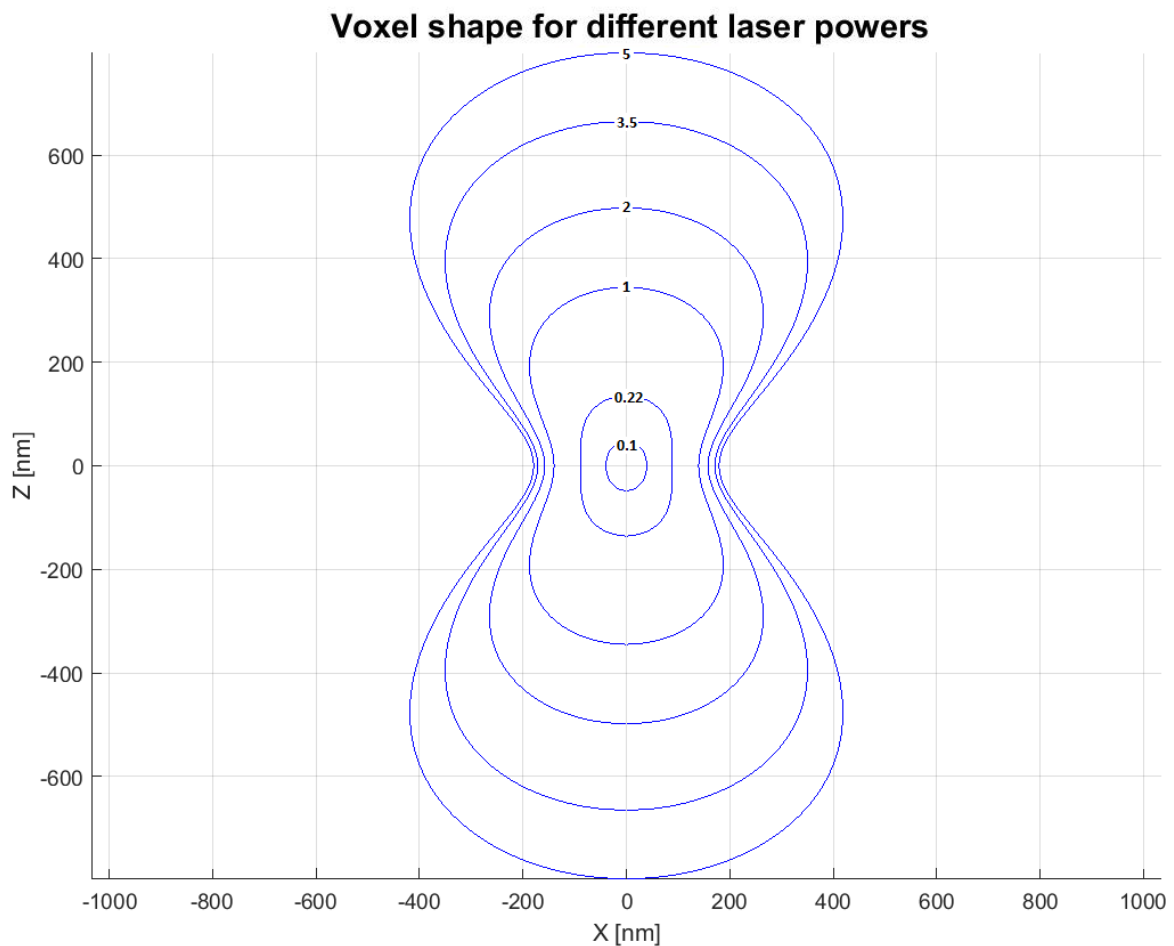


Figure 4-7: The predicted voxel shape for different laser powers (mW).

4-3 Conclusions and discussion

In this section the most important observations that were found in the characterization phase of the research are listed. Possible explanations for the observations are given and suggestions are made for additional experiments.

Important observations

- The assumption that the voxel has an ellipsoidal shape is not true for every laser power. The model showed that the voxel follows the profile of the Gaussian beam and takes an hourglass shape for higher laser powers. The experiments confirmed this observation and showed that the maximum voxel diameter is not always found at the focal plane. For the modeling of the voxel dimensions, therefore the maximum voxel diameter rather than the diameter at $z = 0$ has to be taken into account. There were small differences between the dimensions of the measured voxel and the modeled voxel. The diameter of the measured voxel was larger at the beam waist and slightly higher. Possible explanations for this difference are discussed in 4-3.1, 4-3.2 and 4-3.6.
- The minimum pore size was found to be around 250 nm. For the very low laser powers at which these pores were produced, pores were not always observed. In some cases TPA was not initiated. Possible reasons for this irregularity and explanations why the minimum pore size is limited are given in 4-3.1, 4-3.2, 4-3.3 and 4-3.4.
- The beam waist radius that was obtained from the model was larger than the value calculated with the equation given by Zhou et al [51], which gave good results for earlier research at PME. An explanation for the larger beam waist radius is discussed in 4-3.4.
- A difference in pore diameter can be observed between the situation where the voxel was scanned through the resist and when the voxel was used for single voxel exposure. The reason for this difference is discussed in 4-3.5.
- During the process there were measurement errors that could have had a small influence on the final result. The possible errors in the process are mentioned in 4-3.6.

4-3.1 Aberrations in the optical system

The optical system in the setup will never be perfect. Small aberrations in the system could be one of the reasons why the measured voxel diameter at the waist was larger than modeled. Due to spherical aberrations in the lens, parts of the laser beam may be focused at a small distance from the desired focal point. This would create a larger beam waist radius, resulting in a larger region where TPA is initiated. This could also be one of the factors that limits the minimum voxel diameter.

4-3.2 Diffusion of the functionalized DNQ

Diffusion of the DNQ that was functionalized with a COOH-group into the unexposed resist can be one of the factors that limits the minimum pore diameter, as well as it can be an explanation for the differences between the measured and calculated voxel shapes. If the functionalized DNQ would diffuse into the unexposed resist, the effect would be larger at the waist of the voxel, because the DNQ can diffuse from more directions. This is visualized in Figure 4-8.

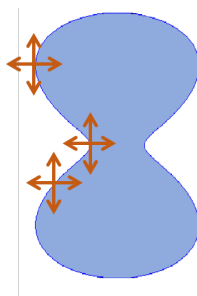


Figure 4-8: Voxel with arrows indicating diffusion of functionalized DNQ at three different locations. The effect will be larger at the waist of the voxel.

To see if the diffusion of the excited molecules into the unexposed resist is the cause of the actual voxel shape, there are different experiments that can be done. An option is to do the same experiment for a very thin layer of resist. If the layer is thin enough, the excited molecule can only diffuse in the horizontal plane, which will decrease diffusion. Another option is to do the experiment for the voxel height at different temperatures. At low temperature there should be less diffusion than at higher temperatures.

4-3.3 Effects at low laser powers

The experiments were performed with very low laser powers. At such low laser powers, quantum effects can come into play. Due to the particle nature of light, the presence of photons will always be in discrete numbers. For a very low photon density, the situation may occur that sometimes one photon and sometimes two photons are present within the timespan needed for TPA. This would result in a procedure where sometimes TPA is initiated and other times nothing happens. These fluctuations in the laser intensity are also called shot noise [62, 63].

4-3.4 Refractive index of the photoresist

The refractive index of the photoresist could be a factor that limits the minimum diameter of the voxel, as well as it can be the reason that the obtained beam waist radius was larger than expected from literature. Taking the equation from Zhou et al, the beam waist depends on the refractive index of the photoresist [51]. If this equation is reliable, a lower refractive index would result in a smaller beam waist radius. This could make it possible to produce smaller pores. The refractive index of AZ 4562 used in this research was estimated based on

the research of Cao et al. who used a similar photoresist (AZ 4620P) [41, 55]. If the actual refractive index of AZ 4562 is smaller than estimated, this would result in a smaller calculated beam waist radius. The obtained values for the beam waist radius would correspond if the refractive index of the material is in the range of 1.554 - 1.573. The refractive index could be measured with a refractometer to see if the estimation by Zhou et al. is applicable in a TPL process on a positive photoresist.

4-3.5 Scanning speed and exposure time

It can be observed that for similar laser powers and scanning speeds, the pore diameter for the height experiment was smaller than for the first experiment, where the voxel was scanned through the resist. This can be explained by the fact that single voxel exposure instead of a scanning voxel was used for the height experiment. The scanning voxel increases the exposure time of the resist, creating larger pores. When dealing with single voxel exposure, an increase in scanning speed is directly proportional to a decrease in exposure time. This can also be observed in the linear relation between the value of K_{CTM} and the scanning speed in Figure 4-5a. For a scanning voxel, the exposure time is proportional to $\sqrt{\text{Scanningspeed}}$ according to Nanoscribe GmbH [64].

The obtained knowledge can still be used to manufacture the pores in a membrane. Instead of scanning the voxel through the resist, the pores can be created by single voxel exposure at an increasing height. With this procedure, the alignment accuracy of the TPL machine must be taken into account. For the Photonic Professional GT this accuracy is 10 nm [64].

4-3.6 Measurement errors

There could have been measurement errors that influenced the final result. For the measurement of the diameter, there is an error in the SEM which is typically around 10 nm. The layer that was sputtercoated on the sample has a thickness of around 5 nm. In case the wall coverage is very good, the pore diameter could have appeared 10 μm smaller than it really was. The human error during the measurement was neglected, because the SEM software and a custom MATLAB script was used. There is an error in the voxel height measurement. In the model the number of pores was counted and multiplied with 50 nm. The height can be up to 50 nm higher than measured on both sides of the measurement. This height difference is also visible in Figure 4-6b, where the actual height of the top and bottom dot can be anywhere within 50 nm from the previous data point.

3D manufacturing

The goal of the second phase of the project was to prove that 3D manufacturing is a possibility of TPL with a positive photoresist. Because it is difficult to image 3D structures when they are inside of a polymer layer, the decision was made to use nanoimprint lithography (NIL) to obtain the negative of the 3D structures on a Polydimethylsiloxane (PDMS) surface. PDMS was chosen because it is widely used in microfluidic applications [12, 27, 65–67] and because it was available at the department.

The parameters chosen for the TPL process were:

- Resist layer thickness: 10 μm
- Laser power: 10 mW
- Scanning speed: 20 mm/s
- Slicing: 0.3 μm
- Hatching: 0.06 μm

5-1 Straight pillars

In this research phase the AZ 4562 was used as a stamp. A stamp with straight pores is visualized in Figure 5-1a. As shown in Figure 5-1b and 5-1c, the PDMS was then poured onto the stamp and released, leaving the negative of the pattern on the substrate. The full recipe for PDMS that was used is given in Appendix C.

To support research in the Department of Chemical Engineering, the first stamp that was made was designed for straight pillars. This means that the stamp consisted of pores with straight walls. Arrays of 500 x 500 μm were written for pore diameters of 1, 2, 3 and 5 μm .

The results after the stamping are shown in Figure 5-1d, 5-1e, 5-1f and 5-1g respectively. The images are taken under a 45° angle. The height of the pillars is $7\ \mu\text{m}$. After the first arrays of straight pillars were successfully produced, the work was handed over to a new master student from the Department of Chemical Engineering.

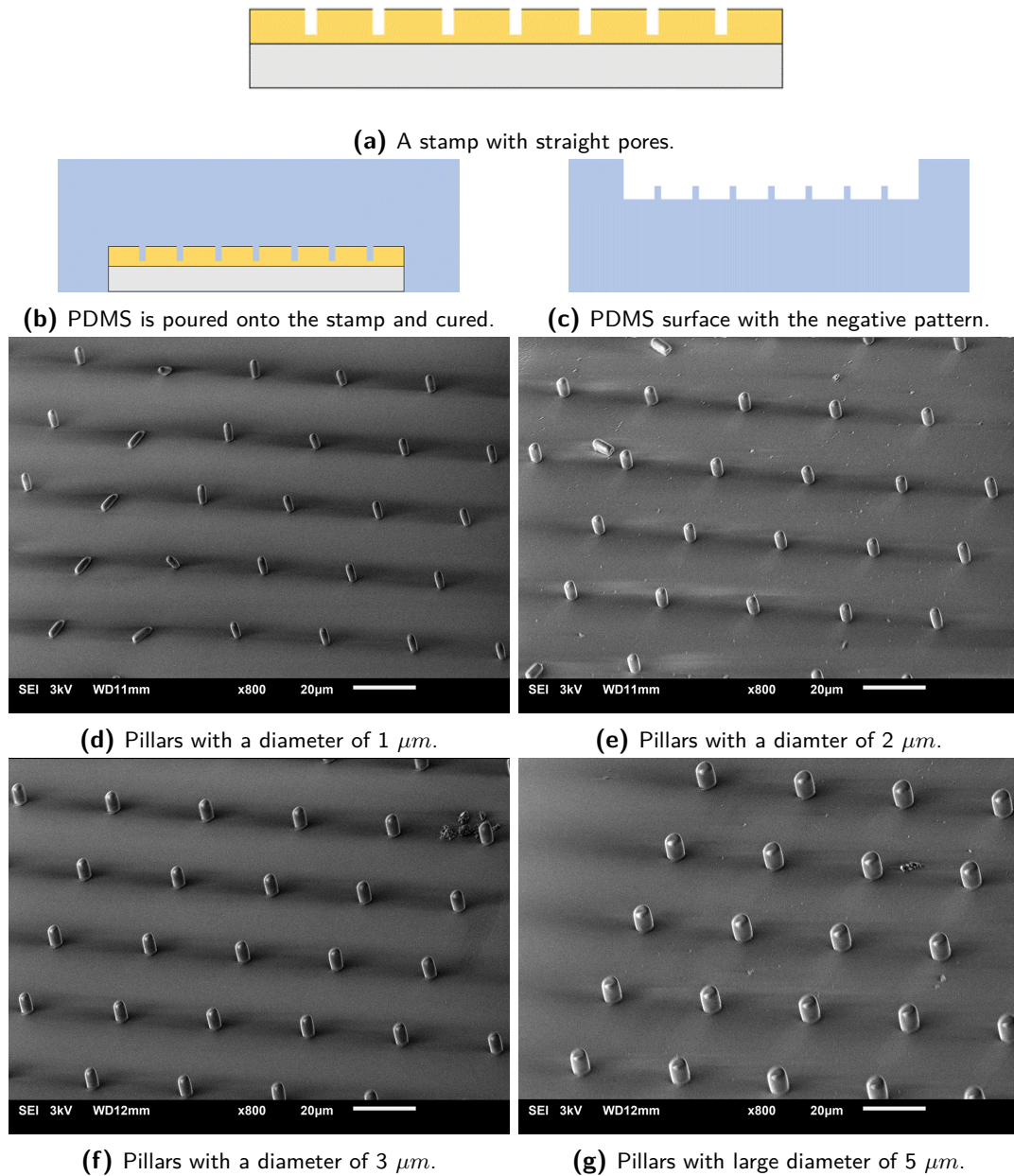


Figure 5-1: The NIL process to create straight pillars.

5-2 3D structures

After the fabrication of the features with straight walls, the next step was to create 3D structures. To prove that it is possible to create pillars with walls that are not straight, a new stamp design was made and imprinted in the PDMS surface. At first a stamp with only pits was made to create an array of cones, shown in Figure 5-2a and 5-2b. The designed array measured $1 \times 2 \mu\text{m}$, but due to the tilt of the sample, only parts of the pits were successfully written and developed. After stamping however, a perfect pattern transfer was observed. Figure 5-2c shows a micrograph of the PDMS surface with the transferred pattern and in Figure 5-2d one of the cones is shown. The pillar has a bottom diameter of $5 \mu\text{m}$, a top diameter of $2.5 \mu\text{m}$ and a height of $7 \mu\text{m}$. The walls are tilted with a slope angle of 80° .

To obtain a variation of structures, a second design featuring three different shapes with varying slope angles was made. Cones with slope angles between 54° and 90° , pyramids with slope angles between 63° and 90° and trapeziums with slope angles between 45° and 90° were successfully produced. Images of the produced structures are given in Appendix B.

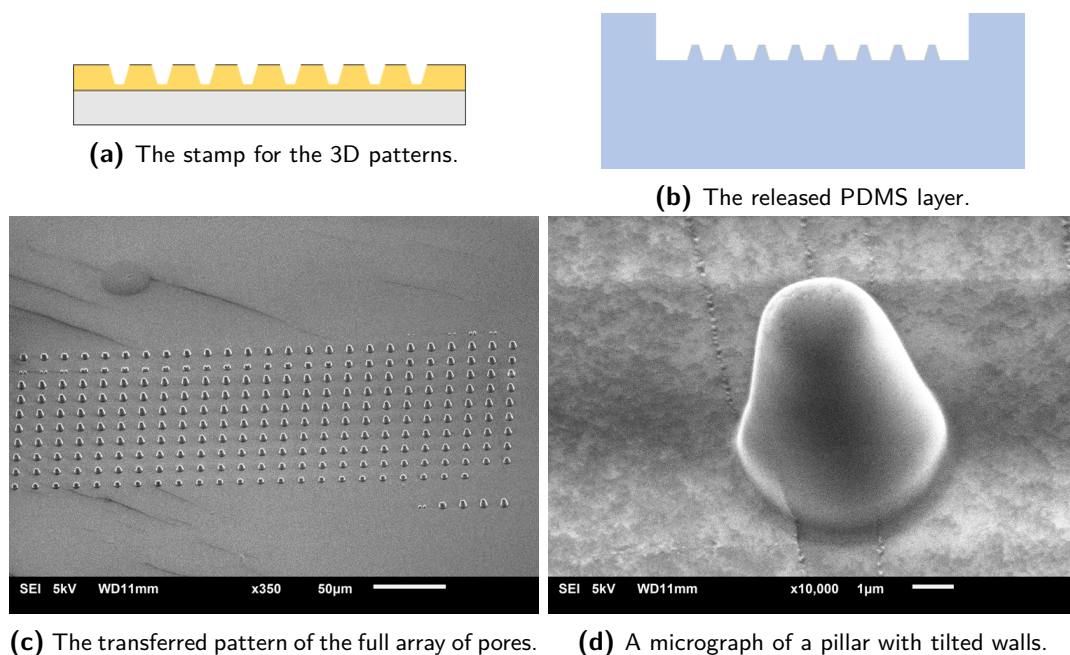


Figure 5-2: The NIL process for 3D structures.

5-3 AZ 4562 as a mold

Finally in the second phase of the research another application for AZ 4562 was explored. Previously the material was used as a stamp for NIL. It can however, also be used as a mold. 3D patterns that grow larger in the horizontal plane when getting deeper into the photoresist were written. The result is a mold, shown in Figure 5-3a. The second step of the process is again pouring the PDMS on the mold as in Figure 5-3b. This time the PDMS can not

simply be pulled off, because the structures would be stuck in the photoresist and get ripped off the PDMS surface. Therefore, after curing the PDMS, the mold was dissolved in acetone, leaving the 3D structures on the surface, visualized in Figure 5-3c and 5-3d. The different structures that were successfully produced were inverse cones with slope angles between 81° and 90° , inverse pyramids with slope angles between 74° and 90° and inverse trapeziums with one straight side and slope angles between 51° and 90° on the other side. Structures with smaller slope angles were pulled off the PDMS surface. An overview of the produced features is shown in Figure 5-3e and a closer view of the inverse pyramids is shown in 5-3f. Images of the other produced structures are given in Appendix B.

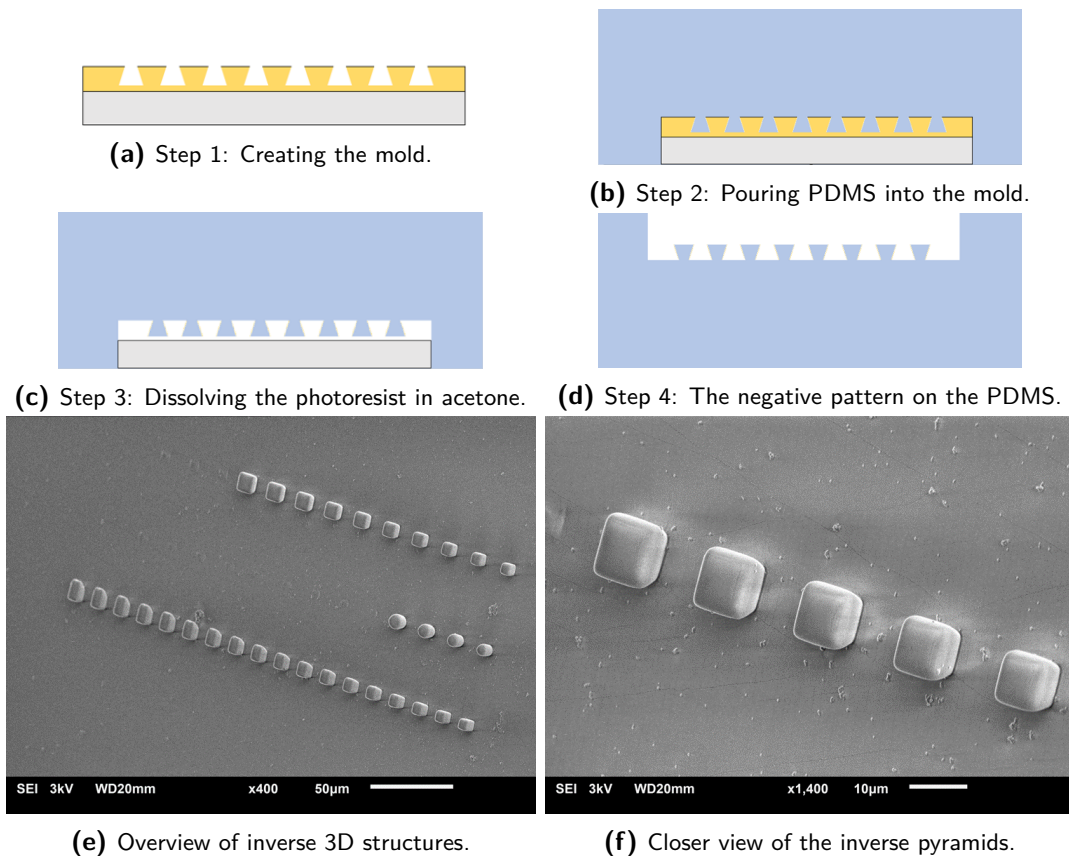


Figure 5-3: The process for producing 3D structures by using a mold.

5-4 Conclusions and discussion

From the experimental results it can be concluded that 3D structures can be created with TPL on a positive-tone photoresist. AZ 4562 makes a good stamp for nano-imprint lithography and a good mold for inverse 3D structures. The material dissolves in acetone. It could however, be beneficial to find a different solution for dissolving the photoresist, because PDMS swells in acetone [68].

The size of the pillars is limited to the size of the pores that can be produced. In Chapter 4 it was shown that pores down to 250 *nm* can be produced. Very small pillars however, could get stuck and pulled of the PDMS surface more easily when the PDMS is removed. For pillar manufacturing thicker layers of AZ 4562 could be used to increase the aspect ratio. However, if the aspect ratio of the pillars is too high, they can be pulled down due to capillary forces during the drying of the sample. This could be solved by drying the sample in a critical point dryer.

The structures produced in the second phase of this research can be described as small topographical features. Currently there are many interesting applications for these 3D or 2.5D surface features. An example is the influence of certain topographical features on the differentiation of mesenchymal and neural stem cells [69, 70]. Using a positive photoresist as a stamp or mold would be a cheap and fast method to create these topographies. Another interesting application of this technique is to create biomimicking surfaces, such as the hydrophobic leaf of the lotus flower [71] or the surface of the inside of a kidney [72], which is a topic of research at PME.

Fabrication of the microfluidic device

In the third phase of the project, fabrication of the microfluidic device was researched. The device consists of two crossed channels at different heights, separated by a membrane. In this chapter the results of the channel and chip manufacturing are given. To create a channel under the surface, the sample was spincoated multiple times with layers of $10\ \mu\text{m}$. For single channels a final layer of $30\ \mu\text{m}$ was used. For the full chip the glass slide was spincoated 5 times resulting in a layer thickness of around $50\ \mu\text{m}$. The protocols for this process can be found in Appendix C and additional results in Appendix B.

6-1 Channel and chip manufacturing

For the manufacturing of the channels, the laser was focused inside the photoresist. The settings that were used for the final channel manufacturing were:

- Laser power: 20%
- Scanning speed: $20000\ \mu\text{m}/\text{s}$
- Slicing: $0.3\ \mu\text{m}$
- Hatching: $0.06\ \mu\text{m}$

After the exposure, the photoresist is developed and it is important that the developer solution can reach the exposed photoresist. For channel manufacturing, the only way the developer has access to the exposed resist is through the in- and outlet holes. To fully develop the channels, four different methods were tried, listed below.

- Developing for a long time without extra measures. The result was the separation of the AZ 400K and water, creating a high concentration of AZ 400K on the bottom of the beaker. This caused the unexposed resist at the bottom of the sample to dissolve and the exposed resist at the top to not dissolve.

- Developing in an ultrasonic bath. The vibrations caused the in- and outlet holes to break.
- Developing in a heated solution for 20 minutes. The developer solution affected the unexposed resist, causing unexposed resist to dissolve as well. The warmer environment could also increase the diffusion of functionalized DNQ into the unexposed resist.
- Developing for a long time with a magnetic stirrer (IKA Labortechnik RH basic). This gave the desired results.

In Figure 6-1a an optical image of three successfully produced channels is shown. The length of the channels is 180, 380 and 580 μm respectively. The channels have a width of 100 μm and a height of 10 μm . There is a contour around the channels, a possible explanation for this observation is discussed later in this chapter. The SEM micrograph in Figure 6-1b shows the surface of the photoresist with the in- and outlet holes. It can be observed that the channels are inside the resist. The channels were developed for 60 minutes, during which the developer solution was stirred. Figure 6-1c displays the smallest channel that was produced. The width of the channel is 10 μm and the length is 420 μm .

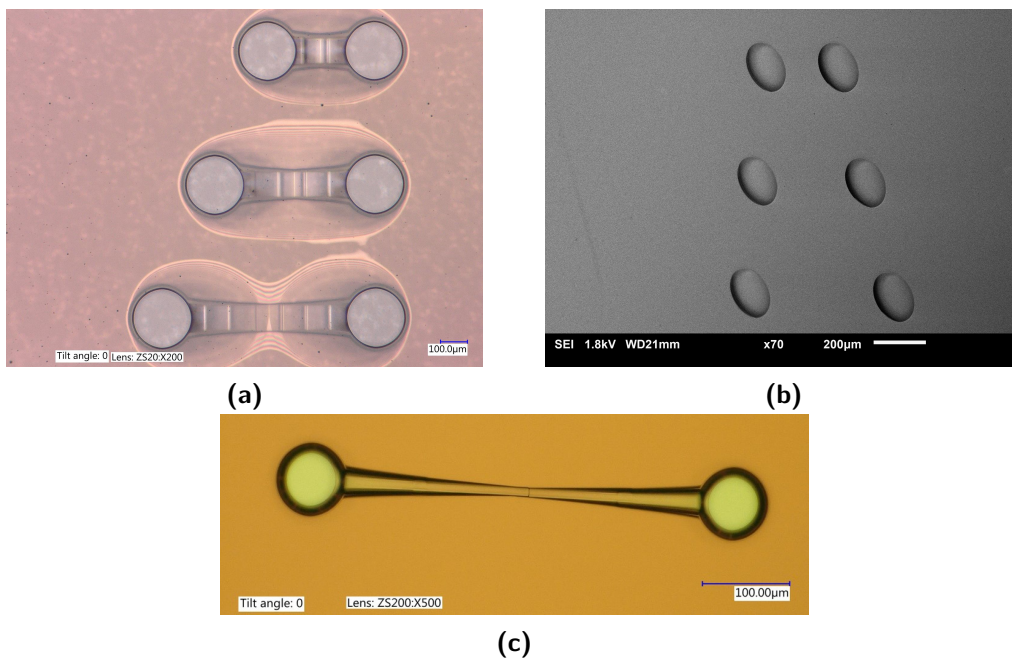


Figure 6-1: (a) Fully developed channel with a width of 100 μm , a height of 10 μm and a length of respectively 180, 380 and 580 μm . (b) SEM image under 45 $^\circ$ angle showing that the channels are closed. (c) Optical image of a small channel that was produced. The height and width are 10 μm and the length is 420 μm .

Finally a microfluidic device consisting of two crossed channels at different heights connected by a membrane was produced. The device was developed, while using the magnetic stirrer, for 80 minutes. An optical image of the device is shown in Figure 6-2a. In Figure 6-2b the image taken with a white light interferometer (Bruker) is shown. It can be seen that the channels are lower than the surface. The depth of the in- and outlet holes is around 50 μm .

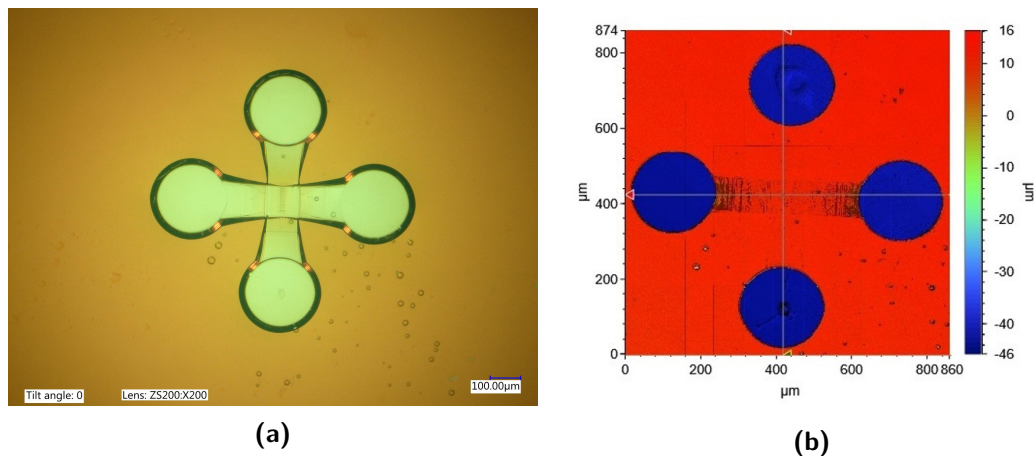


Figure 6-2: (a) An optical image of the fully developed chip. (b) The white light interferometer shows that the channels are under the surface.

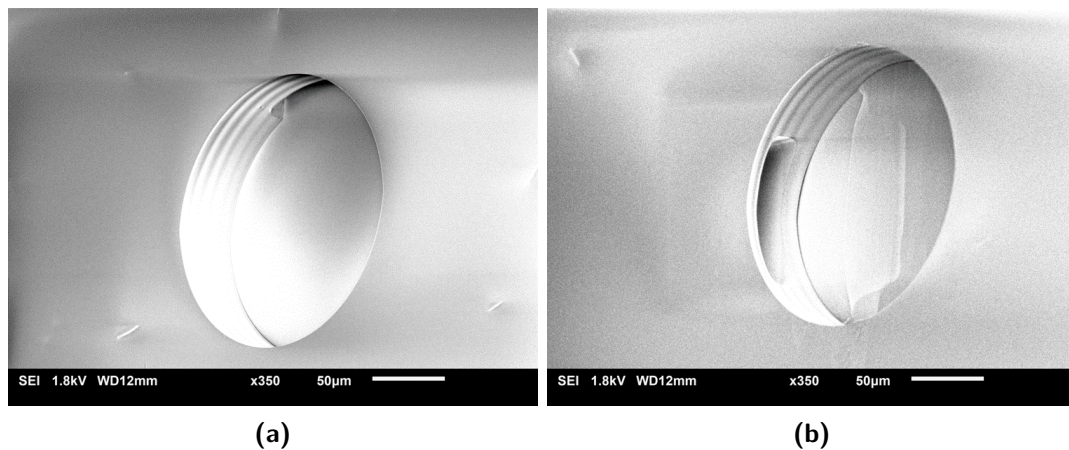


Figure 6-3: (a) Micrograph of the in- or outlet hole to the lower channel taken in the SEM under a 45° angle. (b) Micrograph of the in- or outlet hole to the higher channel.

In Figure 6-3a an in- or outlet hole is shown for the lower channel. The opening of the channel is clearly visible. The diameter is 210 μm, designed for the smallest blunt needle available. Figure 6-3b shows the opening to the higher channel.

6-2 Conclusions and discussion

Two-photon lithography can be used to create a microfluidic device featuring two crossed channels and a connecting membrane in a single lithography and development step. The development time of the device is long and still needs to be optimized. The photoresist AZ 4562 can not withstand the vibrations of an ultrasonic shaker. Heating the developer solution will decrease the development time, but it will increase the effect from the developer on the unexposed resist. The warmer environment may also increase the diffusion of functionalized DNQ into the unexposed resist, resulting in larger channels. If the AZ 400K and the DI-water

are not stirred for a long time, they will separate and there will be a higher concentration of developer on the bottom of the beaker. This will result in an uneven development of the sample. The use of a magnetic stirrer during development is therefore recommended.

It can be observed that the channels are wider at the in- and outlet holes. This is caused by dark erosion [73]. The developer solution also affects the unexposed material. At short development times this is negligible, but for the channel manufacturing the effect is clearly visible. A lower ratio of AZ 400K and DI-water could reduce the dark erosion. However, the development time will then increase. Another solution would be to design channels that are narrower at the in- and outlet interfaces and wider towards the middle of the channels. The opening for the developer to the exposed resist will be smaller, increasing the total development time. The channels however, would be straight in the end. This can only be done when the dark erosion is characterized per unit time.

To explain the contours around the channels, a capillary flow experiment was conducted. A droplet of water was placed on the substrate and capillary forces pulled the water into the channel. The flow could not be filmed, because a microchannel fills within milliseconds by capillary flow [74, 75]. In Figure 6-4a, the dry channels are shown with the contours around them. In Figure 6-4b the channels are filled with water and the contours are not clearly visible anymore. The channels were written at the height of the interface between the glass and the photoresist. During or after the development, the remaining resist next to the channels did not adhere well to the glass anymore and partly released. The space underneath the resist is also filled with water, explaining why the contours disappeared when the channels were filled. After the sample was dried, the contours were visible again. For future channel manufacturing it is therefore recommended to produce the channels at a height from the glass, to make sure that the channels are fully closed.

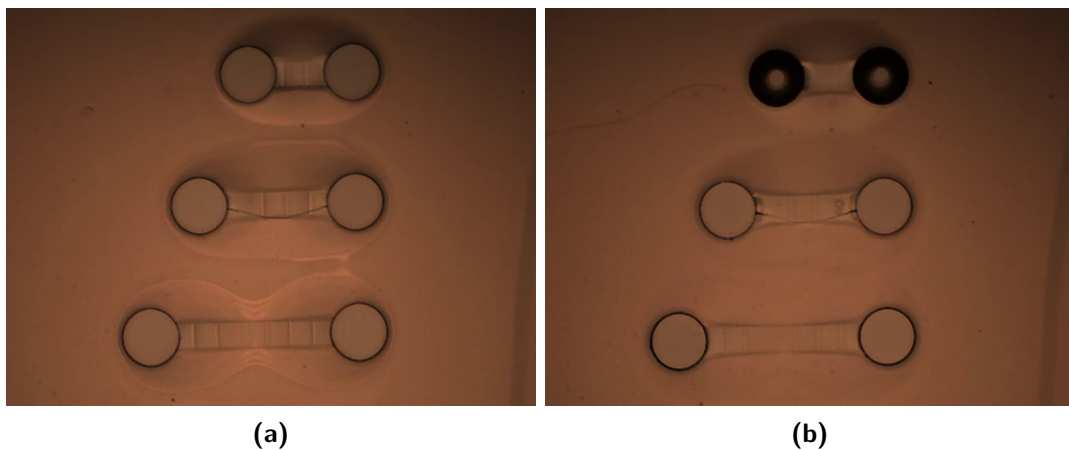


Figure 6-4: (a) Dry channels before they were filled with water. (b) Channels filled with water.

Conclusions and recommendations

The goal of this research was to find and characterize a manufacturing method that can be used for the single step fabrication of a microfluidic device consisting of two crossed channels at a different height level, connected by a membrane. The proposed manufacturing method was two-photon lithography (TPL) on a positive photoresist, as this method is suitable for small scale production, it allows rapid prototyping and offers the possibility of 3D manufacturing. The photoresist used was AZ 4562. The research was divided into three phases. The first phase was the characterization of the process, which was mainly focused on pore manufacturing. In the second phase 3D manufacturing was explored. The third phase focused on using the obtained knowledge for the fabrication of the microfluidic device.

The process of pore manufacturing was characterized by testing and measuring the height and diameter of the voxel. A model was made to describe the voxel dimensions for laser powers between 0.5 and 5 *mW* and the calculations corresponded well to the experimental results. It was observed that the voxel takes an hourglass shape for higher laser powers, meaning that the maximum voxel diameter is not always found at the focal plane of the laser. Therefore, in a procedure to write pores, the maximum voxel diameter instead of the diameter at the focal plane should be taken into account. Pores with a diameter down to 250 *nm* were successfully produced, but were not reproducible. Straight pillars and 3D structures were successfully fabricated by using AZ 4562 as a stamp in a nanoimprint lithography (NIL) process onto a Polydimethylsiloxane (PDMS) surface. The pattern was completely transferred and the stamp was reusable. Furthermore, AZ 4562 was used as a mold for more complex 3D structures in a process where the resist was ultimately dissolved in acetone. Finally a fully developed microfluidic device was successfully fabricated in a single lithography and development step. The thickness of the resist was 50 μm . The channel width was 100 μm and the height was 10 μm . The channels were separated by 10 μm in height. During the development the solution was continuously mixed with a magnetic stirrer.

Based on the results of this project several recommendations for future research can be made. To be able to create reproducible high resolution pores, the use of a photoresist with a lower

density of the photosensitive DNQ is recommended. This will lead to less functionalized DNQ and less material that is dissolved. It will also reduce the diffusion of the functionalized DNQ into the unexposed material. A lower density of DNQ may also allow the use of a higher photon intensity, which would reduce the influence of laser fluctuations. Furthermore it is recommended to use a photoresist with a lower refractive index, which would result in a smaller beam waist radius. To further verify and improve the model that predicts the voxel dimensions, it is recommended to measure the properties of the photoresist before doing any other experiments.

For the manufacturing of the microfluidic device, a new way of coating the resist must be found. If a thicker layer can be deposited in one step, time is saved and there will be no risk of any contamination between the layers. Another recommendation for the manufacturing of microfluidic channels is to find a faster way of developing the chip to prevent dark erosion. An example is to continuously rotate the sample during the development.

Finally it is recommended to try to combine different types of photoresists. The combination of a positive and a negative-tone resist offers many new possibilities for the fabrication of microfluidic devices. For example, a positive resist could be used for channel production, after which the channel could be filled with a negative-tone resist to create topographical features inside the channel.

Chapter 8

Reflection

This chapter contains a self-reflection about the year that I spent on my project. My experiences, planning, project progress and points of improvement will be discussed.

I did my bachelor end project at the PME department in the field of OoC technology. I noticed that I like this field of research as it deals with real world problems, such as the one researched during this project. For this reason I joined the masters track PME, where the group of Micro and Nano Engineering (MNE) caught my interest. I really like the fact that MNE firstly focuses on the fundamental understanding of a process and then uses the knowledge to solve relevant problems. MNE is an impressive group with people that are truly experts in their field of work. It was a privilege to be a part of this group and to be able to make use of the knowledge and facilities it offers.

In the introduction of this report, a project planning can be found in the form of a Gantt chart. Making the planning taught me to make realistic estimations of the amount of work needed to solve a problem. I incorporated two weeks of vacation and three backup weeks in the planning. In the end it turned out that both the vacation and the backup weeks were very welcome. I learned that it is good to also relax in between long periods of work and that the writing of a full thesis will take longer than one would think. During the project, the different phases overlapped a bit. The first phase was stretched out, whereas the second project phase started earlier. Despite the overlap between the different phases, the planning was realistic and successfully executed.

During the project I learned that modeling and experimental work is a good combination. To switch work environments now and then keeps you sharp and motivated. It is very satisfying if the lab work confirms predictions made with a model. If however, the measurements do not correspond with the model, this can be frustrating. Doing the experiments in the lab was also difficult at times. Dirty beakers and substrates, tilted samples and broken glass slides are inevitable when working in the lab for a year. This taught me to be patient and careful and to

stay focused at all times during experiments. When I had dirty samples, I learned to analyze the process step-by-step to find the cause of the problem, which turned out to be dirty beakers.

During the project there were certain things that I could have done better. I spent a lot of time on trying to create smaller pores, even though they were already smaller than $1 \mu m$. I could have spent this time on the second and third phase of the research and maybe have time left at the end of the project for extra experiments with the full chip. Another point of improvement is that I can ask for feedback sooner. The hourglass shape of the voxel that came out of the model was unexpected and I waited a long time before asking anyone to take a look at it. Finally it would have been good to measure the material properties of my photoresist. This would have made my model more accurate.

In the end I am happy with the way the project went. The topic was relevant, the planning was realistic and the results are interesting and can be a valuable contribution to the field of micro and nano manufacturing.

Appendix A

Additional mathematical information

In the first part of this appendix the derivation of the used equation is given. Some equations will be repeated from the main matter of the thesis for convenience of the reader. The second part of the appendix shows the calculations that support the decisions made in the characterization phase of the research, which was discussed in Chapter 4.

A-1 Equation derivation and explanation

The main equation that describes a TPL process on a positive photoresist is given in Eq. (A-1). The photosensitive molecules in the photoresist used in this research are diazonaphthoquinones (DNQ).



From this equation three rate equations can be derived. Eq. (A-2) shows the change in the amount of unexcited DNQ. In Eq. (A-3) the change in amount of excited DNQ is described. The rate at which the excited DNQ reacts with water to form a carboxylic acid (COOH) is described by Eq. (A-4).

$$\frac{dM}{dt} = k_2 M^* - k_1 M, \quad (\text{A-2})$$

$$\frac{dM^*}{dt} = k_1 M - (k_2 + k_3) M^*, \quad (\text{A-3})$$

$$\frac{dP}{dt} = k_3 M^*. \quad (\text{A-4})$$

The total process will quickly reach an equilibrium, meaning that the amount of DNQ in the excited state does not change anymore [56]. With this assumption Eq. (A-3) can be rewritten

as in Eq. (A-5). Filling this in in Eq. (A-2) we obtain a relation for the process in the form of a first order differential equation, shown in Eq. (A-6).

$$M^* = \frac{k_1}{k_2 + k_3}, \quad (\text{A-5})$$

$$\frac{dM}{dt} = \frac{-k_1 k_3}{k_2 + k_3} M. \quad (\text{A-6})$$

Rewriting the equation as Eq. (A-7a) leads to the solution given in Eq. (A-7b).

$$\frac{dM}{dt} \frac{1}{M} = \frac{-k_1 k_3}{k_2 + k_3}, \quad (\text{A-7a})$$

$$M = M_0 \exp\left(\frac{-k_1 k_3}{k_2 + k_3} t_I\right). \quad (\text{A-7b})$$

The rate constants can be described by the following relations, taken from Cao et al. [41]:

$$k_1 = \Phi \delta \left(\frac{I}{h\nu f\tau}\right)^2, \quad (\text{A-8a})$$

$$k_2 = A_E, \quad (\text{A-8b})$$

$$k_3 = C_0, \quad (\text{A-8c})$$

$$t_I = t f \tau. \quad (\text{A-8d})$$

The new variables introduced in these expressions can be combined to a two-photon absorption constant C :

$$C = \frac{\Phi \delta C_0}{A_E + C_0}. \quad (\text{A-9})$$

When substituting the expressions for k_1 , k_2 and k_3 , this results in Eq.(A-10a). Rewriting this with the constant C simplifies the equation to Eq. (A-10b).

$$M = M_0 \exp\left(\frac{-C_0 \Phi \delta \left(\frac{I}{h\nu f\tau}\right)^2 t f \tau}{A_E + C_0}\right), \quad (\text{A-10a})$$

$$M = M_0 \exp\left(\frac{-C t}{f\tau (h\nu)^2} I^2\right). \quad (\text{A-10b})$$

The equation for beam intensity is known to be as in Eq. (A-11), where the peak intensity can be described as (A-12).

$$I(r, z) = I_0 \left(\frac{w_0}{w(z)}\right)^2 \exp\left(\frac{-2r^2}{w(z)^2}\right), \quad (\text{A-11})$$

$$I_0 = \frac{2\eta P_{laser}}{\pi w_0^2}. \quad (\text{A-12})$$

For the calculation of the beam radius, the following equation is used:

$$w(z) = w_0 \sqrt{1 + \left(\frac{z}{f_L}\right)^2}, \quad (\text{A-13})$$

The Rayleigh length is described by:

$$f_L = \frac{(n\pi w_0^2)}{\lambda}. \quad (\text{A-14})$$

For the explanation of the equation we will not fill in w_0 , instead we will keep $w(z)$ in the equation. Filling this in gives:

$$I^2 = \left(\frac{2\eta P_{laser}}{\pi w^2(z)}\right)^2 \exp\left(\frac{-4r^2}{w^2(z)}\right) \quad (\text{A-15})$$

The next step is then to substitute the intensity in the main equation:

$$\frac{M}{M_0} = \exp\left(\frac{-Ct}{f\tau(h\nu)^2} \left(\frac{2\eta P_{laser}}{\pi w^2(z)}\right)^2 \exp\left(\frac{-4r^2}{w^2(z)}\right)\right) \quad (\text{A-16a})$$

$$\ln\left(\frac{M}{M_0}\right) = \frac{-Ct}{f\tau(h\nu)^2} \left(\frac{2\eta P_{laser}}{\pi w^2(z)}\right)^2 \exp\left(\frac{-4r^2}{w^2(z)}\right) \quad (\text{A-16b})$$

Switching the numerator and denominator on the left side will make the right side of the equation positive:

$$\ln\left(\frac{M_0}{M}\right) = \frac{Ct}{f\tau(h\nu)^2} \left(\frac{2\eta P_{laser}}{\pi w^2(z)}\right)^2 \exp\left(\frac{-4r^2}{w^2(z)}\right) \quad (\text{A-16c})$$

The next step is getting rid of the other exponent:

$$\frac{-4r^2}{w^2(z)} = \ln\left(\frac{f\tau(\pi h\nu w^2(z))^2 \ln\frac{M_0}{M_{th}}}{4C\eta^2 P_{laser}^2 t}\right) \quad (\text{A-16d})$$

Switching the numerator and denominator again and taking $w^2(z)$ to the right side of the equation:

$$4r^2 = w^2(z) \ln\left(\frac{4C\eta^2 P_{laser}^2 t}{f\tau(\pi h\nu w^2(z))^2 \ln\frac{M_0}{M_{th}}}\right) \quad (\text{A-16e})$$

Knowing that $2r = d$, finally this will result in the equation used by Cao et al.:

$$d(z) = w(z) \sqrt{\ln\left(\frac{4C\eta^2 P_{laser}^2 t}{f\tau(\pi h\nu w^2(z))^2 \ln\frac{M_0}{M_{th}}}\right)} \quad (\text{A-17})$$

Dimensional analysis

A dimensional analysis has been done to check if the dimension of the equation matches the desired dimension. In Eq. (A-18), the units of the parameters are given.

$$[m] = [m] \sqrt{\ln\left(\frac{[m^4 s][J^2 s^{-2}][s]}{[s^{-1}][s][J^2 s^2][m^4][s^{-2}]}\right)} \quad (\text{A-18})$$

When the units for time are put together the result is shown in Eq. (A-19) showing that the equation ends in the right dimension.

$$[m] = [m] \sqrt{\ln\left(\frac{[m^4][J^2]}{[J^2][m^4]}\right)} = [m] \quad (\text{A-19})$$

From this equation the variables can be split into two groups. The variables that are known and the unknown group. The variables are shown in Table 4-1.

A-2 Characterization steps and decisions

As mentioned there are four main unknown values. The first step in the model was to investigate the individual influence of these variables on the calculated result. Before this is done, there is already one simplification that can be made. Since constant C and exposure time t have exactly the same mathematical influence, these variables can be taken together to form one new variable Ct . The third and fourth unknown variables are the material threshold value M_{th} and the beam waist radius w_0 respectively.

Material threshold M_{th}

One of the main values that is unknown is the threshold amount of dissolvable DNQ in the photoresist. This is a material property and because there is not much known about this resist, this threshold value can be varied. The variable can be found in the equation as M_{th} and it will always be lower than 1. Since this is a ratio with the initial value of DNQ present in the polymer, the decision was made to set $M_0 = 1$ and $0 < M_{th} < 1$. To illustrate the influence of M_{th} on the equation. Fig. A-1 was generated. The influence is shown with a value for $Ct = 5 \times 10^{-60}$.

Material constant C and exposure time t

The influence of Ct will be shown by using the stated value for each variable in Table 4-1. Looking at the expected values of C and t , it is decided to look in the range of 1×10^{-60} to 1×10^{-59} . The other main variables are chosen as follows: $M_{th} = 0.1$ and for w_0 Eq. (4-4b) is used. The result is shown in Fig. A-2.

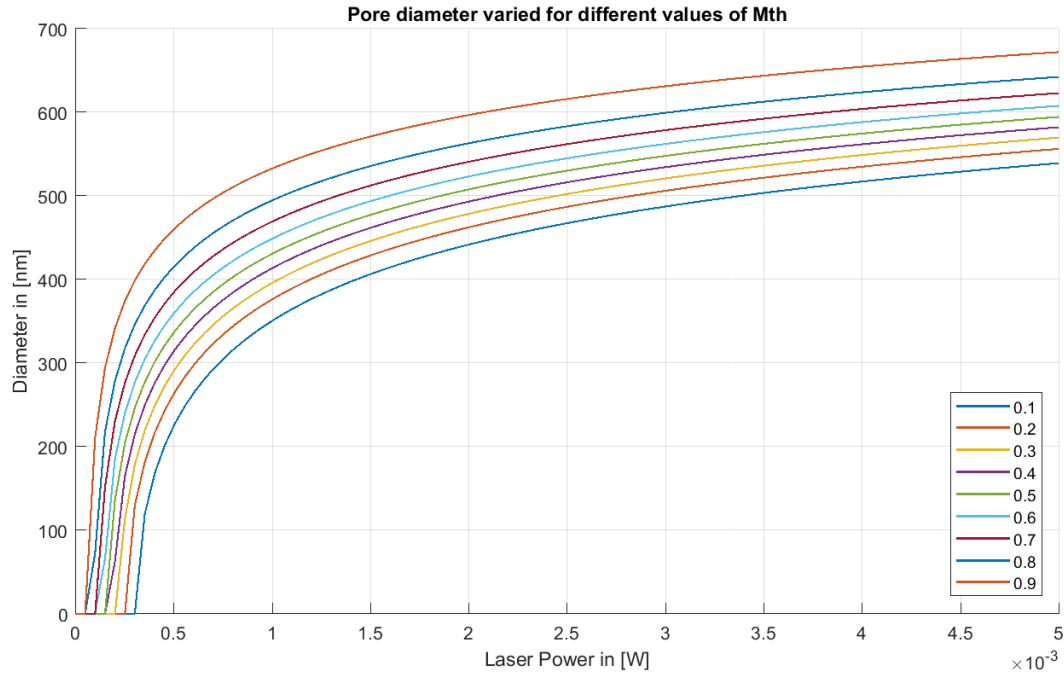


Figure A-1: Mathematical influence of the material threshold value M_{th} .

The influence of w_0

The values used were again $M_{th} = 0.1$ and $Ct = 5 \times 10^{-60}$. The beam waist radius is generally described by $w_0 = \frac{\lambda}{\pi N_A}$, so to illustrate the influence of the beam waist radius on the calculated results, a multiplier is used and varied. It can be seen that the beam waist radius fundamentally changes the shape of the calculated result. Therefore this variable will be kept separate, leaving two fitting variables K_{CtM} and w_0 .

Conclusion for fitting

Out of this research it can be seen that to simplify the fitting model even more, Ct and M_{th} can be taken together in to a variable K_{CtM} . This value together with the beam waist radius w_0 are the two fitting variables used for the calculations.

$$K_{CtM} = \frac{Ct}{\ln\left(\frac{M_0}{M_{th}}\right)} \quad (\text{A-20})$$

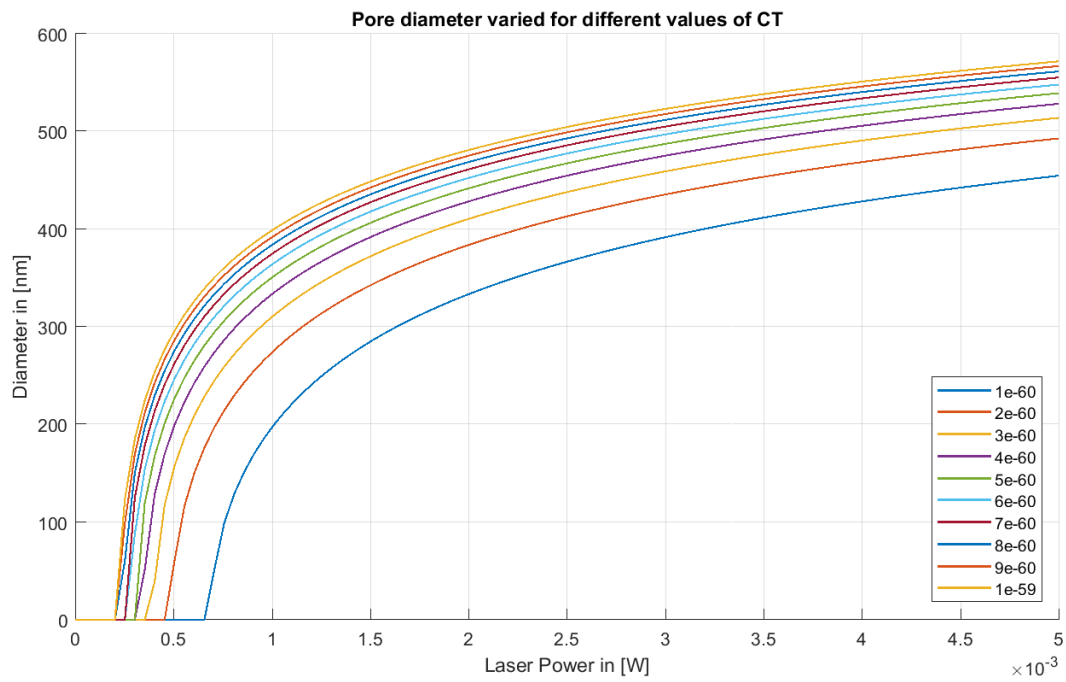


Figure A-2: Mathematical influence of the two-photon absorption constant C and exposure time t combined as Ct .

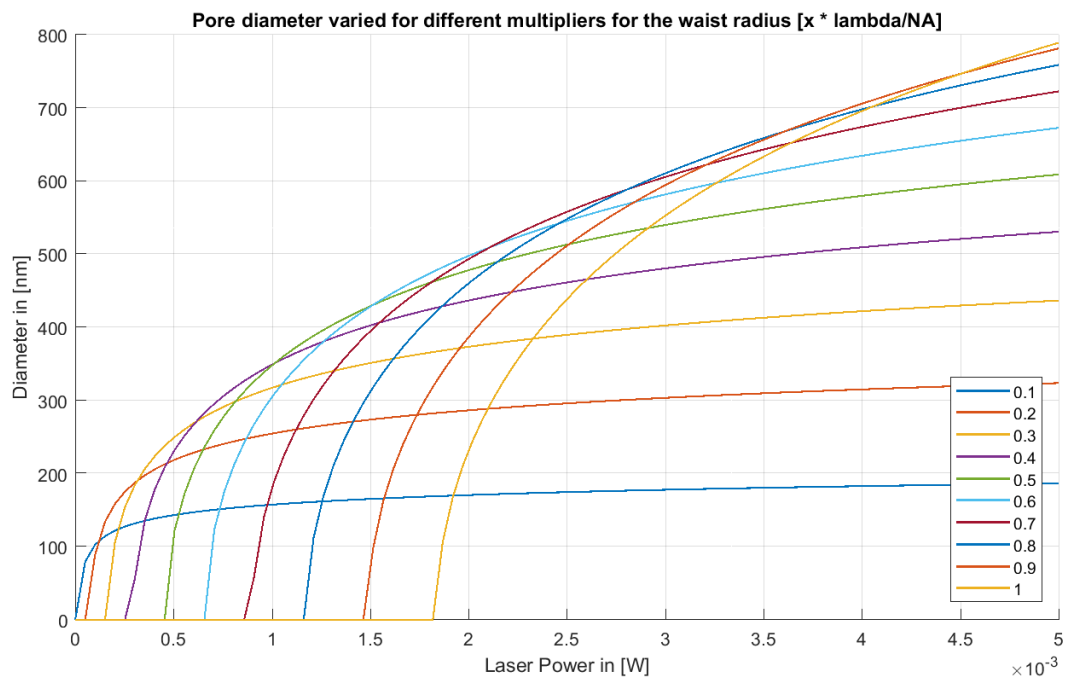


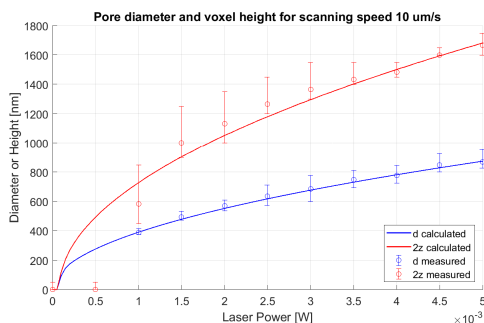
Figure A-3: Mathematical influence of the beam waist radius w_0 .

Appendix B

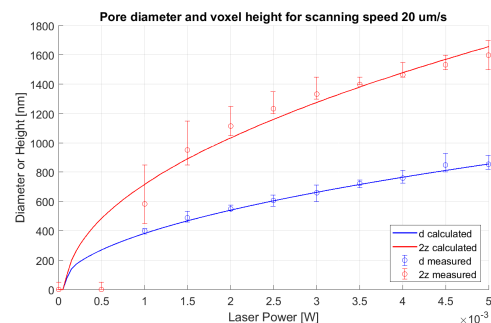
Experimental results

B-1 Data and model fits for different scanning speeds

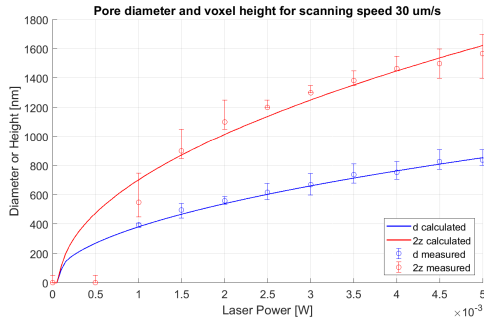
The following figures display the data that was obtained during the experiments performed to find the voxel diameter and voxel height. The scanning speed was varied between 10 - 100 $\mu m/s$ and the laser power was varied between 0.5 - 5 mW . The fitted curves and the obtained values for K_{CtM} and w_0 are given.



(a) Pore diameter and voxel height for a scanning speed of 10 $\mu m/s$.
 $K_{CtM} = 3.28 \times 10^{-60} m^4 s^2$
 $w_0 = 126.15nm$



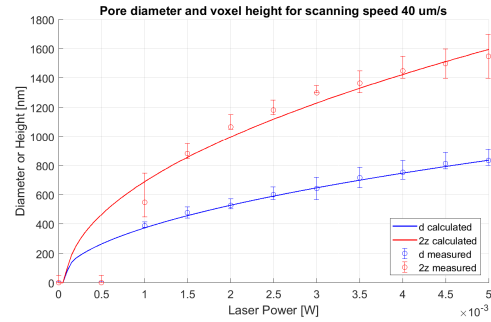
(b) Pore diameter and voxel height for a scanning speed of 20 $\mu m/s$.
 $K_{CtM} = 3.00 \times 10^{-60} m^4 s^2$
 $w_0 = 127.13nm$



(c) Pore diameter and voxel height for a scanning speed of $30 \mu\text{m}/\text{s}$.

$$K_{CtM} = 2.99 \times 10^{-60} \text{ m}^4 \text{ s}^2$$

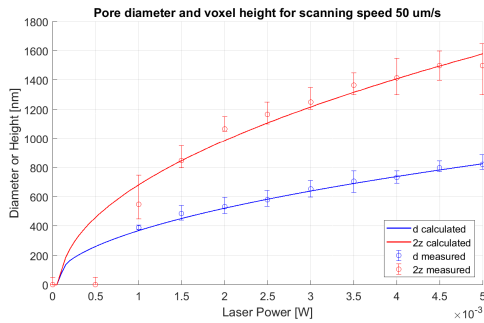
$$w_0 = 124.64 \text{ nm}$$



(d) Pore diameter and voxel height for a scanning speed of $40 \mu\text{m}/\text{s}$.

$$K_{CtM} = 2.75 \times 10^{-60} \text{ m}^4 \text{ s}^2$$

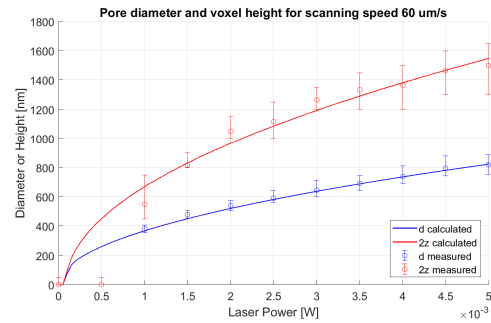
$$w_0 = 125.14 \text{ nm}$$



(e) Pore diameter and voxel height for a scanning speed of $50 \mu\text{m}/\text{s}$.

$$K_{CtM} = 2.61 \times 10^{-60} \text{ m}^4 \text{ s}^2$$

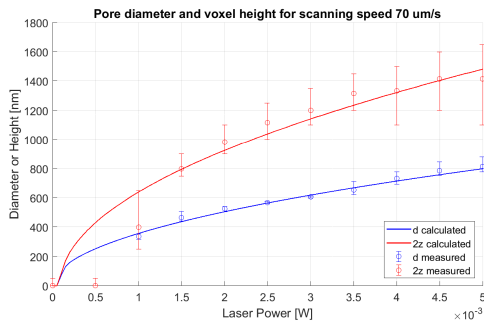
$$w_0 = 125.45 \text{ nm}$$



(f) Pore diameter and voxel height for a scanning speed of $60 \mu\text{m}/\text{s}$.

$$K_{CtM} = 2.58 \times 10^{-60} \text{ m}^4 \text{ s}^2$$

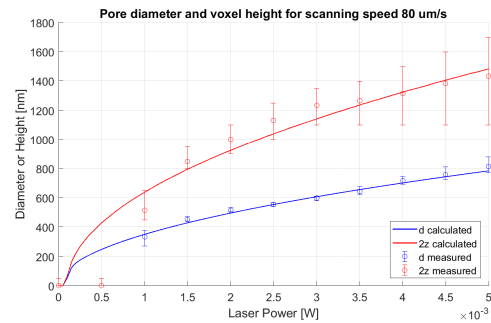
$$w_0 = 123.37 \text{ nm}$$



(g) Pore diameter and voxel height for a scanning speed of $70 \mu\text{m}/\text{s}$.

$$K_{CtM} = 2.29 \times 10^{-60} \text{ m}^4 \text{ s}^2$$

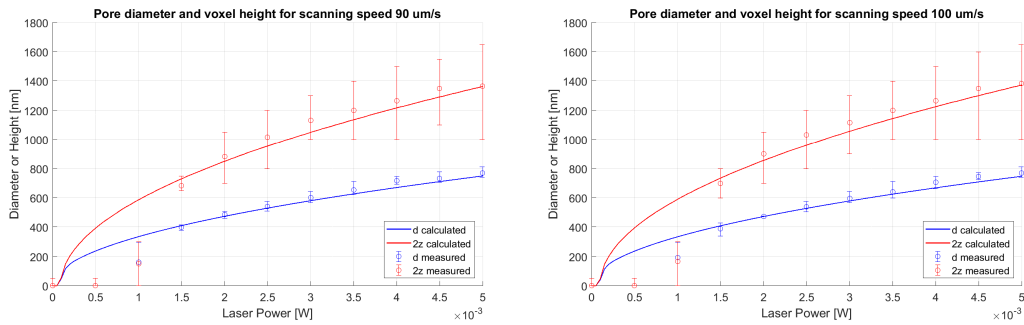
$$w_0 = 121.68 \text{ nm}$$



(h) Pore diameter and voxel height for a scanning speed of $80 \mu\text{m}/\text{s}$.

$$K_{CtM} = 2.13 \times 10^{-60} \text{ m}^4 \text{ s}^2$$

$$w_0 = 124.19 \text{ nm}$$



(i) Pore diameter and voxel height for a scanning speed of $90 \mu\text{m}/\text{s}$.
 $K_{CTM} = 1.77 \times 10^{-60} \text{ m}^4 \text{ s}^2$
 $w_0 = 119.45 \text{ nm}$

(j) Pore diameter and voxel height for a scanning speed of $100 \mu\text{m}/\text{s}$.
 $K_{CTM} = 1.75 \times 10^{-60} \text{ m}^4 \text{ s}^2$
 $w_0 = 120.68 \text{ nm}$

Figure B-1: The fitted curves that were obtained for the voxel height and diameter experiments.

Extra voxel height and diameter measurement

For a laser power of 3.5 mW and a scanning speed of $100 \mu\text{m}/\text{s}$, the voxel was also measured. The obtained data points are shown in Figure B-2b in red and the prediction of the voxel shape is shown in blue.

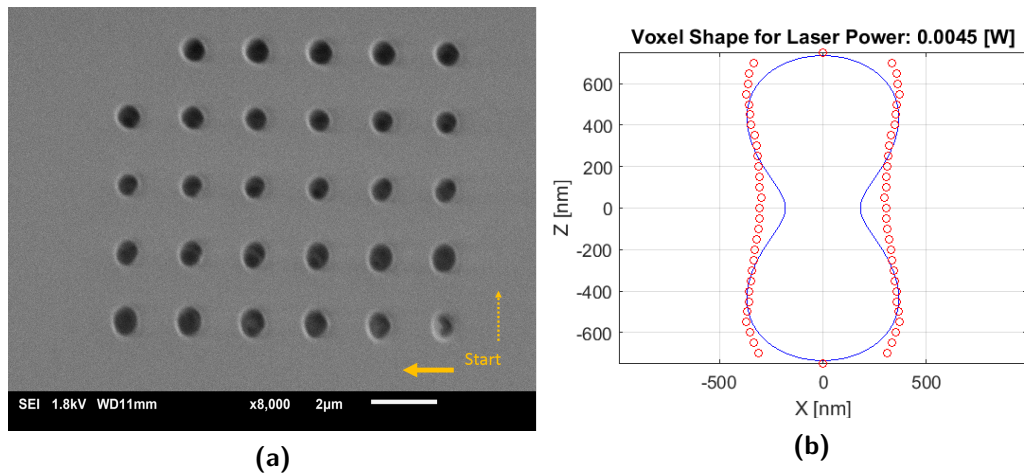
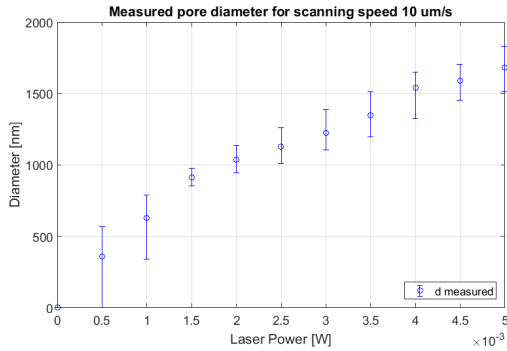


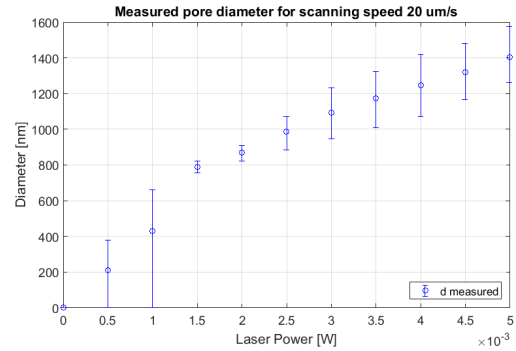
Figure B-2: (a) A micrograph of the voxel height and diameter test for a laser power of 3.5 mW and scanning speed $100 \mu\text{m}/\text{s}$. (b) The measured diameter and height for laser power 3.5 mW and scanning speed $100 \mu\text{m}/\text{s}$.

B-2 Data from scanning voxel

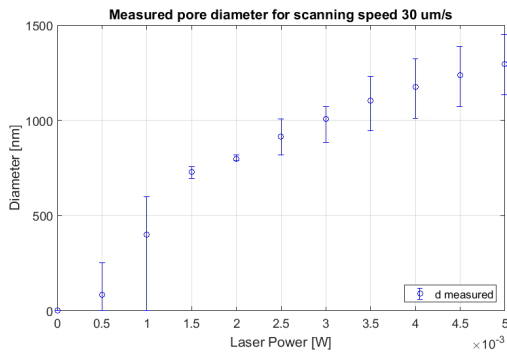
The following figures display the data obtained when pores were created with a scanning voxel. The voxel height was not measured during these experiments, so there was no curve fitted onto this data, because the results would not be relevant.



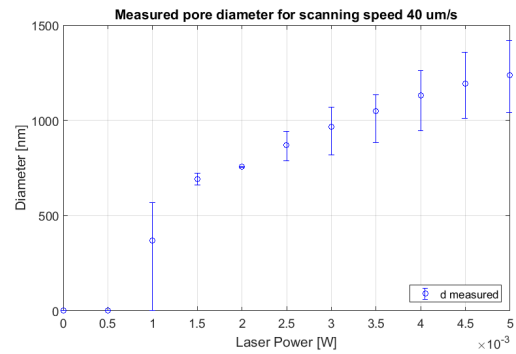
(a) Pore diameter for a scanning speed of 10 $\mu\text{m/s}$.



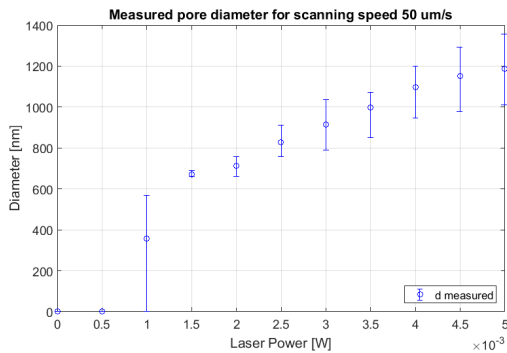
(b) Pore diameter for a scanning speed of 20 $\mu\text{m/s}$.



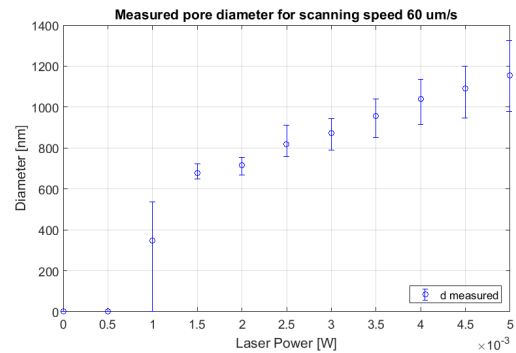
(c) Pore diameter for a scanning speed of 30 $\mu\text{m/s}$.



(d) Pore diameter for a scanning speed of 40 $\mu\text{m/s}$.



(e) Pore diameter for a scanning speed of 50 $\mu\text{m/s}$.



(f) Pore diameter for a scanning speed of 60 $\mu\text{m/s}$.

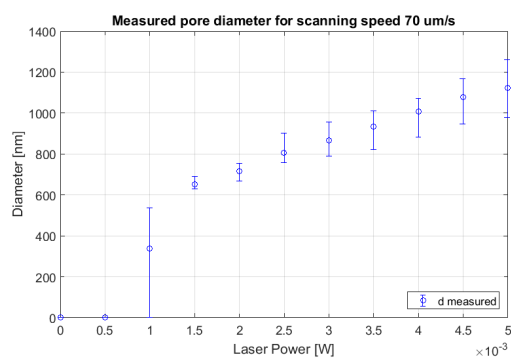
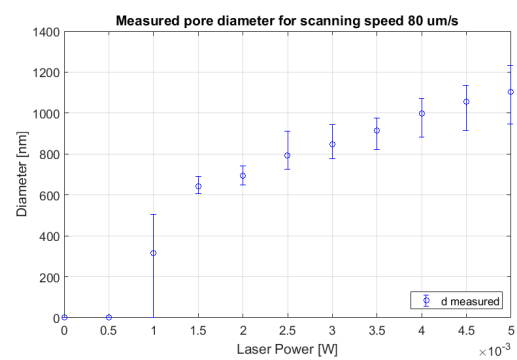
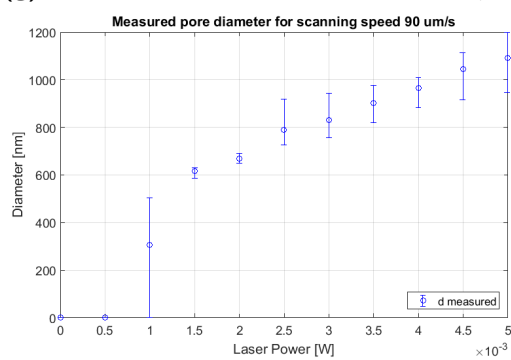
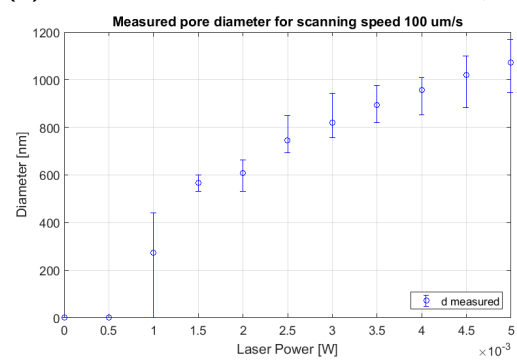
(g) Pore diameter for a scanning speed of 70 $\mu\text{m/s}$.(h) Pore diameter for a scanning speed of 80 $\mu\text{m/s}$.(i) Pore diameter for a scanning speed of 90 $\mu\text{m/s}$.(j) Pore diameter for a scanning speed of 100 $\mu\text{m/s}$.

Figure B-3: The pore diameter measured from the initial experiment. The voxel was scanned through the material.

B-3 3D structures

This section shows additional results obtained from the second phase of the research. In this phase 3D manufacturing was investigated.

3D structures

Figure B-4a shows an overview of the 3D structures that were produced. The produced cones are shown in Figure B-4b. Slope angles between 54° and 90° were produced. For the pyramids shown in Figure B-4c, slope angles between 63° and 90° were produced. Finally trapeziums with one straight sides were successfully produced for slope angles between 45° and 90° , shown in Figure B-4d.

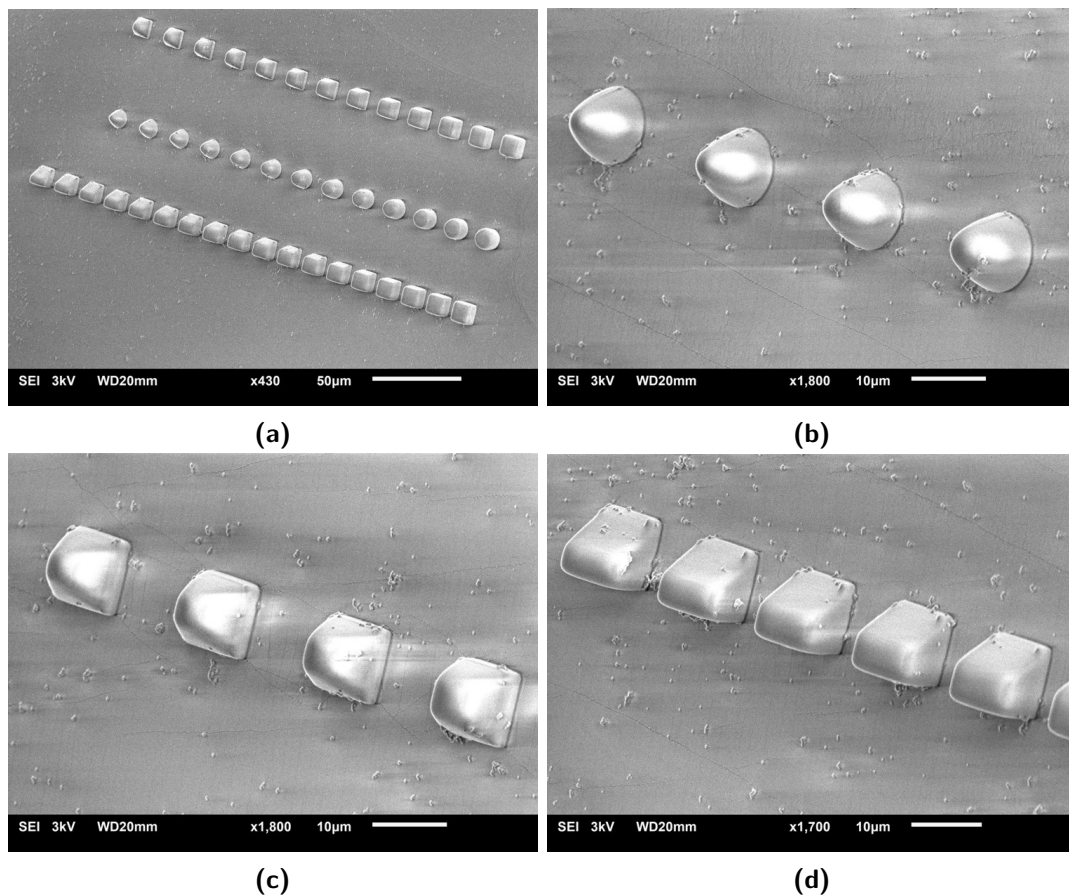


Figure B-4: (a) An overview of the produced 3D features. (b) A micrograph of the cones. (c) A micrograph of the pyramids. (d) A micrograph of the trapeziums with one straight side.

Inverse 3D structures

Figure B-5a shows an overview of the inverse 3D structures that were produced. The inverse cones are shown in Figure B-5b. Slope angles between 81° and 90° were produced. For the pyramids shown in Figure B-5c, slope angles between 74° and 90° were produced. For smaller angles the structures were pulled off the PDMS surface. Finally trapeziums with one straight sides were successfully produced for slope angles between 51° and 90° , shown in Figure B-5d.

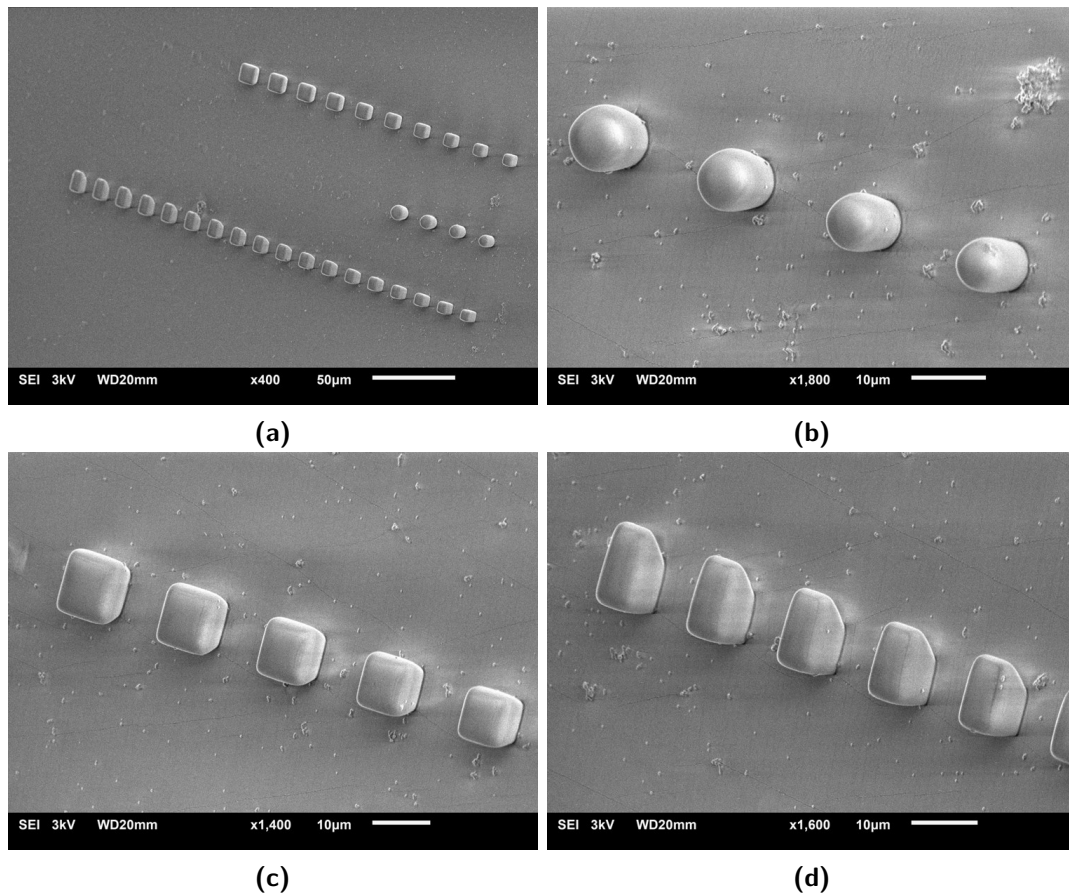


Figure B-5: (a) An overview of the produced inverse 3D features. (b) A micrograph of the inverse cones. (c) A micrograph of the inverse pyramids. (d) A micrograph of the inverse trapeziums with one straight side.

B-4 Channel and chip manufacturing

Figure B-6a shows a successfully produced chip, where the top channel unfortunately cracked. This failure however, does allow us to see that both of the channels are there. Figure B-6b shows an SEM micrograph of the chip. The intersection of the channels is shown in Figure B-6c. The lower channel is clearly visible. Finally in Figure B-6d the cracked surface at the in- or outlet hole is shown.

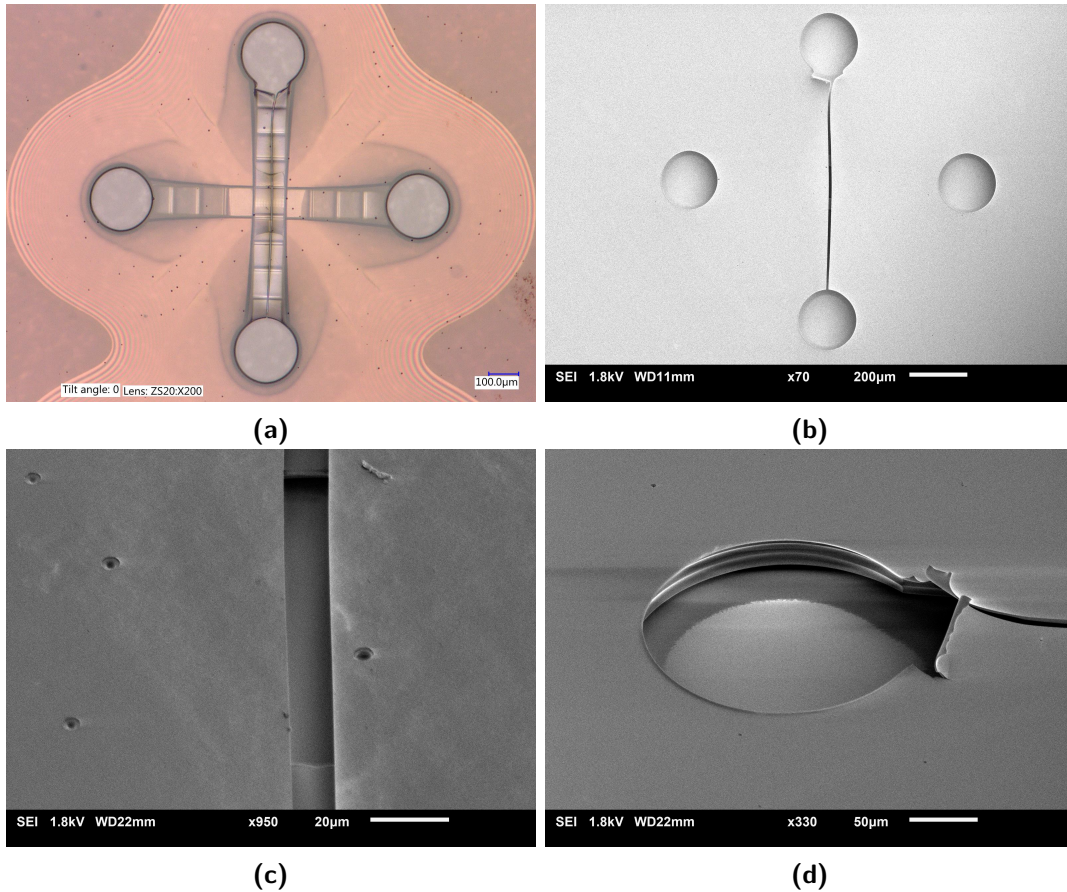


Figure B-6: A cracked surface shows that both channels are there at different heights.

Appendix C

Writing protocols

In this Appendix protocols are given for working with TPL and AZ 4562. First a general protocol is given, then a guide for finding the interface is shown. After tips for writing in Piezo mode, writing in Galvomode, channel manufacturing and PDMS stamping are given. In the Nanoscribe computer, a folder with general writing jobs is left.

C-1 General protocol

IMPORTANT: Before working with this resist, read the safety manuals stored in the cabinet in the yellow lab.

30 minutes before preparing the sample, preheat the hotplate to $110\text{ }^{\circ}\text{C}$ and take the AZ 4562 out of the fridge to get it to room temperature. After this is done, follow the next steps:

1. **Sample preparation:** Clean the glass slide with IPA, dry with the air blower or an extra clean tissue. Check the sample for particles, they can ruin the spincoat step.
2. (Optional) Use aluminum foil to prevent the spin coater from getting dirty.
3. Turn on the spincoater, turn on the motor underneath the fume hood and switch the valve on the CDA cable.
4. Select the spincoating program, the one used in this research is B on the machine, for single step $10\text{ }\mu\text{m}$ coating. (Check the channel manufacturing section for multiple layer coating.) The program should be:
 - Disperse resist: 5 seconds on 500 rpm, acceleration 10 kprm/s
 - Spread resist: 20 seconds on 2300 rpm, acceleration 10 kprm/s
5. Place the glass slide on the spincoater and turn on vacuum.

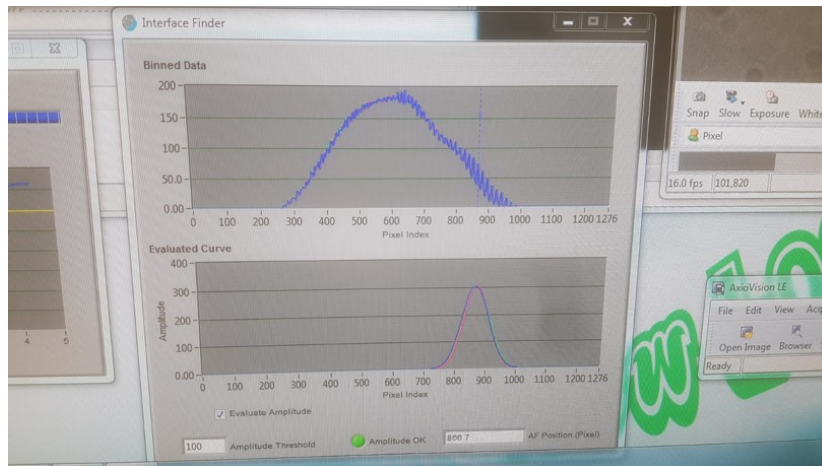
6. Disperse resist with a large pipette, fill it almost until the edge to be sure there is enough resist.
7. Start the spincoater.
8. (Optional) Remove resist on the edges with acetone (EBR).
9. Place the sample on an old silicon wafer (to avoid the hotplate from getting dirty) and in the hotplate for 1 minute per $2 \mu m$.
10. Let the sample hydrate for 15-20 minutes. Without the hydration the chemical reaction with water can not take place.
11. Place the sample on the holder with the resist pointing down, the DiLL holder should be with the bottom side up. Place a drop of oil on the bottom side.
12. **Exposure:** Place the holder in the machine, find the interface (described below), load and start your job.
13. **Development:** Make sure the beakers are cleaned with IPA and DI-water.
14. Prepare the developer solution: AZ 400K : DI-water in a 1:4 ratio.
15. Develop for 1 minute per $2 \mu m$.
16. Dry sample with the air blower.

C-2 Interface finding

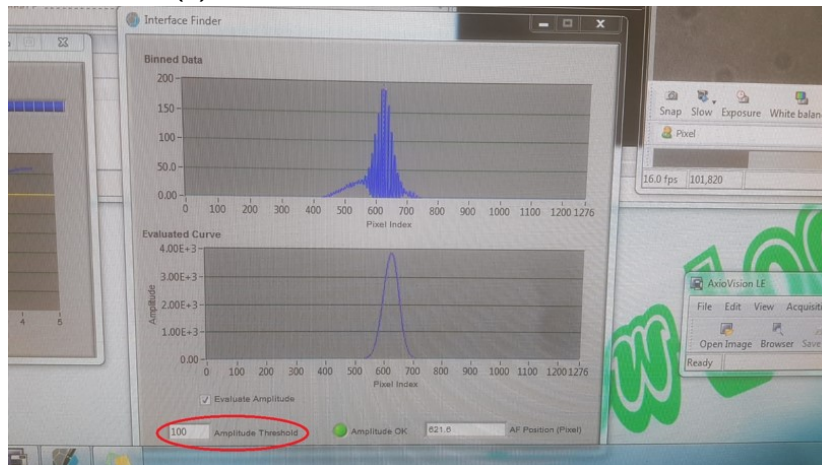
There are two different interfaces: Glass - Resist, which will give a signal with a low amplitude and Resist - Air, which will give a signal with a very high amplitude. You will not find the right interface with the standard settings of the machine. Make sure that before pressing Approach Sample the following settings are correct:

- The machine is in conventional mode.
- Set Amplitude Threshold to 100. The final signal will be much higher, but this is enough to skip the first interface. If there are still problems with finding the interface, try a higher Amplitude Threshold. Finally you can try to manually move the objective closer to the sample to skip the first interface.
- If you write in conventional mode and want to start writing in the air above the resist to make sure the voxel goes all the way through, use FindInterface 1 with InvertZAxis 1.

Now the right interface should be found. Typical values are 3000 - 6000 @98. Typical height is 10.28 - 10.33 *mm*.



(a) Small disturbance due to the first interface.



(b) The second interface with a red circle around the Amplitude threshold.

Figure C-1: Interface signals in the Photonic Professional GT.

C-3 Piezo mode writing

This part of the protocol is written for piezo mode writing in conventional mode. Watch the following points before you start writing.

1. If you need to go all the way through the layer, make sure to add the command `FindInterfaceAt 1`, and `InvertZAxis 1`.
2. Avoid negative Offsets in your script, this will not be written.
3. Recommended settings:
 - Laser power 3 - 10 %
 - Scanning speed 10 - 100 $\mu\text{m}/\text{s}$. You can adjust the scanning speed by the commands `PointDistance` and `UpdateRate`. Leave `PointDistance` at 10. Set `UpdateRate` at 1000 - 10000, for a scanning speed between 10 - 100 $\mu\text{m}/\text{s}$.

4. Make sure to use MeasureTilt 5, and put TiltCorrectionOn. This will not correct perfectly, but it gives an indication of how high above the sample you have to start writing.

C-4 Galvo mode writing

This part is written for writing in Galvo mode.

1. Recommended settings:
 - Laser power: 20 %
 - Scanning speed: 20 *mm/s*
 - Slicing: 0.3 μm
 - Hatching: 0.06 μm

C-5 Stamp/Mold for PDMS

The recommended recipe for creating the PDMS structures is given below.

- Elastomer and curing agent ratio 10:1.
- Mix for 5 minutes.
- Pour the mix on the AZ 4562.
- Remove bubbles in desiccator for 30 minutes.
- Cure in oven at 70 °C for at least 60 minutes.
- (Only for inverse 3D structures) Make a small incision so that the AZ can be accessed and put the whole sample in acetone to dissolve the resist.
- (For reusable stamp/mold) Carefully remove the PDMS from the resist.

C-6 Channel manufacturing

For channel manufacturing, you may want to use a thicker layer of AZ 4562. To get a thicker layer, follow these steps:

Channels:

- Writing channels with inlet and outlet will be done in Galvo mode. The recommended settings are therefore the ones mentioned in the Galvo mode section.
- Make sure that the channels are written in blocks that in any direction are not longer than 180 μm . Recommended length is 100 μm per block.

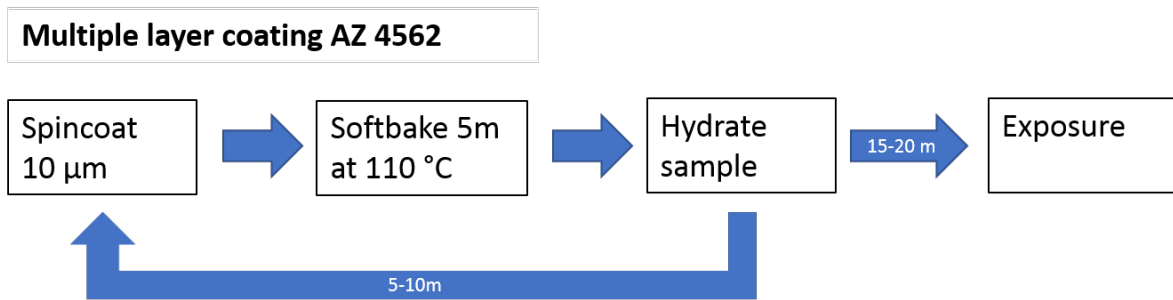


Figure C-2: For multiple layer coating, at hydration, follow the arrow back to spincoating, until the final layer is thick enough.

- Do not forget to set the right ZOffset under the surface.
- The laser power is high, so reduce the channel height settings to compensate. Recommended setting for a 10 μm high channel is a height of 7 μm in the code. The dark erosion will also increase the final channel height.

In- and outlet:

- Make sure that the radius of the in- or outlet is in the center of the writing area. Otherwise the area is not large enough to write it.
- Downsize the holes in the design to cope with dark erosion.

Development:

For the development of the channel there are do's and don'ts. The things to take into account are given below.

- Use the magnetic stirrer. The AZ 400K developer and the water will eventually separate. This will result in a concentration of AZ 400K at the bottom of the beaker that is too large and will dissolve the AZ 4562. The top will lack AZ 400K and it will not develop anymore. The magnetic stirrer keeps the liquids mixed. Recommended setting: 6.
- Do **not** use the ultrasonic shaker. It will destroy the pores.
- Do **not** heat up the developer solution. The developer will affect unexposed volume more.
- The recommended development time depends on the length of the channels. 60 minutes was enough to develop channels with a length of 380 μm .
- After developing, put the sample on the holder in DI-water to clear out the developer from the channels.
- Let the sample dry for 1-3 days.

Appendix D

Project steps, designs and decisions

This work was divided into three phases as described in the introduction. Each of these phases had deliverables and finally a milestone. In this appendix, the iteration steps that were made to achieve these goals are given. First the finding of the interface is described, after which the project steps for the Galvo scan mode and the steps for Piezo scan mode are given. Then information about the 3D manufacturing phase and finally the steps taken in the integration phase are shown.

D-1 Finding the interface

The software for the Photonic Professional GT will start writing at a certain Z-position. To make sure the material is exposed as desired, it is important to find the surface of the resist. There are two locations where this surface can be found, which is against the glass substrate, and at the top surface. The machine will find the interface by looking at a difference in refractive index. In Fig. D-1 the setup with each layer of material is shown. The immersion oil was specifically designed for this glass substrate, giving it the same refractive index. This means that the machine will not notice this interface. The first noticeable interface is between the glass and the photoresist. The photoresist has a higher refractive index, creating a signal. However, when this interface is found, a different signal is already visible a small distance ahead. The other signal is at the interface between the resist and the air. The difference in refractive index is much higher for this interface, giving a signal with a higher amplitude. The fact that there are two interfaces very close to each other, causes the machine to be stuck between them and not find one interface. Therefore the solution is to search for a higher signal only, skipping the first interface and finding only the second one. Practical tests showed that an amplitude of 100 or higher is sufficient to skip the first interface and to find the second one.

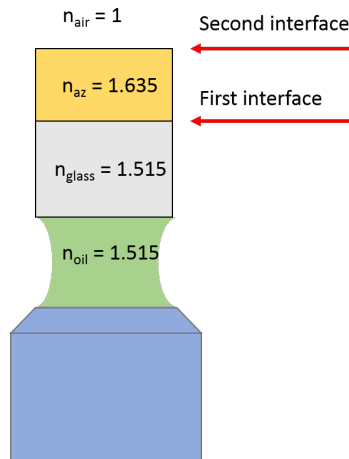


Figure D-1: Interfaces in the writing configuration.

D-2 Project steps for Galvo Scan Mode

There are two different writing modes for the Photonic Professional GT. Galvo scan mode is used for high processing speed and Piezo scan mode is used for high resolution features. In this research Galvo scan mode was used for the larger features, i.e. channels and in- and outlet holes. Piezo scan mode was used for the manufacturing of the pores. In this section the project steps for Galvo scan mode are discussed.

Galvo scan mode makes use of galvano mirrors for the positioning of the laser, making it suitable for manufacturing at higher scanning speed. In theory this mode should be able to achieve high resolution as well, but the higher processing speed will lead to less positioning accuracy and therefore lower resolution. Recommended scanning speeds are between 1000 - 20000 $\mu\text{m}/\text{s}$.

Designs

For the first research step the decision was made to remove structures that could be well observed with an optical microscope. Therefore square pores with walls of 10 μm were designed. Three different designs for a single square layer were designed and tested. The designs were made with the Describe software by Nanoscribe and they are shown in Figures D-2a, D-2b, D-2c and D-2d.

No significant difference between the designs was discovered at this scale, for smaller features there could be a difference, but that is irrelevant for writing in Galvo mode. The decision has been made to continue the experiments with the design shown in Fig. D-2b. For round features, the same format was used, shown in Fig. D-2d. First the edge is written, which then is filled with lines. To create higher structures, these layers are stacked on top of each other with a distance known as the slicing value. Later in this Appendix, the steps to find the optimal slicing value are shown.

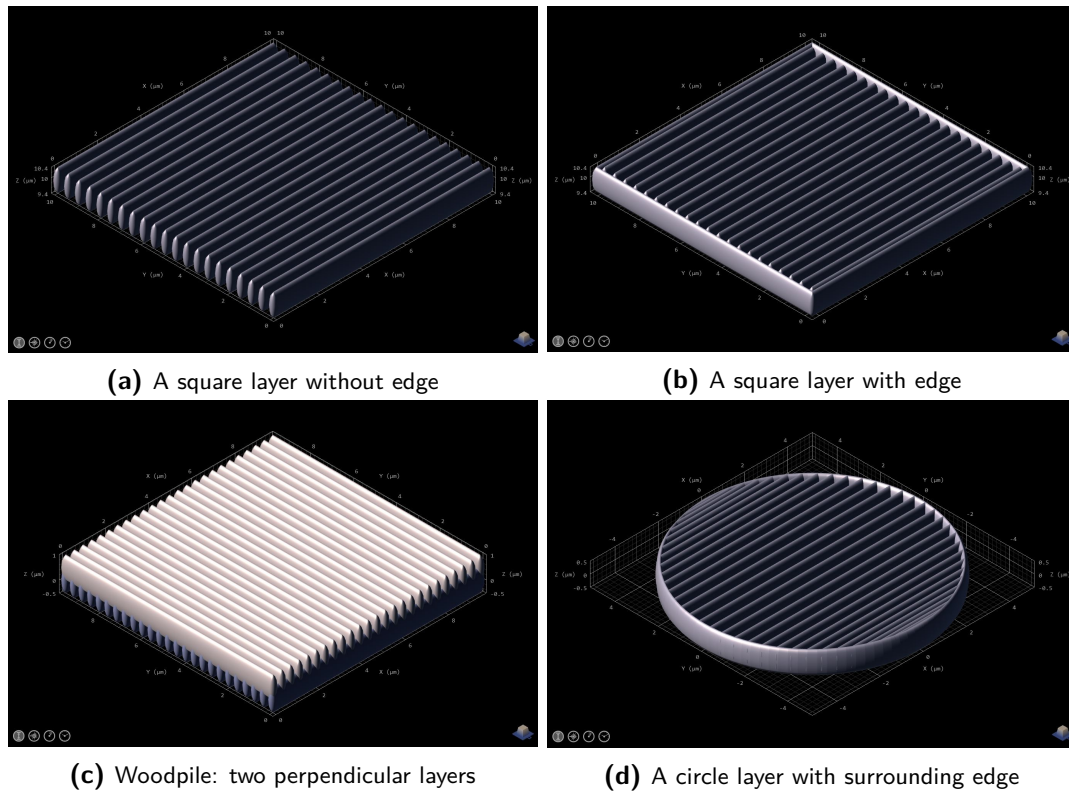


Figure D-2: Four different Describe designs for large pores.

Optimizing parameters

For the Galvo Scan Mode there are four main parameters that need to be optimized. The laser power and scanning speed together determine the laser dose to which the resist is exposed. The slicing is the height difference between different layers and hatching is the distance between two lines at the horizontal plane. For the Galvo Scan Mode, the goal is to find the parameters for which the process time is minimized, but still reliable results are obtained.

Scanning speed

The recommended scanning speed by Nanoscribe is between $1000 - 20000 \mu\text{m}/\text{s}$. However, the machine can be put on values high above $20 \text{ mm}/\text{s}$. At higher speeds the result may not be as fast a predicted. This is due to acceleration and deceleration limits of the machine. A test was performed to compare the predicted process time with the actual process time. The design for a channel was chosen, because this feature is desired later in the research. The channels were open at the top. For this test the optimal laser power was not known, so the laser power was set on 25% or 12.5 mW . The actual process time was not the same as predicted. The optimal scanning speed was found at $24 \text{ mm}/\text{s}$. The same test was taken three times and gave exactly the same process time for every independent test.

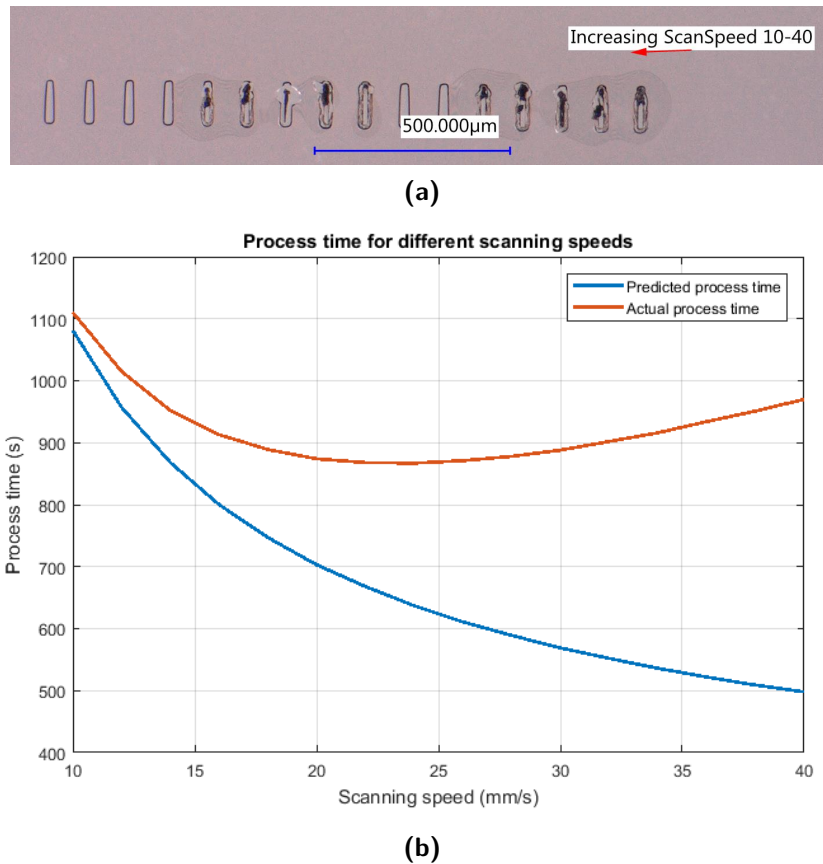
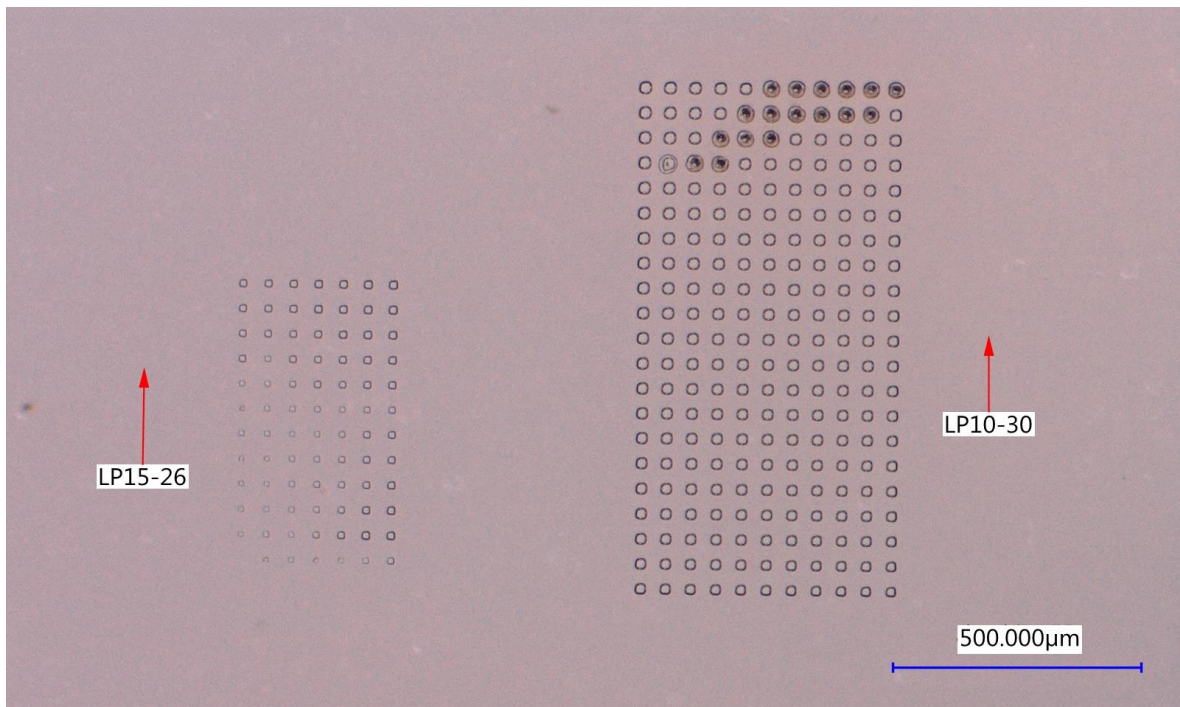


Figure D-3: (a) Array of open channels. (b) The predicted process time in blue and the actual process time in red.

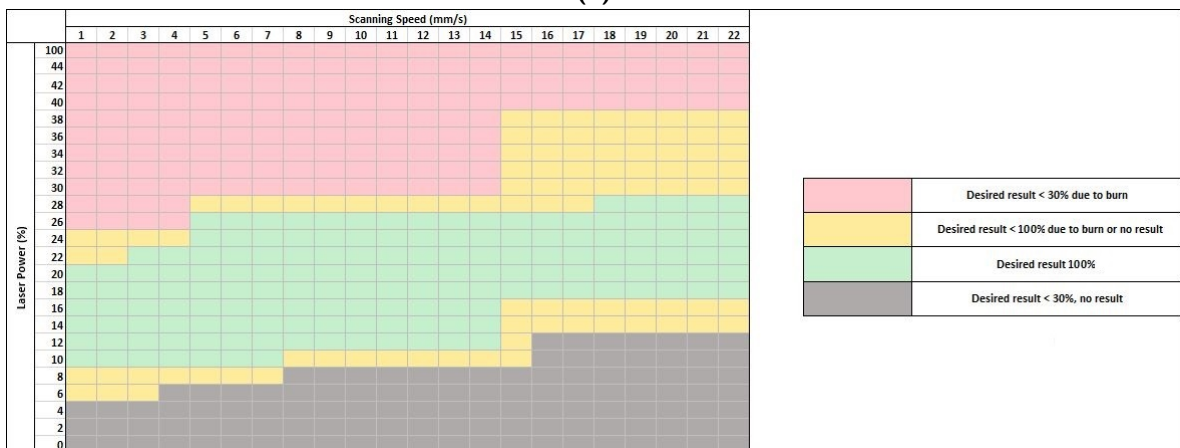
Laser power

For a reliable writing process it is important that the structures are written every time, but they should not burn. To find reliable combinations between laser power and scanning speed, parameter sweeps were done like the one shown in Figure D-4a. The initial experiments were done for square pores of $10 \times 10 \mu\text{m}$, because they are clearly visible in an optical microscope. The values for slicing and hatching were not yet optimized, and chosen to be $0.5 \mu\text{m}$ and $0.4 \mu\text{m}$ respectively. The parameter sweeps were done for a laser power between 1 - 44%, which is 0.5 - 22 mW. The result is shown in Figure D-4b and it can be seen that for laser powers above 40% every pore burned. Therefore it was assumed that the same will happen for higher laser powers. Nearly every single combination in this overview was tested multiple times, but if a combination was missing, the result was interpolated from surrounding combinations. The borders of the green area are not completely reliable as particles could sometimes cause a pore to burn and a sample tilt or the fact that slicing and hatching were not yet optimized could prevent the pore being written. The green area however, was reliable in all of the experiments.

In the end a combination of a laser power of 20% and a scanning speed of 20 mm/s was chosen to continue with. The laser power gives reliable results and the scanning speed is fast and still in the range of recommended scanning speeds.



(a)



(b) Overview of scanning speed and laser power tests for Galvo mode

Figure D-4: (a) Parameter sweeps 10x10 μm square pores. (b) Overview of laser power vs. scanning speed for Galvo scan mode.

Slicing and Hatching

Besides laser power and scanning speed there are two more important parameters for a design in Galvo mode. The distance between two layers in z-direction, also known as slicing, and the distance between two lines within the xy-plane, called hatching. Parameter sweeps were done to find the optimal value. Based on values for slicing and hatching used in other researches, for slicing values between 0.1 and 1 μm were tested. For hatching values between 0.01 and 0.1 μm . Slicing and hatching did not influence the result much. Finally a slicing value of 0.3 μm and a hatching value of 0.06 μm were chosen to continue with.

Conclusions for Galvo Scan mode

Finally the writing parameters for Galvo Scan mode were:

- Laser power: 20%, 10 *mW*
- Scanning speed: 20 *mm/s*
- Slicing: 0.3 μm
- Hatching: 0.06 μm

More results for structures written in Galvo Scan mode are shown in sections that cover 3D manufacturing and the fabrication of the microfluidic chip.

D-3 Project steps for Piezo Scan mode

The second writing mode is called Piezo Scan mode. This mode makes use of a piezo-electric actuator to position the focal point of the laser. This mode has higher resolution and can be used for very low scanning speeds. The recommended speed is between 25 - 300 $\mu m/s$. In Piezo mode there is no slicing or hatching, because we work with single voxel lines. Therefore the result only depends on laser power and scanning speed. This writing mode was used for the manufacturing of trenches and pores and the experiments to determine the voxel diameter and height. For the lower scanning speed, still the optimal combination with a laser power had to be found.

Designs

Different designs were made for the parameter sweeps and other experiments that were done in Piezo Scan mode. Figure D-5a shows the parameter sweep for the trenches that were and will be discussed below. The colors indicate the scanning speed, where red is the fastest and blue the slowest. In Figure D-5b nine pores are shown. These pores are written by vertically moving the voxel through the resist and the number was chosen to get a more reliable measurement. An example of a parameter sweep design for pore manufacturing is given in Figure D-5c. The colors again indicate the different scanning speeds. Finally in Figure D-5d the experiment done to test the voxel height and diameter is shown. This time the colors indicate the time when the voxel is written. As visible the voxel is lowered in small steps.

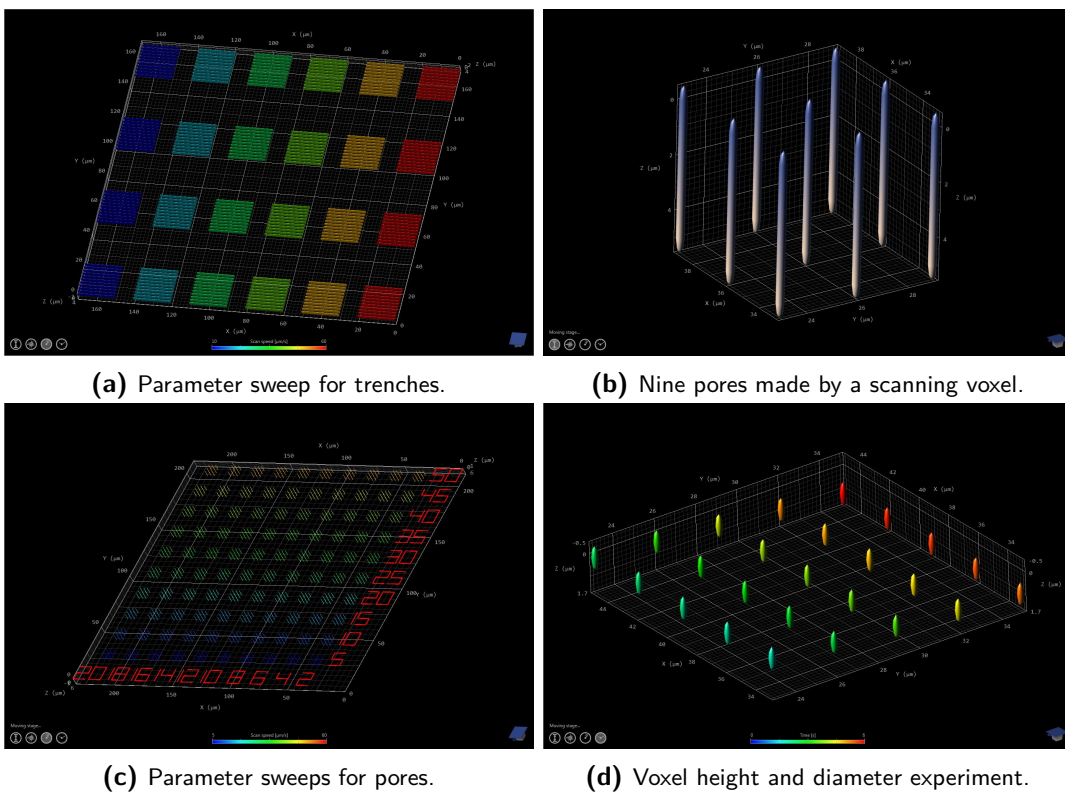
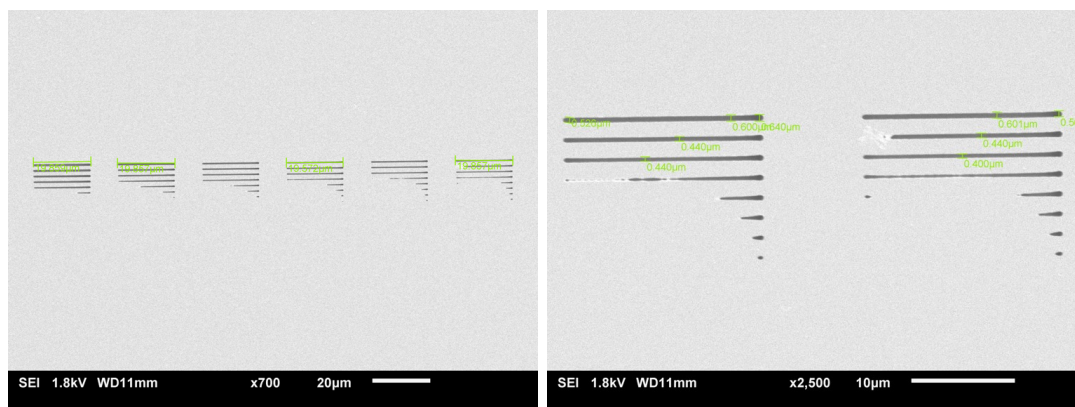


Figure D-5: The different Describe designs made for Piezo Scan mode writing.

Trenches

Inspired by the paper of Cao et al. [41], the first piezo experiments were used to create trenches and to compare the results to the paper. Trenches were written for laser powers between 0.25 - 1.15 mW and scanning speeds between 10 - 60 $\mu m/s$. In Figure D-6a an example of a trench overview is given. In Figure D-6b a closer image of two trenches is shown for a scanning speed of respectively 50 and 60 $\mu m/s$. Five different tests were done with very different results. The results are shown in the table given in Figure. D-6c. The main problem with the writing of trenches is that it is only in the horizontal plane. This means that a small tilt or error in the interface finding will prevent any results. Observing this was the reason to continue with the writing of pores instead of trenches.



(a) (b)

Laser Power (mW)		Trench Diameter (nm)					
		Scanning speed ($\mu m/s$)					
		10	20	30	40	50	60
0.25	Min	0	0	0	0	0	0
	Max	0	0	0	0	0	0
0.35	Min	0	0	0	0	0	0
	Max	0	0	0	0	0	0
0.45	Min	0	0	0	0	0	0
	Max	0	0	0	0	0	0
0.55	Min	0	0	0	0	0	0
	Max	0	0	0	0	0	0
0.65	Min	0	0	0	0	0	0
	Max	480	0	0	0	0	0
0.75	Min	0	0	0	0	0	0
	Max	600	440	400	0	0	400
0.95	Min	0	0	0	0	240	360
	Max	720	520	440	480	400	440
1.05	Min	0	0	0	0	400	440
	Max	800	640	522	480	560	480
1.15	Min	0	0	0	0	500	500
	Max	884	724	640	600	600	600

(c)

Figure D-6: (a) Overview of trenches. (b) Closer view of two trenches. (c) Results from trench experiments.

Pores

The goal of the research was to create pores as small as possible, with a diameter that was smaller than $1 \mu m$. The smallest voxel diameter should be obtained for the lowest laser power that still initiates two-photon absorption. Laser powers from 0.5 to $5 mW$ were investigated, for scanning speeds between $10 - 100 \mu m/s$. The results are shown in Appendix B. Figures D-7a and D-7b show an example of the diameter test with the scanning voxel and the height and diameter test with single voxel exposure.

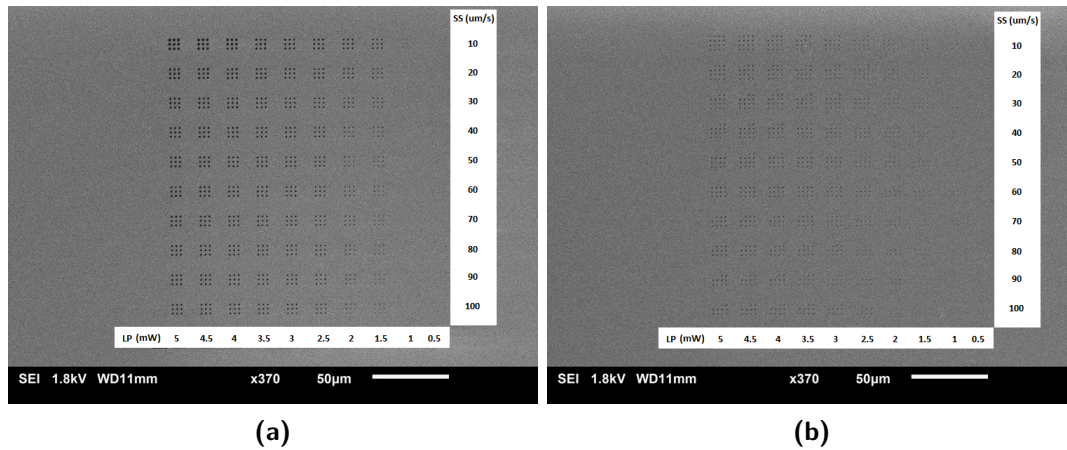


Figure D-7: (a) Dose test with scanning laser to create pores with a length of $10 \mu m$. (b) Test to find voxel height and corresponding voxel diameter, by lowering the voxel with steps of $50 nm$.

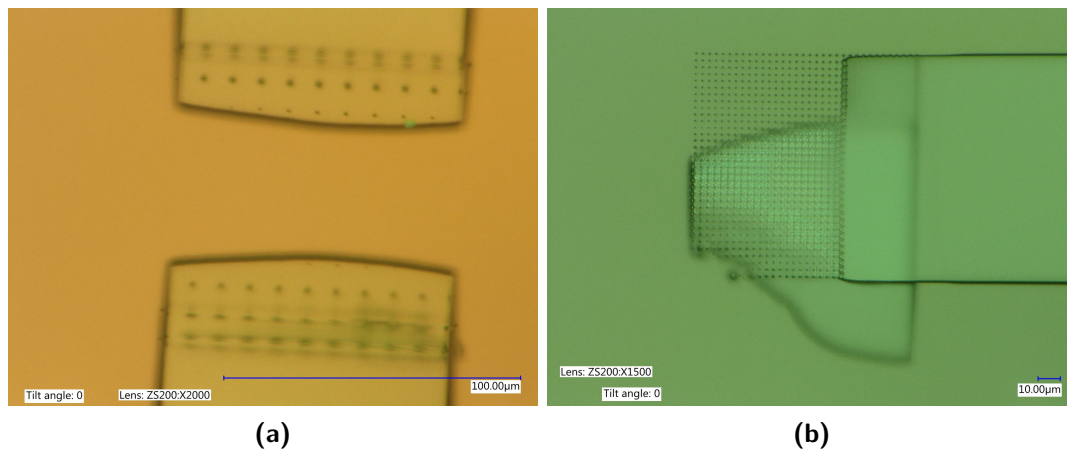


Figure D-8: Two images of channel intersections. The channels were not completely developed, but the pores are clearly visible.

D-4 3D structures

This section discusses the project steps that were taken and led to the results shown in Chapter 5.

Designs

The stamps and molds that have been designed are discussed in Chapter 5. In Figures D-9a and D-9b, the full designs are shown.

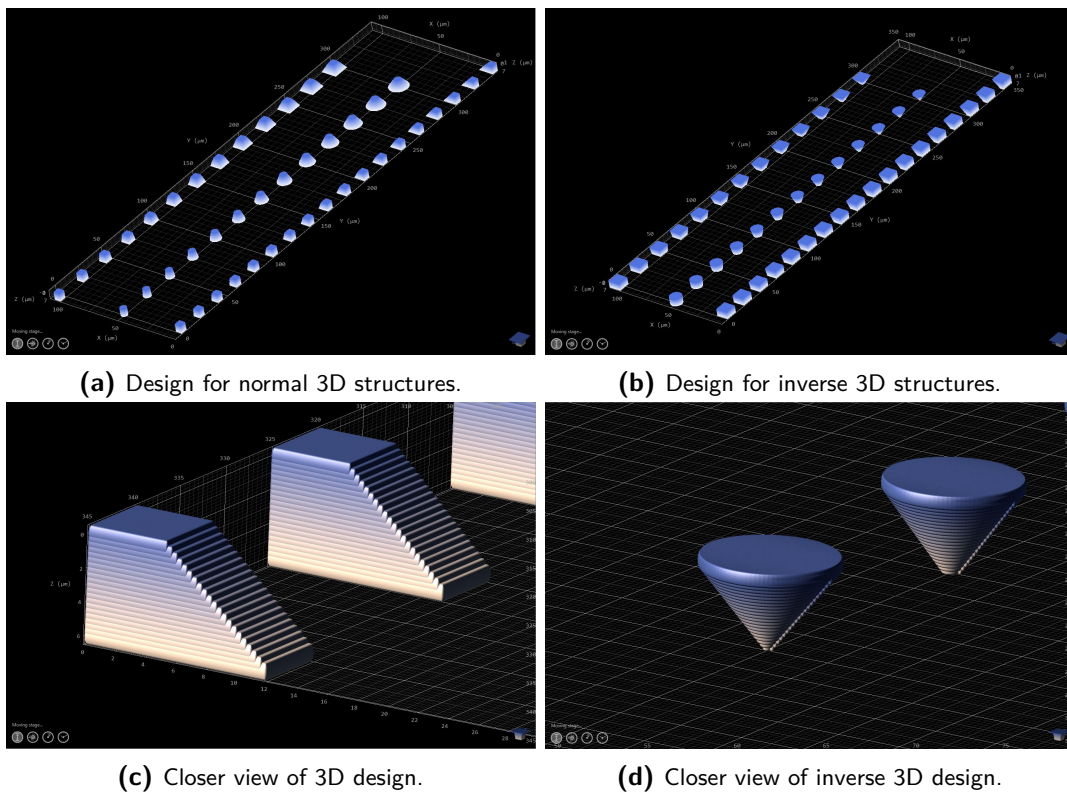


Figure D-9: Describe designs for 3D manufacturing.

First NIL test

The very first test performed to see if a pattern could be transferred from the AZ 4562 to PDMS, was an array of pits of different diameter. In Figure D-10a an optical image of the pits is shown. The transfer is visible more clearly in the SEM picture shown in Figure D-10b. From Figure D-10c it can be observed that the pattern is perfectly transferred. The white light interferometer image in Figure D-10d shows that the pillars are there and around $10 \mu\text{m}$ high.

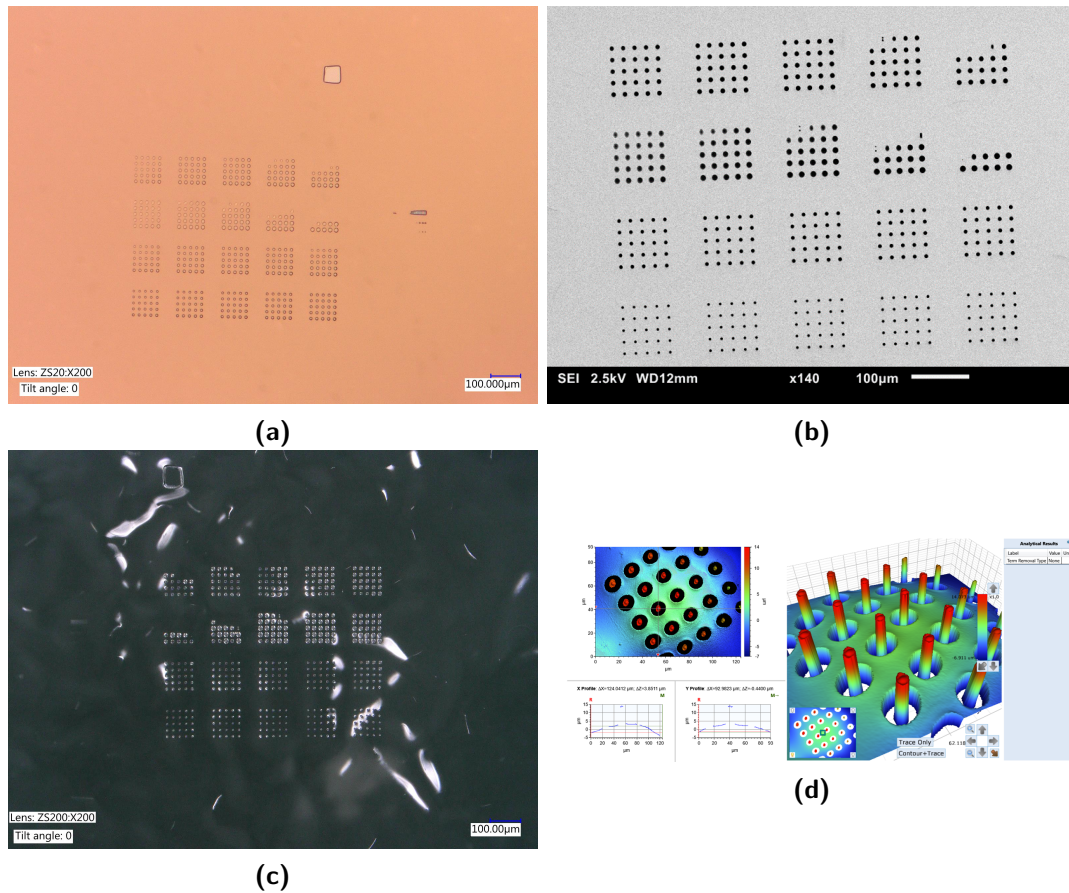


Figure D-10: (a) Optical image of the stamp. (b) SEM micrograph of the stamp. (c) PDMS pillars. (d) White light interferometer image from the pillars.

D-5 Channel and chip manufacturing

For the manufacturing of the channels, the machine parameters determined for Galvo Scan mode were used. The pores were written with Piezo Scan mode.

Designs

The design of the channels and the chips consists of multiple features. The design for the in- and outlet hole is shown in Figure D-11a. The channels were made out of blocks, limited by the maximum writing area of the Photonic Professional GT. The channel block is shown in Figure D-11b. The pores were written in Piezo Scan mode and the design is shown in Figure D-11c. Finally the features are combined a full chip design shown in Figure D-11d.

Development tactics

As explained in Methods and materials 3, the resist will only be removed when the exposed material can be dissolved in the developer solution. However, when creating channels under

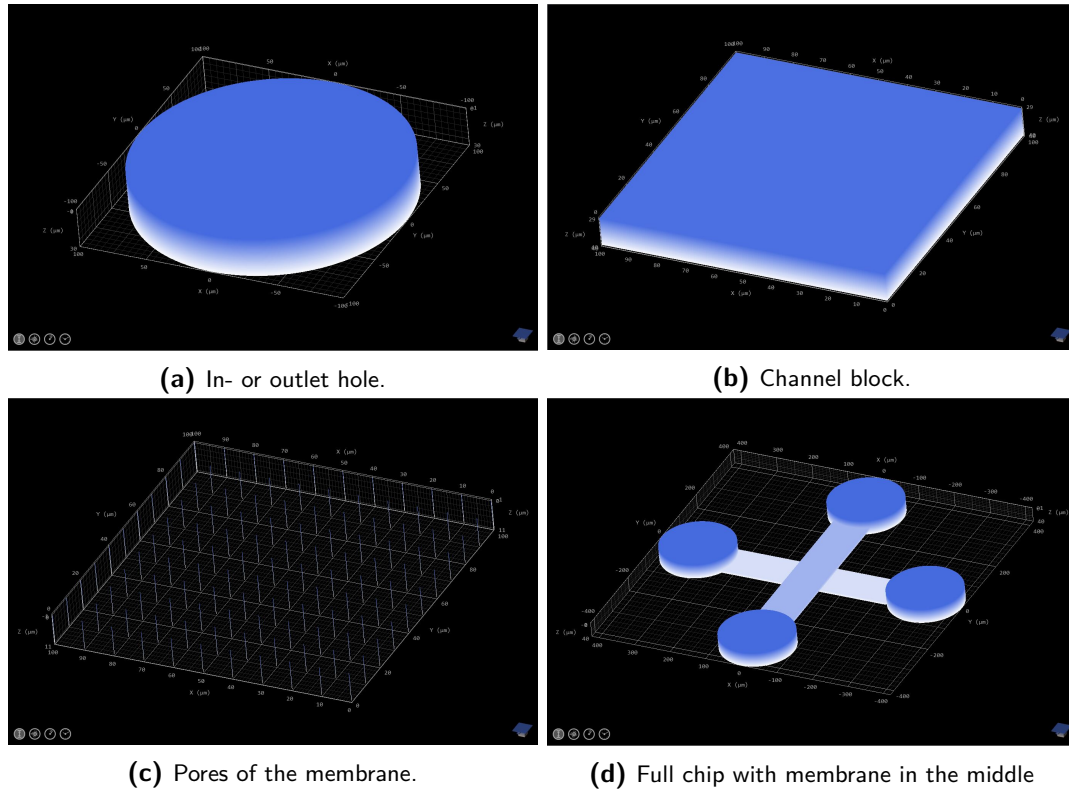


Figure D-11: The three features that make the chip and the full chip design.

the surface, it can take a long time for the developer to get through the entire channel. In this phase of the research different steps were taken to create a fully developed sub-surface channel.

- **No additional measures:**

When the sample was left in the developer without additional measures, the AZ 400K and the water started to separate. This resulted in a larger concentration of AZ 400K at the bottom of the beaker and a lower concentration at the top. The higher concentration dissolved unexposed material, whereas the lower concentration did not dissolve any resist. Figure D-13a shows how the unexposed resist was dissolved due to the higher concentration of AZ 400K.

- **Under different angles:**

To try to speed up the development process, the option of developing under different angles was explored. A difference in density between the dissolved resist and the developer solution could cause the access of the developer to be blocked. In Figure D-13b one of the experiments is shown. The vertical channels seem to have more dissolved resist, but the upper channel shows the least development. Therefore the decision was made to look for a different way of developing.

- **With higher temperature developer:**

The third attempt to speed up the development process was done with a developer

solution at a higher temperature. The heating did speed up the development, but the unexposed resist was affected. This is shown in Figure D-13c. Therefore the decision was made to keep the development temperature between 18 and 22 °C

- **With ultrasonic shaker:**

The next attempt was the use of an ultrasonic shaker during the development. The sample shown in Figure D-13d was developed for 10 min without the ultrasonic bath and 10 min with the ultrasonic bath. The result is holes that grew out of proportion due to the vibrations. Development strategies that used the ultrasonic shaker between 2 - 30 minutes all resulted in broken holes. Besides the broken holes, the channels did not develop faster.

- **While stirring with magnetic stirrer:**

Finally a magnetic stirrer was used to continuously mix the developer solution during the development. This gave the desired results that are shown in the main matter of this thesis. A magnetic stirrer works by using a stir bar or flea that is rotated due to a magnetic field. Initially this flea could not rotate due to the sample holder. Therefore a design for a small stage was made. The design is shown in Figure D-12a. The stage was 3D printed, shown in Figure D-12b and fitted into the beaker perfectly, making the magnetic stirrer a standard option for developing in future projects.



(a) The design for the stage.

(b) The 3D printed stage.

Figure D-12: The stage that was designed to enable the use of the magnetic stirrer.

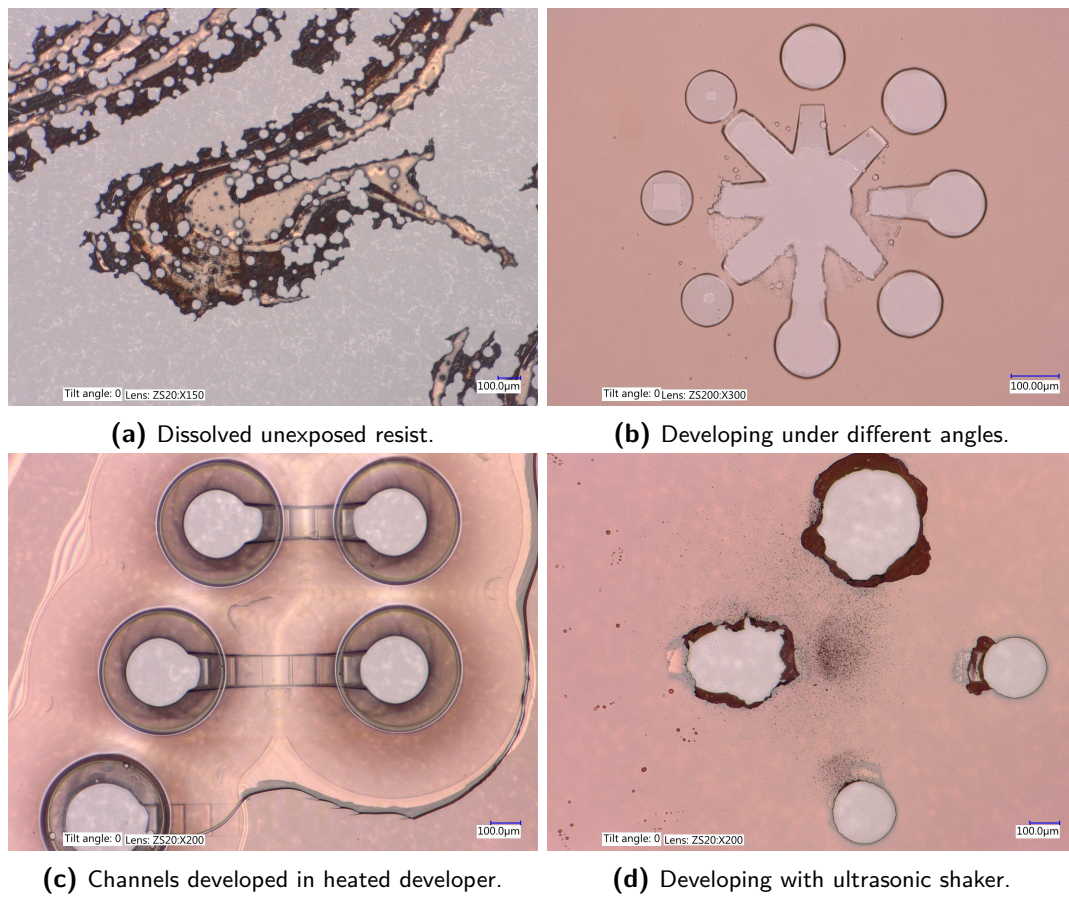


Figure D-13: Four failed development methods.

Appendix E

Extra work

Next to the work shown in this thesis, extra work was done. In this appendix this work is explained. A script for automatic pore measurement and a GUI for fitting the mode were written. Preparations for electrochemical deposition were made. The smallest blunt needle was prepared for experiments and finally an image of this project made it to the PME calendar.

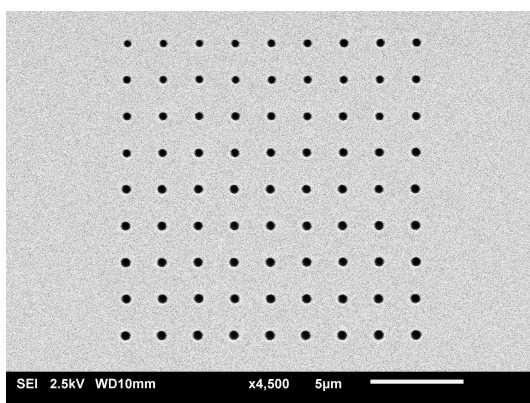
E-1 Automatic pore diameter measurement

In the iteration steps shown in Appendix A, one of the main time consuming parts is the measurement of the diameter of the pores. These measurements are usually done by human hands using the software installed with the Scanning Electron Microscope (SEM). The accuracy and precision of the measurements therefore depends on human factors. This, and the fact that is time consuming, was the reason that a software tool was developed for pore diameter measurement. The measurement was done in the following steps:

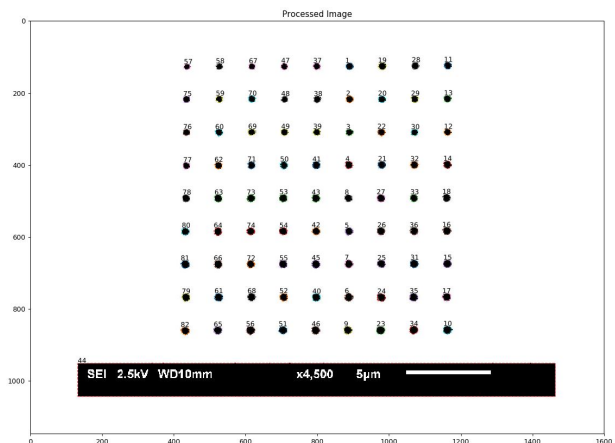
- **Imaging:** The imaging was done with an SEM. For the tool to be able to work, the micrograph had to be made with high contrast. In Fig. E-1c an example is given of a picture with too low contrast. In Fig. E-1a an image with high enough contrast for the tool is shown.
- **Enlarging contrast:** The image is loaded into a MatLab file where the first processing step is done. The image is read in pixels, giving each pixel a value. Black pixels will get a value of 0 and white pixels will get a value of 255. In this processing step, each pixel will get a new value that is the average of that pixel and the surrounding 8 pixels. If this average value gets below a certain number, it is now defined as a black pixel. If the value is above this number, the pixel is now defined as white. By trial and error a value of 100 is finally chosen.
- **Finding clusters:** This part of the tool is programmed in Python, because of the availability of strong image processing toolboxes. The program will search for a black

pixel, when this is found, the surrounding pixels are checked. If they are also black, they will be part of the cluster. After clustering the edges of the clusters are defined and the maximum distance between 2 pixels in the border will be defined as the pore diameter.

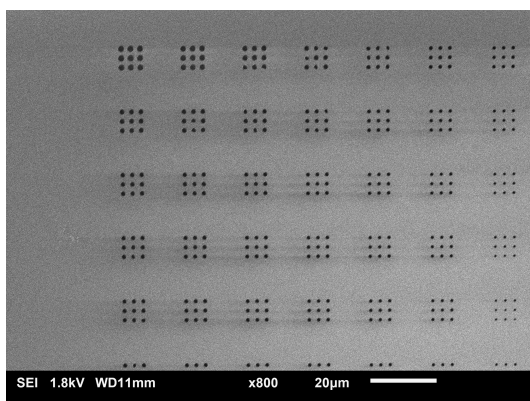
- **Reading data and comparing with human measurement:** Finally the result of the tool was compared to number of random human measurements. The result is shown in Fig. E-2a . The measurements do not correspond fully. This is due to the inaccuracy of the human measurements.



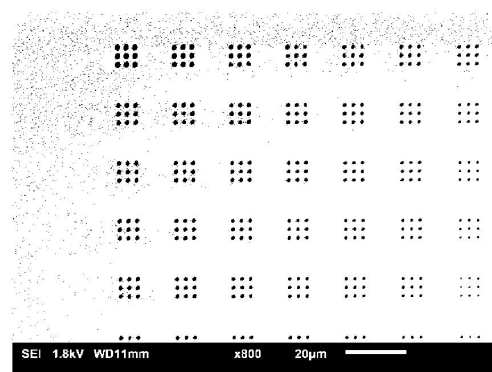
(a) High contrast micrograph



(b) Processed image.



(c) Low contrast micrograph



(d) The image can not be processed.

Figure E-1: High and low contrast images before and after processing.

A				
Nr.	SEM	Calculated	Difference	Percentage
14	0.444	0.445	-0.001	-0.2252
16	0.449	0.445	0.004	0.8909
21	0.444	0.424	0.02	4.5045
B				
Nr.	SEM	Calculated	Difference	Percentage
18	0.6	0.62	-0.02	-3.3333
28	0.634	0.621	0.013	2.0505
27	0.65	0.637	0.013	2.0000
83	0.65	0.637	0.013	2.0000
94	0.6	0.652	-0.052	-8.6667
98	0.667	0.637	0.03	4.4978
107	0.617	0.605	0.012	1.9449
109	0.617	0.637	-0.02	-3.2415
119	0.634	0.636	-0.002	-0.3155
C				
Nr.	SEM	Calculated	Difference	Percentage
1	287.408	285.075	2.333	0.8117
2	13.704	13.345	0.359	2.6197
D				
Nr.	SEM	Calculated	Difference	Percentage
41	0.633	0.646	-0.013	-2.0537
44	0.667	0.646	0.021	3.1484
13	0.633	0.63	0.003	0.4739
43	0.6	0.63	-0.03	-5.0000
2	0.633	0.645	-0.012	-1.8957
73	0.669	0.662	0.007	1.0463
55	0.635	0.646	-0.011	-1.7323

(a)

Legend
Difference is 2% or less
Human measurement very inaccurate
Difference is more than 2%

(b)

Figure E-2: The automatic pore measurement is all within 5% of human measurement, except for the situation where the human measurement was very inaccurate.

E-2 GUI for model fitting

Different GUIs were made during the project. The first one was made to show the mathematical influence of the unknown parameters in the main equation. When the decision was made to continue with two unknown variables, a new GUI was made to do a single least-squares error fit on the diameter measurements. Finally the last GUI was made to perform a combined least-squares error fit for the voxel height and diameter. This GUI is shown in Figure E-3.

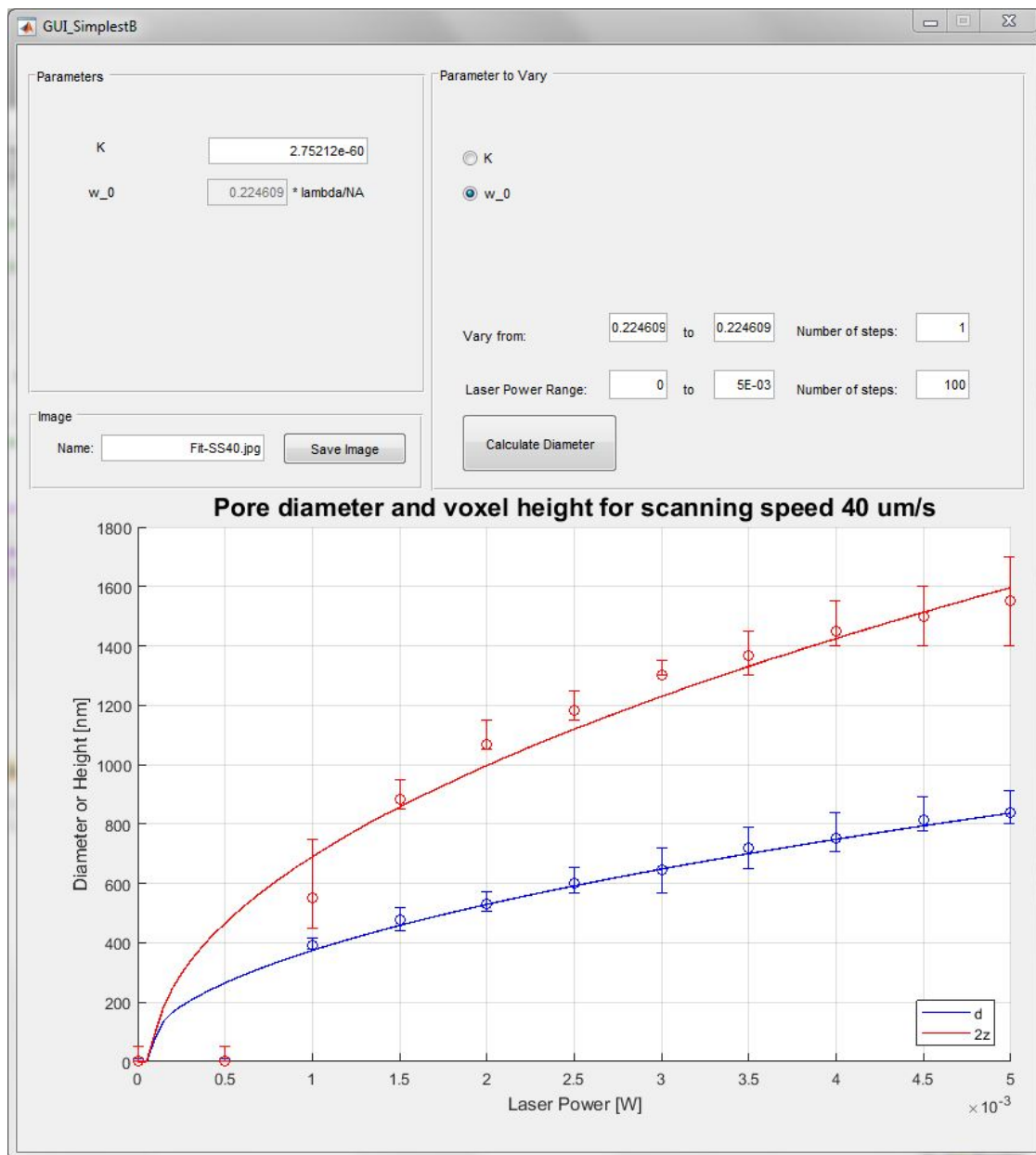


Figure E-3: GUI made for combined least-squares error fit.

E-3 Preparing for electrochemical deposition

To produce complex 3D structures from metals, electrochemical deposition can be used [76]. The surface of the substrate has to be conductive for this process to be possible. Substrates with a conductive layer were too thick to use in conventional writing configuration, shown in Figure E-4a. Therefore the possibilities of using a spincoated polymer layer in DiLL mode were explored. In Figure E-4b the immersion oil is placed between the resist and the objective. This made the substrate dirty and was not suitable to create structures. In Figure E-4c air is used as immersion medium. This setup worked, but much higher laser power needed to be used.

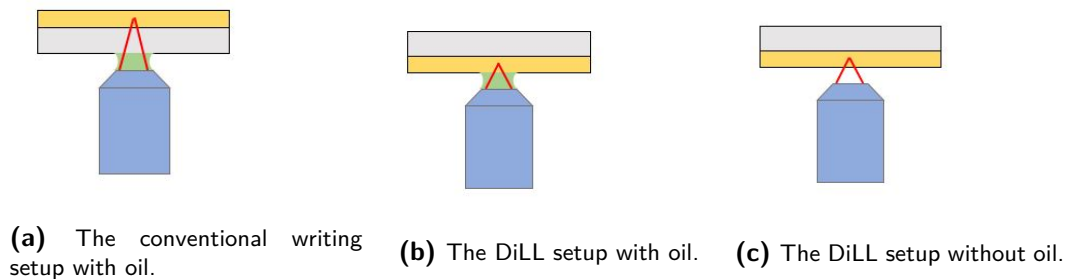


Figure E-4: Three writing configurations.

E-4 Needle preparation

The design was made for the smallest blunt needle available, which has a diameter of $210\ \mu\text{m}$. However, a blunt needle could be blocked when used for this experiment. Therefore an incision in the needle was made with the laser cutter. The incision is $10\ \mu\text{m}$ high and $50\ \mu\text{m}$ wide. The result is shown in Figures E-5a and E-5b.

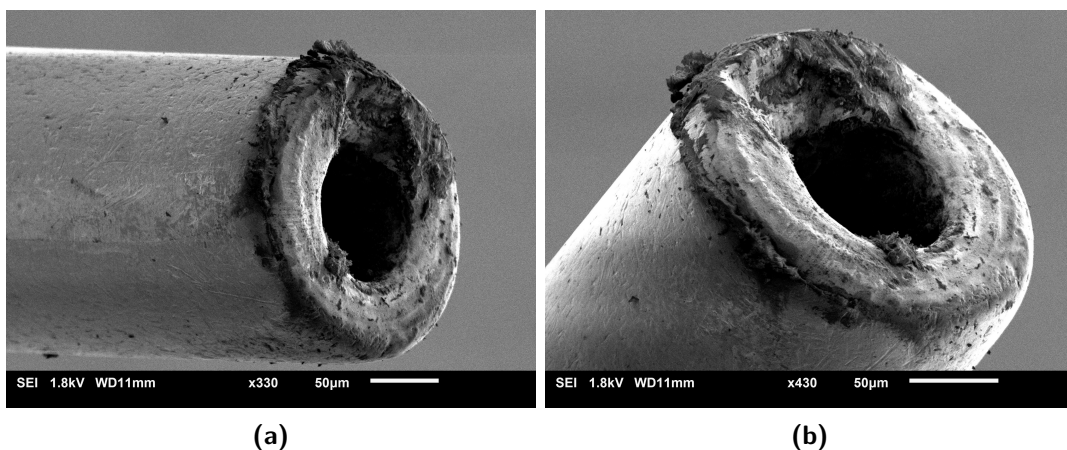


Figure E-5: SEM micrographs of needle with laser cut layer.



Figure E-6: Picture on the calendar of the PME department.

Bibliography

- [1] I. Torjesen, “Drug development: the journey of a medicine from lab to shelf,” 2015.
- [2] J. Endres, “The drug development process: From the lab to your medicine cabinet.,” 2017.
- [3] G. Hamilton, “Body parts on a chip,” 2013.
- [4] K. Groff, E. Bachli, M. Lansdowne, and T. Capaldo, “Review of Evidence of Environmental Impacts of Animal Research and Testing,” *Environments*, vol. 1, pp. 14–30, jun 2014.
- [5] University of Adelaide, “Laboratory Animal Services,” 2018.
- [6] Theodora Capaldo, “Animal Data Is Not Reliable for Human Health Research,” 2014.
- [7] B. Zhang and M. Radisic, “Organ-on-a-chip devices advance to market,” *Lab on a Chip*, vol. 17, pp. 2395–2420, jul 2017.
- [8] T. Pasman, D. Grijpma, D. Stamatialis, and A. Poot, “Flat and microstructured polymeric membranes in organs-on-chips,” *Journal of the Royal Society Interface*, vol. 15, p. 20180351, jul 2018.
- [9] S. N. Bhatia and D. E. Ingber, “Microfluidic organs-on-chips.,” *Nature biotechnology*, vol. 32, no. 8, pp. 760–72, 2014.
- [10] R. Masereeuw, J. Vriend, and M. J. Wilmer, “Kidney-on-a-Chip: Technologies for Studying Pharmacological and Therapeutic Approaches to Kidney Repair,” *Kidney Transplantation, Bioengineering and Regeneration*, pp. 1119–1133, jan 2017.
- [11] M. Zhang, C. Xu, L. Jiang, and J. Qin, “A 3D human lung-on-a-chip model for nanotoxicity testing,” *Toxicology Research*, 2018.

- [12] D. Sticker, M. Rothbauer, S. Lechner, M. T. Hehenberger, and P. Ertl, “Multi-layered, membrane-integrated microfluidics based on replica molding of a thiol-ene epoxy thermoset for organ-on-a-chip applications,” *Lab on a Chip*, vol. 15, pp. 4542–4554, nov 2015.
- [13] Corning Incorporated, “Guidelines for Use: Transwell® Permeable Supports | Life Sciences | Corning,” 2018.
- [14] D. Huh, B. D. Matthews, A. Mammoto, M. Montoya-Zavala, H. Yuan Hsin, and D. E. Ingber, “Reconstituting organ-level lung functions on a chip,” *Science*, vol. 328, pp. 1662–1668, jun 2010.
- [15] B. A. Hassell, G. Goyal, E. Lee, A. Sontheimer-Phelps, O. Levy, C. S. Chen, and D. E. Ingber, “Erratum: Human Organ Chip Models Recapitulate Orthotopic Lung Cancer Growth, Therapeutic Responses, and Tumor Dormancy In Vitro,” *Cell Reports*, vol. 23, p. 3698, oct 2018.
- [16] K. H. Benam, R. Villenave, C. Lucchesi, A. Varone, C. Hubeau, H. H. Lee, S. E. Alves, M. Salmon, T. C. Ferrante, J. C. Weaver, A. Bahinski, G. A. Hamilton, and D. E. Ingber, “Small airway-on-a-chip enables analysis of human lung inflammation and drug responses in vitro,” *Nature Methods*, vol. 13, pp. 151–157, feb 2016.
- [17] A. Bein, W. Shin, S. Jalili-Firoozinezhad, M. H. Park, A. Sontheimer-Phelps, A. Tovaglieri, A. Chalkiadaki, H. J. Kim, and D. E. Ingber, “Microfluidic Organ-on-a-Chip Models of Human Intestine,” *Cmgh*, vol. 5, pp. 659–668, jan 2018.
- [18] Y. Du, N. Li, H. Yang, C. Luo, Y. Gong, C. Tong, Y. Gao, S. Lü, and M. Long, “Mimicking liver sinusoidal structures and functions using a 3D-configured microfluidic chip,” *Lab on a Chip*, vol. 17, no. 5, pp. 782–794, 2017.
- [19] H. E. Abaci, K. Gledhill, Z. Guo, A. M. Christiano, and M. L. Shuler, “Pumpless microfluidic platform for drug testing on human skin equivalents,” *Lab on a Chip*, vol. 15, no. 3, pp. 882–888, 2015.
- [20] M. Cecchini, F. Signori, P. Pingue, S. Bronco, F. Ciardelli, and F. Beltram, “High-resolution polyethylene terephthalate (PET) hot embossing at low temperature: Thermal, mechanical, and optical analysis of nanopatterned films,” *Langmuir*, vol. 24, no. 21, pp. 12581–12586, 2008.
- [21] T. W. Odom, J. C. Love, D. B. Wolfe, K. E. Paul, and G. M. Whitesides, “Improved pattern transfer in soft lithography using composite stamps,” *Langmuir*, vol. 18, no. 13, pp. 5314–5320, 2002.
- [22] H. Schiff, C. David, M. Gabriel, J. Gobrecht, L. J. Heyderman, W. Kaiser, S. Köppel, and L. Scandella, “Nanoreplication in polymers using hot embossing and injection molding,” *Microelectronic Engineering*, vol. 53, no. 1, pp. 171–174, 2000.
- [23] R. Ogawa, N. Kaji, S. Hashioka, A. , F. Yasuaki Tamura, M. Hikita, and Y. Shuto, “Injection Molding of Nanopillars for Perpendicular Patterned Magnetic Media with Metallic Nanostamp,” *Japanese Journal of Applied Physics*, vol. 47, 2008.

-
- [24] R. M. Allaf, "Melt-molding technologies for 3D scaffold engineering," *Functional 3D Tissue Engineering Scaffolds*, pp. 75–100, jan 2017.
- [25] S. Y. Chou, "Sub-10 nm imprint lithography and applications," *Journal of Vacuum Science & Technology B: Microelectronics and Nanometer Structures*, vol. 15, no. 6, p. 2897, 1997.
- [26] C. J. Ting, M. C. Huang, H. Y. Tsai, C. P. Chou, and C. C. Fu, "Low cost fabrication of the large-area anti-reflection films from polymer by nanoimprint/hot-embossing technology," *Nanotechnology*, vol. 19, p. 205301, may 2008.
- [27] L. J. Guo, "Nanoimprint lithography: Methods and material requirements," *Advanced Materials*, vol. 19, pp. 495–513, feb 2007.
- [28] X. Zhang, L. Cox, Z. Wen, W. Xi, Y. Ding, and C. N. Bowman, "Implementation of two distinct wavelengths to induce multistage polymerization in shape memory materials and nanoimprint lithography," *Polymer*, vol. 156, pp. 162–168, nov 2018.
- [29] A. A. Tseng, K. Chen, C. D. Chen, and K. J. Ma, "Electron beam lithography in nanoscale fabrication: Recent development," *IEEE Transactions on Electronics Packaging Manufacturing*, vol. 26, pp. 141–149, apr 2003.
- [30] V. R. Manfrinato, A. Stein, L. Zhang, C. Y. Nam, K. G. Yager, E. A. Stach, and C. T. Black, "Aberration-Corrected Electron Beam Lithography at the One Nanometer Length Scale," *Nano Letters*, vol. 17, no. 8, pp. 4562–4567, 2017.
- [31] Y. Chen, Z. Lu, X. Wang, Z. Cui, G. Pan, Y. Zhou, M. Muñoz, C. Hao, L. Yonghua, and N. Garcia, "Fabrication of ferromagnetic nanoconstrictions by electron beam lithography using LOR/PMMA bilayer technique," *Microelectronic Engineering*, vol. 84, pp. 1499–1502, may 2007.
- [32] A. N. Broers, A. C. Hoole Andrew, and J. M. Ryan, "Electron beam lithography - Resolution limits," *Microelectronic Engineering*, vol. 32, no. 1-4 SPEC. ISS., pp. 131–142, 1996.
- [33] H. W. Li, D. J. Kang, M. G. Blamire, and W. T. Huck, "Focused ion beam fabrication of silicon print masters," *Nanotechnology*, vol. 14, no. 2, pp. 220–223, 2003.
- [34] G. Y. Liu, S. Xu, and Y. Qian, "Nanofabrication of self-assembled monolayers using scanning probe lithography," *Accounts of Chemical Research*, vol. 33, no. 7, pp. 457–466, 2000.
- [35] R. V. Martínez, N. S. Losilla, J. Martínez, Y. Huttel, and R. Garcia, "Patterning polymeric structures with 2 nm resolution at 3 nm half pitch in ambient conditions," *Nano Letters*, vol. 7, no. 7, pp. 1846–1850, 2007.
- [36] Y. Liao, C. H. Loh, M. Tian, R. Wang, and A. G. Fane, "Progress in electrospun polymeric nanofibrous membranes for water treatment: Fabrication, modification and applications," *Progress in Polymer Science*, vol. 77, pp. 69–94, feb 2018.

- [37] S. Yan, X. Zhang, L. Zhang, H. Liu, X. Wang, and Q. Li, "Polymer scaffolds for vascular tissue engineering fabricated by combined electrospinning and hot embossing," *Biomedical Materials (Bristol)*, vol. 13, p. 015003, nov 2018.
- [38] S. Juodkazis, V. Mizeikis, K. K. Seet, M. Miwa, and H. Misawa, "Two-photon lithography of nanorods in SU-8 photoresist," *Nanotechnology*, vol. 16, no. 6, pp. 846–849, 2005.
- [39] R. P. Chaudhary, A. Jaiswal, G. Ummethala, S. R. Hawal, S. Saxena, and S. Shukla, "Sub-wavelength lithography of complex 2D and 3D nanostructures without two-photon dyes," *Additive Manufacturing*, vol. 16, pp. 30–34, aug 2017.
- [40] S. Ibrahim, D. A. Higgins, and L. T. Ito, "Direct-write multiphoton photolithography: A systematic study of the etching behaviors in various commercial polymers," *Langmuir*, vol. 23, no. 24, pp. 12406–12412, 2007.
- [41] H. Z. Cao, M. L. Zheng, X. Z. Dong, F. Jin, Z. S. Zhao, and X. M. Duan, "Two-photon nanolithography of positive photoresist thin film with ultrafast laser direct writing," *Applied Physics Letters*, vol. 102, p. 201108, may 2013.
- [42] G. Williams, M. Hunt, B. Boehm, A. May, M. Taverne, D. Ho, S. Giblin, D. Read, J. Rarity, R. Allenspach, and S. Ladak, "Two-photon lithography for 3D magnetic nanostructure fabrication," *Nano Research*, vol. 11, no. 2, pp. 845–854, 2018.
- [43] MicroChemicals, "Chapter 01 MicroChemicals ®-Fundamentals of Microstructuring WET-CHEMICAL ETCHING OF METALS Etching of Aluminium Properties and Application Areas of Aluminium," tech. rep.
- [44] M. Hudedmani, C. Jambotkar, and V. M. Soppimath, "No Title," *European Journal of Applied Engineering and Scientific Research*, vol. 5, no. 1, pp. 1–13, 2017.
- [45] ISO 20473, "Optics and photonics – Spectral bands," 2007.
- [46] I. Tiginyanu, V. Ursaki, and V. Popa, "Nanoimprint lithography (NIL) and related techniques for electronics applications," *Nanocoatings and Ultra-Thin Films: Technologies and Applications*, pp. 280–329, jan 2011.
- [47] MicroChem, "Positive vs. Negative Tone Photoresists."
- [48] F. Wang and X. Liu, "Nanomaterials," *Comprehensive Nanoscience and Technology*, 2011.
- [49] N. V. Tkachenko, "Appendix C. Two photon absorption Title," *Optical Spectroscopy: Methods and Instrumentations.*, p. 293, 2006.
- [50] P. Busch, "The Time-Energy Uncertainty Relation $\hat{H}\hat{E}$," tech. rep., 2007.
- [51] X. Zhou, Y. Hou, and J. Lin, "A review on the processing accuracy of two-photon polymerization," *AIP Advances*, vol. 5, p. 030701, mar 2015.
- [52] S. Maruo, O. Nakamura, and S. Kawata, "Three-dimensional microfabrication with two-photon-absorbed photopolymerization," *Optics Letters*, vol. 22, p. 132, jan 1997.

-
- [53] F. Kohler, “3D micro-printing by Direct Laser Writing General introduction and application examples 2017,,” 2017.
- [54] S. A. Campbell, *The science and engineering of microelectronic fabrication*, vol. 34. 2 ed., 2013.
- [55] MicroChemicals, “General Properties of AZ / TI Photoresists,” tech. rep., 2007.
- [56] J. Albers, “Intensity Dependence of Photochemical Reaction Rates for Photoresists,” *Journal of The Electrochemical Society*, vol. 127, p. 1400, jun 2006.
- [57] M. Göppert-Mayer, “Über Elementarakte mit zwei Quantensprüngen,” *Annalen der Physik*, vol. 401, pp. 273–294, jan 1931.
- [58] M. G. Mlynczak and D. J. Nesbitt, “The Einstein Coefficient for spontaneous emission of the O₂ state,” *Geophysical Research Letters*, vol. 22, pp. 1381–1384, jun 1995.
- [59] L. Li and J. T. Fourkas, “Multiphoton polymerization,” *Materials Today*, vol. 10, no. 6, pp. 30–37, 2007.
- [60] H.-B. Sun, M. Maeda, K. Takada, J. W. M. Chon, M. Gu, and S. Kawata, “Experimental investigation of single voxels for laser nanofabrication via two-photon photopolymerization,” *Applied Physics Letters*, vol. 83, no. 5, pp. 819–821, 2003.
- [61] C. N. LaFratta, J. T. Fourkas, T. Baldacchini, and R. A. Farrer, “Multiphoton fabrication,” *Angewandte Chemie - International Edition*, vol. 46, pp. 6238–6258, aug 2007.
- [62] W. Schottky, “Über spontane Stromschwankungen in verschiedenen Elektrizitätsleitern,” *Annalen der Physik*, vol. 362, no. 23, pp. 541–567, 1918.
- [63] R. Paschotta, “Noise in Laser Technology Part 1: Intensity and Phase Noise the Encyclopedia of Laser Physics and Technology,” Tech. Rep. 2, 2009.
- [64] Nanoscribe, “Photonic Professional GT Datasheet,” no. July, 2013.
- [65] S. Jeon, V. Malyarchuk, J. A. Rogers, and G. P. Wiederrecht, “Fabricating three-dimensional nanostructures using two photon lithography in a single exposure step,” *Optics Express*, vol. 14, p. 2300, mar 2006.
- [66] J. C. McDonald and G. M. Whitesides, “Poly(dimethylsiloxane) as a Material for Fabricating Microfluidic Devices,” 2002.
- [67] K. Ren, J. Zhou, and H. Wu, “Materials for Microfluidic Chip Fabrication,” *Accounts of Chemical Research*, vol. 46, pp. 2396–2406, nov 2013.
- [68] F. Li, P. Smejkal, N. P. Macdonald, R. M. Guijt, and M. C. Breadmore, “One-Step Fabrication of a Microfluidic Device with an Integrated Membrane and Embedded Reagents by Multimaterial 3D Printing,” *Analytical Chemistry*, vol. 89, no. 8, pp. 4701–4707, 2017.
- [69] M. J. Dalby, N. Gadegaard, R. Tare, A. Andar, M. O. Riehle, P. Herzyk, C. D. Wilkinson, and R. O. Oreffo, “The control of human mesenchymal cell differentiation using nanoscale symmetry and disorder,” *Nature Materials*, vol. 6, pp. 997–1003, dec 2007.

- [70] L. E. McNamara, R. J. McMurray, M. J. Biggs, F. Kantawong, R. O. Oreffo, and M. J. Dalby, "Nanotopographical control of stem cell differentiation," *Journal of Tissue Engineering*, vol. 1, no. 1, pp. 1–13, 2010.
- [71] M. K. Dawood, H. Zheng, T. H. Liew, K. C. Leong, Y. L. Foo, R. Rajagopalan, S. A. Khan, and W. K. Choi, "Mimicking both petal and lotus effects on a single silicon substrate by tuning the wettability of nanostructured surfaces," *Langmuir*, vol. 27, no. 7, pp. 4126–4133, 2011.
- [72] P. F. Shanley, M. D. Rosen, M. Brezis, P. Silva, F. H. Epstein, and S. Rosen, "Topography of focal proximal tubular necrosis after ischemia with reflow in the rat kidney," *Tech. Rep.* 3, 1985.
- [73] MicroChemicals, "Basic Chemistry of Developers," tech. rep.
- [74] J. Cheng, Y. Tao, Y. Zhang, Z.-Q. Cai, P. Pi, X. Wen, D. Zheng, Z. Yang, L. Lu, and Y. Tang, "Liquid Flow in Rectangular Microchannels with Gradient Wettability Inner Surface Driven by Capillary Force and Gravity," 2011.
- [75] S. Mozaffari, P. Tchoukov, A. Mozaffari, J. Atias, J. Czarnecki, and N. Nazemifard, "Capillary driven flow in nanochannels – Application to heavy oil rheology studies," *Colloids and Surfaces A: Physicochemical and Engineering Aspects*, vol. 513, pp. 178–187, 2017.
- [76] K. Hili, D. Fan, V. A. Guzenko, and Y. Ekinici, "Nickel electroplating for high-resolution nanostructures," *Microelectronic Engineering*, vol. 141, pp. 122–128, jun 2015.